UNIVERSITÁ DEGLI STUDI DI PADOVA

Dipartimento di Ingegneria dell'Informazione

Tesi di Laurea Magistrale

Experimentation of Entangled photon-pairs generation using an ultrafast source at gigahertz

Laureando: **Eduardo Bloise**

Relatore: Ch.mo Prof. **Paolo Villoresi**

Correlatore: Dott. **Giuseppe Vallone**

Corso di laurea in Ingegneria delle Telecomunicazioni

Padova, 8 Luglio 2013

Anno Accademico 2012-2013

a Mary

Contents

Abstract

In this dissertation we will present the experimental study of polarization entangled photon pairs generation, through *spontaneous parametric down conversion* (SPDC) using an ultrafast source at gigahertz.
The laser source that we used is a TACCOR 8, a femtosecond pulses source with a repetition rate of 1 GHz and an average power up to 1.4 W.
The optical process of *second harmonic generation* (SHG) at the wavelenght $\lambda = 405$ nm is generated by a periodically poled KTP (PPKTP) crystal. This is characterized by a high nonlinear second order coefficient that allow to generate a really efficient second harmonic through the quasi phase matching (QPM) technique. We mainly tested the second harmonic generation with PPKTP but we also tested it with BBO and BiBO crystals in order to obtain a comparison among SHG power, conversion efficiency,temporal and spectral width of second harmonic pulse. Finally, we measured the photon-pairs generation rate in the best case of conversion efficiency of SHG with PPKTP.

Sommario

In questo lavoro di tesi viene presentato uno studio sperimentale di generazione di coppie di fotoni Entangled con l'utilizzo di una sorgente laser ultraveloce al gigahertz. Il laser utilizzato é il TACCOR 8, una sorgente in grado di generare impulsi al femtosecondo con una frequenza di ripetizione di 1 GHz e una potenza media fino a 1.4 W. La generazione di seconda armonica (SHG) alla lunghezza d'onda di 405 nm é stata prodotta utilizzando un cristallo KTP periodicamente polarizzato (PPKTP), caratterizzato dall'avere un alto coefficiente non lineare del secondo ordine che produce una seconda armonica molto efficiente sfruttando il meccanismo del quasi-phase matching (QPM). Principalmente, é stato testato il funzionamento della generazione di seconda armonica col cristallo PPKTP, ma lo stesso esperimento é stato effettuato anche con i cristalli BBO e BiBO in modo da poter avere un confronto sulla potenza di seconda armonica generata, sull'efficienza di conversione e sulle caratteristiche temporali e spettrali degli impulsi prodotti. Infine, abbiamo effettuato l'esperimento di generazione di coppie di fotoni Entangled utilizzando la miglior seconda armonica prodotta col cristallo PPKTP, andando a misurare il rate di coincidenze.

Chapter 1

Introduction

1.1 Aim of the thesis

The pulsed laser source at gigahertz frequencies is a new attractive technology, that finds application in many fields. Recently, it has been studied the use of this source on metrology and spectroscopy, ultrafast time-domain spectroscopy, biomedical imaging and two photon microscopy [1].
In this thesis we want to study the possibility of using this new laser as a source for applications in *Quantum information* and *Quantum criptography*. Specifically, the aim of this dissertation is an experimental study on how the gigahertz laser can be used for the generation of polarization entangled photon pairs via SPDC. With this work we would like to improve the efficiency of generation of photon pairs per unit of power. In other words, we can see if it is possible enhance the probability of generation of a single entangled photon pair. The incident active pump pulses on SPDC crystal, comes from the process of second harmonic generation. Therefore, in order to obtain active pulses, the process of SHG should be efficient, so as to generate a second harmonic wave with the highest power per pulse.

1.2 Problem analysis and possible solution

Pulsed laser source with high repetition rate and average power of $\sim 1W$ have pulses with low energy. The TACCOR laser sources that we used in this work is produced by Laser Quantum GmbH. The first laser, the TACCOR 6 with average power of $800mW$ was used in the first experiment on SHG while the second laser, TACCOR 8 with average power of $1.4W$ was used in the other all experiments.
Consider the TACCOR 6 laser source with repetition rate of 1 GHz, average

power $P_m = 800 \ \ mW$ at 810 nm and pulse duration of 70 fs. In this case the generated pulses are characterized by the following features:

$$E_{pulse} = \frac{P_m}{repetition \ \ rate} = 0.8 \ \ nJ \tag{1.1}$$

$$P_{pulse} = \frac{P_m}{(repetition \ \ rate)(pulse \ \ duration)} \simeq 11 \ \ MW \tag{1.2}$$

With this value of power the process of SH generation is difficult because the power per pulse is very low. As a matter of fact, in the first experiment carried out in September 2012 we tested the SH generation using a 1 mm BBO crystal and we obtained an efficiency of SH equal to $\eta = 1.9$ %.
This result is similar to that of other several studies about generation of SH in the blue with BBO and BiBO crystals. For istance, in Figure 1, we report a result of one of these studies [2].

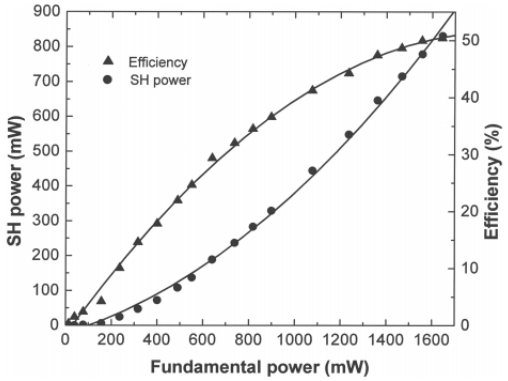

(a) SH avarage power and conversion efficiency as a function of input fundamental power at 406 nm

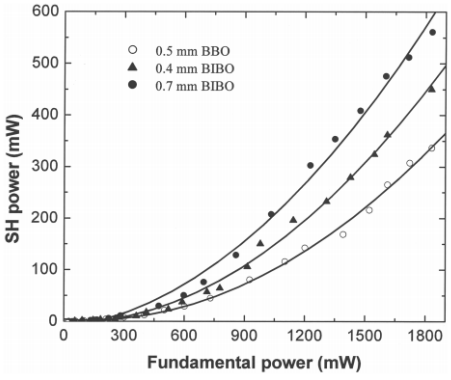

(b) Comparison of the generated SH power in BBO and BIBO as a function of input fundamental power at 406 nm

Figure 1.1

In the work [2] it was used a fundamental beam coming from a mode-locked Ti:sapphire laser (Coherent, Mira) at 76 MHz with an average power of up to 1.9 W over a tunable range $750 - 950$ nm and pulse duration of 130 fs. If we want to make a comparison between our experiment and the work in [2], we should compare the two lasers and calculate the average power of the MIRA laser corresponding to the same power per pulse generated by TACCOR 6 laser. Because the repetition rate of Mira is 13 times lower and the pulse duration is 3 times larger than TACCOR ones, the average power of Mira should be about $100 - 200$ mW. With this value of power we obtain an efficency of about 2 % as we can see from Figure 1.a, that is comparable

with our result. This low value of efficiency determines a low conversion efficiency in photon-pairs generation by SPDC process. For this reason we should find possible solutions to improve the efficiency of the SHG optical process.
Consider the following expression of SH efficiency:

$$\eta_{SH} = C^2 \frac{L^2}{\mathbf{A}} \mathbf{P} \tag{1.3}$$

where C^2 is a constant (W^{-1}) proportional to the square of both d-coefficient and frequency ω of fundamental wave, L is the lenght of the crystal and $\mathbf{P}/\mathbf{A}$ is the intensity of fundamental wave.
To maximize the SHG efficiency it is necessary that the incident wave has the largest possible power and ratio L^2/A. If the fundamental power is fixed, to maximize the efficiency we have to focus the fundamental wave to the smallest possible area and provide the longest possible crystal interaction length L, even if the maximum value of L is limited by the depth of focus of the incident beam. For instance, a Gaussian beam focused on a beam width W_0 maintains a beam cross-section area $\mathbf{A}$ over a depth of focus and if the beam is focused to the small spot size the depth of focus is short. Otherwise, if the beam is focused in a large spot size the depth of focus is long.
In our case the power of input wave is fixed and in a BBO experiment we used the best focusing condition with focal length $f = 40 \ \ mm$. Then, if we want to improve the SH efficiency using BBO or BiBO crystal we have to increase the length L of the crystal. However, crystals like BBO and BiBO with long interaction lenght are affected by the phenomena of *spatial walk-off* and *temporal walk-off* [3] . The spatial walk-off, that can occur in anisotropic crystals, depends on the intensity distribution drift from the direction defined by the wave vector. This is due to the fact that the waves interacting within of the crystal lose their spatial overlap during the propagation and the conversion efficiency can be limited, as well as the spatial profile of producted beams may be broadened and the beam quality reduced. The temporal walk-off occurs when the pulses with different frequencies propagate with different group-velocities and the interacting waves lose their temporal overlap after some propagation distance. These effects can limit the conversion efficiency and can stretch the product pulse in time.
In the case with spatial and temporal walk-off, if we want to obtain high efficiency we have to compensate these effects. Several studies like [4] can minimize lateral walk-off by stacking multiple crystals with alternating walk-off directions and similarly it is possible to minimize temporal walk-off in multiple crystals with alternating signs of group velocity. Other studies propose a technique using configurations with a pair of prisms to compensate the spa-

tial and temporal dispersion [5] or input lens which focuses the fundamental beam into the crystal in an elliptical way. On the one hand these techniques provide good efficiency of second harmonic generation, on the other hand the experimental setup in some cases is complicated to built.
To improve the SH efficiency another parameter to be considered is **C** that depends on the nonlinear coefficient of the medium. Then it is possible to find other different crystals besides BBO or BiBO with high second order nonlinear coefficients. One of the most efficient ways to achieve high conversion efficiency in the blue spectral region is using crystals that implement quasi phase matching (QPM) technique. These nonlinear crystals are now recognized as versatile and highly attractive materials candidated for wide range of frequency conversion applications. The flexibility offered by quasi-phase matching allows access to increased nonlinear optical coefficients, permits wavelength generation within the entire trasparency window of the material and facilitates noncritical phase matching over arbitrary long interaction lengths without the effects of beam walkoff and focusing [6]. Of a number of QPM materials, periodically poled L_iNbO_3 has been firmly established as the most prominent crystal for frequency conversion applications in the infrared. However, its use for wavelength generation in the visible and mainly in ultraviolet is hampered by photorefractive damage.
In the SPDC process it is also important that the incident pulses are chacacterized by narrow-bandwidth and consequently long coherence time. In order to obtain these properties it is possible to realize a "spectral compressor", a device that can convert with high efficiency a broadband pulse into a narrowband one. An interesting study in literature [7] has created a second harmonic generation in the presence of a large group velocity mismatch (GVM) between the fundamental and SH wave. The interacting pulses transfer a large fraction of the energy from a broadband fundamental femtosecond pulse into a narrowband picosecond second harmonic one. To create this it was used a long periodically poled stoichiometric lithium tantalate crystal (PPSLT) in presence of large GVM. However, in a crystal with these characteristics the phase-matching bandwidth for the SHG is very narrow and we would expect that only a small fraction of the fundamental spectrum is converted to the SH, leading to poor conversion efficiency. However, with a broadband fundamental pulse, the output wave is generated by a classical second harmonic process ($\omega_{SH} = \omega_F + \omega_F$) and also by sum frequency generation (SFG) between the spectral component of the fundamental pulse that are symmetric with respect to the phase matching frequency. In particolar, $\omega_{SH} = \omega_1 + \omega_2$ where $\omega_1 = \omega_F + \Delta\omega$ and $\omega_2 = \omega_F - \Delta\omega$.
In this thesis we have tested a SHG with periodically poled KTP that represents an attractive material candidate for our spectral range due to increased

resistance to photorefractive damage, high effective nonlinearity coefficient d_{eff} and wide trasparency up to 4000 nm. At the same time, the development of QPM materials for visible and ultraviolet frequency conversion places stringent tolerance demands on the fabrication of shorter grating periods. However, ongoing advances in poling technology continue to yield shorter grating periods of improved quality and uniformity over increased interaction lengths for first-order quasi-phase matching at lower wavelengths.

Chapter 2

Elements of quantum communications

The new physical theory called *quantum theory* was born when Max Plank explained his idea about the black body radiation. From this time on, the way of treating the microscopic world changed forever. Moreover, the classical theory of physics became inadequate to explain the microscopic physical phenomena. For instance phenomena like wave-particle duality or the principle of superposition could not be described in classical physics.
Quantum mechanics has its principal applications in the field of physics but, since about thirty years, it has developed in the field of telecommunication engineering. *Quantum information* is one of the most promising applications of quantum mechanics in the field of telecommunication. Its main applycations are *quantum cryptography* [8] and in particular *quantum key distribution*; *quantum dense coding* that exploits the phenomenon according to which sending a single bit of quantum information (qubit), two bits of classical information can be trasmitted [9]. Finally, *quantum teleportation*, the phenomenon that allows the transfer of an unknown quantum state from a sender to a receiver [10].
In the first part of this chapter we present the basis of quantum mechanics and in the second part we explain the quantum phenomenon called *entanglement*, which plays the main role in the application of quantum information.

2.1 Basis of quantum mechanics

2.1.1 The mathematical model of quantum mechanics

The quantum mechanics is based on the mathematical theory of Hilbert spaces over complex numbers. Now we remember the principal definition and notation that we will use to understand the following concepts about quantum information.

Def. 1 (**Hilber space of finite dimension**)**.** The Hilbert spase $\mathcal{H}$ is a vector space endowed with a complete inner product.

For quantum communication we consider a finite dimension Hilbert space and in this case every Cauchy sequence in $\mathcal{H}$ has a limit in $\mathcal{H}$. A finite dimension Hilbert space is always complete.
Consider $\mathcal{H}$ be a vector space of dimension N over complex number. We denote the elements vector of $\mathcal{H}$ as $|\varphi\rangle, |\chi\rangle, ...$ and with λ, μ the complex numbers.
The scalar product of two vectors will be donoted as $\langle\chi|\varphi\rangle$ and it has the following properties:

- *Linearity:* $\langle\chi|(\lambda|\varphi_1 + \mu|\varphi_2)\rangle = \lambda\langle\chi|\varphi_1\rangle + \mu\langle\chi|\varphi_2\rangle$
- *Complex conjugation:* $\langle\chi|\varphi\rangle = \langle\varphi|\chi\rangle^*$
- *Positive-definite:* $\langle\chi|\chi\rangle = 0 \iff |\chi\rangle = 0$

Def. 2 (**Orthonormal basis**)**.** It is defined an orthonormal basis in $\mathcal{H}$, composed of N vectors, as $\{|n\rangle\} \equiv \{|1\rangle, |2\rangle, ..., |n\rangle, ..., |N\rangle\}$ where $\forall|n\rangle, |m\rangle \in \{|n\rangle\}$ is valid:

$$\langle n|m\rangle = \delta_{nm} = \begin{cases} 1 & if \quad n = m \\ 0 & if \quad n \neq m \end{cases} \tag{2.1}$$

Any vector $|\chi\rangle$ can be decomposed on this basis with coefficients c_n which are the component of $|\chi\rangle$ in this basis:

$$|\chi\rangle = \sum_{n=1}^{N} c_n|n\rangle \tag{2.2}$$

In quantum mechanics the concept of superposition is fundamental and a physic state which could assume two quantum states $\chi_1\rangle$ and $|\chi_2\rangle$ can be found in a superposition of these quantum states:

$$|\chi\rangle = \lambda_1|\chi_1\rangle + \lambda_2|\chi_2\rangle \tag{2.3}$$

where $\chi_1\rangle, |\chi_2\rangle$ are orthonormal.
If the state $|\chi\rangle$ is normalized, the complex coefficients follow the equality: $|\lambda_1|^2 + |\lambda_2|^2 = 1$ and the terms $|\lambda_1|^2$ and $|\lambda_2|^2$ represent the probability that the system is found in state $\chi_1\rangle$ or $|\chi_2\rangle$ respectively.

Def. 3 (**Linear operator**)**.** A linear operator $\mathbf{A}$ is a function between two Hilbert spaces $\mathcal{H}$; it respects the linear property.

$$\mathbf{A} : \mathcal{H} \to \mathcal{H} \tag{2.4}$$

$$|\mathbf{A}(\varphi + \lambda\chi)\rangle = |\mathbf{A}\varphi\rangle + \lambda|\mathbf{A}\chi\rangle \tag{2.5}$$

When an operator $\mathbf{A}$ is applied on a quantum state, the physical system evolves in a new quantum state.

$$|\chi_2\rangle = \mathbf{A}|\chi_1\rangle \quad with \quad |\chi_2\rangle \in \mathcal{H} \tag{2.6}$$

An operator can be represented by a matrix. If we want to represent an operator with a matrix we should define an orthonormal basis $\{|n\rangle\}$ in which an element of the matrix is equal to:

$$a_{ij} = \langle n_i|\mathbf{A}|n_j\rangle, \quad with \quad |a_i\rangle, |a_j\rangle \in \{|n\rangle\} \tag{2.7}$$

Basing on the operator matrix, we can obtain the original operator as follows:

$$\mathbf{A} = \sum_i \sum_j a_{ij}|n_i\rangle\langle n_j| \tag{2.8}$$

An important property of an operator's matrix is that it varies depending on the base. If we choose two different basis $\{|n\rangle\}$,$\{|m\rangle\}$ they generate two different matrices of the same operator.

Def. 4 (**Trace of an operator**)**.** The trace of an operator is the sum of its diagonal elements:

$$Tr(\mathbf{A}) = \sum_{\mathbf{i}} \langle \mathbf{n_i}|\mathbf{A}|\mathbf{n_j}\rangle \tag{2.9}$$

The trace of an operator is invariant under a change of basis.

In quantum mechanics *Hermitian* and *Unitary* operators are used almost entirely.

Def. 5 (**Hermitian operator**)**.** An operator $\mathbf{A}$ is hermitian if the operator is equal to its hermitian conjugate.

$$\mathbf{A}^* = \mathbf{A} \tag{2.10}$$

where the hermitian conjugate $\mathbf{A}$ is defined as: $\langle\chi|\mathbf{A}^*\varphi\rangle = \langle\mathbf{A}\chi|\varphi\rangle = \langle\varphi|\mathbf{A}\rangle^*$.
Consequently, every matrix that represents $\mathbf{A}$ is a hermitian matrix.

Def. 6 (Unitary operator). An operator $\mathbf{U}$ is unitary if the following equality is true:

$$\mathbf{U}\mathbf{U}^* = \mathbf{I}_{\mathcal{H}} \tag{2.11}$$

where $\mathbf{I}_{\mathcal{H}}$ is identity operator.

Def. 7 (The Observables). In physics an observable is any physical quantity that can be measured by a sequence of physical operations. In quantum mechanics an observable is an hermitian operator connected to a misurable physical quantity as a quantum state.

In quantum mechanics, measurement of observables exhibits some seemingly unintuitive properties. Specifically, if a system is in a state described by a vector in a Hilbert space, the measurement process affects the state in a non-deterministic, but statistically predictable way. In particular, after a measurement is applied, the state description by a single vector may be destroyed, being replaced by a statistical ensemble.
In quantum system each quantum state is associated with a Hermitian operator that acts on the state of the quantum system and whose eigenvalues correspond to the possible values of the dynamical variable. For example, suppose $|\varphi_i\rangle$ is an eigenket (eigenvector) of the observable, with eigenvalue λ_i where:

$$\mathbf{A}|\varphi_i\rangle = \lambda_i|\varphi_i\rangle \tag{2.12}$$

This eigenstate equation says that if a measurement of the observable $\mathbf{A}$ is made while the system of interest is in the state $|\varphi_i\rangle$, then the observed value of that particular measurement must return the eigenvalue λ_i. In general the quantum state is a superposition of states and we can write:

$$|\varphi\rangle = \sum_i c_i|\varphi_i\rangle \tag{2.13}$$

where $c_i = \langle\varphi_i|\varphi\rangle$.
In this case the eigenvalue λ_i has only a probability to be found, but not a certainty.

$$P_i = |\langle\varphi_i|\varphi\rangle|^2 \tag{2.14}$$

Moreover, in quantun mechanics we can discriminate two types of states: the *pure state* described by a single state vector and the *mixed states* that are a statistical ensamble of several quantum states. Another method to decribe the statistical property of a quantum state is through a density matrix.

Def. 8 (Density matrix). The density matrix ρ is an operator on the Hilbert space $\mathcal{H}$ that is defined as:

- if $|\varphi$ is a pure state:
$$\rho = |\varphi\rangle\langle\varphi| \tag{2.15}$$
- if $|\varphi$ is a mixed state where the system has a probability q_i to be in the state $|\varphi_i$:
$$\rho = \sum_{\mathbf{i}} \mathbf{q_i}|\varphi_\mathbf{i}\rangle\langle\varphi_\mathbf{i}| \tag{2.16}$$

2.1.2 Postulate of quantum mechanics

Now we present the basic postulates of quantum mechanics in the general conceptual framework.

Postulate 1 (*the space of states*). *The property of quantum system is completely defined by specification of its state vector $|\varphi\rangle$, which fixes the mathematical representation of the system's physical state. The state vector is an element of a complex Hilbert space $\mathcal{H}$ called space of states. [11]*

It is important to define the specific nature of the state vector $|\varphi\rangle$ which should be unitary and have a unit norm:

$$||\varphi||^2 = \langle\varphi|\varphi\rangle = 1 \tag{2.17}$$

An important consequence of the vector representation of a quantum state that derives from linearity of the Hilbert space is the superposition of the states. If $|\varphi\rangle$ and $|\chi\rangle$ are vectors of $\mathcal{H}$ rappresenting quantum state, the normalized vector is:

$$|\psi\rangle = \frac{\lambda|\varphi\rangle + \mu|\chi\rangle}{||\lambda|\varphi\rangle + \mu|\chi\rangle||} \tag{2.18}$$

with λ and μ are complex numbers, $|\psi\rangle$ is a vector of $\mathcal{H}$ and also rappresents a physical state.

Postulate 2 (*Heisenberg*). *The time evolution of a closed quantum system is described by an unitary operator $\mathbf{U}$. If $|\psi(t_0)\rangle$ is the state of the system at the time t_0, the state of the system at the time t is:*

$$|\psi(t)\rangle = \mathbf{u}|\psi(t_0)\rangle \quad t > t_0 \tag{2.19}$$

In other words, the time evolution of a closed quantum system with state $|\phi(t)\rangle$ is governed by Shrödinger equation.

$$i\hbar\frac{\partial}{\partial t}|\psi(t)\rangle = \mathbf{H}(t)|\phi(t)\rangle \tag{2.20}$$

Postulate 3 (***Measure on quantum states***). *A measurement on a quantum system that is described by an Hilbert space $\mathcal{H}$ can be obtained through a system of complete orthogonal projection operators $\{\mathbf{\Pi_i}, \mathbf{i} \in (\mathbf{M})\}$ where $\mathcal{M}$ is a set of possible measurements' results.*
If the system before the measurements is in a quantum state $|\phi\rangle$, the probability that the result of the measumentent is $m = i$ is equal to:

$$P[m = i|\phi] = \langle\psi|\mathbf{\Pi}_i|\psi\rangle \tag{2.21}$$

Def. 9 (**orthogonal projection operators**). The orthonormal projection operators $\{\mathbf{\Pi_i}, \mathbf{i} \in (\mathbf{M})$ defined on the Hilbert space $\mathcal{H}$ are a set of quantum operators that satisfy the following properties:

$$\mathbf{\Pi}_i^2 = \mathbf{\Pi}_i, \quad \mathbf{\Pi}_i\mathbf{\Pi}_j = \mathbf{0}_\mathcal{H} \text{ with } i \neq j, \quad \sum_{i\in\mathcal{M}} \mathbf{\Pi}_i = \mathbf{I}_\mathcal{H} \tag{2.22}$$

where $\mathbf{0}_\mathcal{H}$ is the zero operator and $\mathbf{I}_\mathcal{H}$ is the identity operator.

We can also describe the Postulate 3 of quantum mechanics through the density matrix of a quantum state. If $|\phi\rangle$ is a quantum state before the measurement and we know the statistical description of the state, the probability that the result of the measurement is $m = i$ is:

$$P[m = i|\psi] = Tr(\rho\mathbf{\Pi_i}) \tag{2.23}$$

If the quantum state is in a incoherent superposition of states, each one with probability P_i to be in the state $|\psi_i\rangle$, the Postulate 3 can be applied. However, we have to know in which among possible states the system is before the measurement. In this case we can write:

$$P[m = i|s = |\phi_i] = \langle\psi_i|bf|Pi_i|\psi_i\rangle = Tr(|\psi_i\rangle\langle\psi_i|\pi_i) \tag{2.24}$$

where the possible results of the measurement is a conditional random variable.

Postulate 4 (***Composition of interecting quantum systems***). *A quantum system which is composed by two interacting quantum systems $\mathcal{H}_1, \mathcal{H}_2$ is described by a Hilbert space $\mathcal{H}$ generated from the tensorial product of two interecting systems.*

$$\mathcal{H} = \mathcal{H}_1 \otimes \mathcal{H}_2 \tag{2.25}$$

Then, if $|\psi_1\rangle$ is a state of the quantum system $\mathcal{H}_1$ and $|\psi_2\rangle$ is a state of the quantum system $\mathcal{H}_2$, the quantum state of the composite system $\mathcal{H}$ is:

$$|\psi\rangle = |\psi_1\rangle \otimes |\psi_2\rangle \tag{2.26}$$

If the compoud quantum system is generated from n interacting quantum system with states $|\psi_1\rangle, |\psi_2\rangle, ..., |\psi_n\rangle$, the compound quantum state $|\psi\rangle$ is equal to:

$$|\psi\rangle = |\psi_1\rangle \otimes |\psi_2\rangle \otimes ... \otimes |\psi_n\rangle \tag{2.27}$$

2.1.3 An elementary quantum system: The qubit

The qubit is an elementary quantum system that is modeled by a bidimensional Hilbert space. In classical information theory the information carrier is a bit that can have the value 0 and 1. In quantum information theory, not just two states can be encoded, but also a superposition of them. The unit in information is called quantum bit (*qubit*) [12].
In this space we can define an orthonormal base that can be $|0\rangle$ and $|1\rangle$. A generic state of this system can be defined with the following expression:

$$|\psi\rangle = \lambda|0\rangle + \mu|1\rangle \tag{2.28}$$

where λ and μ are complex numbers that must satisfy the condition of normalization.

$$|\lambda|^2 + |\mu|^2 = 1 \quad \text{and consequently} \quad ||\psi||^2 = 1 \tag{2.29}$$

For example, two possible states of this system are:

$$|\psi_1\rangle = \frac{1}{\sqrt{2}}|0\rangle + \frac{1}{\sqrt{2}}|1\rangle, \quad |\psi_2\rangle = \frac{i}{\sqrt{3}}|0\rangle + \frac{i+1}{\sqrt{3}}|1\rangle$$

Now, we show an application of postulate 3 on qubit quantum system. Consider a vector rappresentation of orthonormal base:

$$|0\rangle = \begin{bmatrix} 1 \\ 0 \end{bmatrix} \quad |1\rangle = \begin{bmatrix} 0 \\ 1 \end{bmatrix} \tag{2.30}$$

In order to carry out the measurement, we have to choose two orthonormal projections. In particular, we choose the two elementary projections:

$$\mathbf{\Pi}_0 = |0\rangle\langle 0| = \begin{bmatrix} 1 & 0 \\ 0 & 0 \end{bmatrix} \quad \mathbf{\Pi}_1 = |1\rangle\langle 1| = \begin{bmatrix} 0 & 0 \\ 0 & 1 \end{bmatrix} \tag{2.31}$$

From this representation it is easy to demonstrate that the two projectors generate a complete set of orthonormal projectors and satisfy the following properties:

$$\mathbf{\Pi}_0^2 = \mathbf{\Pi}_0, \quad \mathbf{\Pi}_1^2 = \mathbf{\Pi}_1$$

and

$$\mathbf{\Pi}_0\mathbf{\Pi}_1 = \begin{bmatrix} 0 & 0 \\ 0 & 0 \end{bmatrix} = \mathbf{0}_{\mathcal{H}}, \quad \mathbf{\Pi}_0 + \mathbf{\Pi}_1 = \begin{bmatrix} 0 & 0 \\ 0 & 0 \end{bmatrix} = \mathbf{I}_{\mathcal{H}}$$

The results of the measurement can have two possible values $m = \{0, 1\} \in \mathcal{M}$ and considering the state $|\psi\rangle$ before the measurement, we show that:

$$P[m = 0|\phi] = \langle\psi|0\rangle\langle 0|\psi\rangle = (\lambda^*\langle 0| + \mu^*\langle 1|)(|0\rangle\langle 0|)(\lambda|0\rangle + \mu|1\rangle) = |\lambda|^2 \quad (2.32)$$

$$P[m = 1|\phi] = \langle\psi|0\rangle\langle 0|\psi\rangle = (\lambda^*\langle 0| + \mu^*\langle 1|)(|1\rangle\langle 1|)(\lambda|0\rangle + \mu|1\rangle) = |\mu|^2 \quad (2.33)$$

Finally, we show how the quantum state collapses after the measurement.
If the result is $m = 0$:

$$|\psi_{post}\rangle = \frac{\mathbf{\Pi}_0|\psi\rangle}{|\langle\psi|0\rangle|} = \frac{|0\rangle\langle 0|(\lambda|0\rangle + \mu|1\rangle))}{\sqrt{|\lambda|^2}} = \frac{\lambda}{|\lambda|}|0\rangle \quad \rightarrow \quad |0\rangle \qquad (2.34)$$

If the result is $m = 1$:

$$|\psi_{post}\rangle = \frac{\mathbf{\Pi}_1|\psi\rangle}{|\langle\psi|1\rangle|} = \frac{|1\rangle\langle 1|(\lambda|0\rangle + \mu|1\rangle))}{\sqrt{|\mu|^2}} = \frac{\mu}{|\mu|}|1\rangle \quad \rightarrow \quad |1\rangle \qquad (2.35)$$

2.1.4 Phisycal realization of qubit system

There are several ways to implement a system that physically realizes the qubit. Some implementations have used the nuclear or electron spin, the photon polarization and ions in resonant cavities. When using photons, this means a variety of possible qubit implementations that use different properties of photons as polarization, phase, frequency, time and spatial mode.
In this thesis work we have used a system that exploits the photons polarization. This is a common choice for photonic qubits mainly due to the relative easines in manipulating polarization using half and quarter-wave plates, and polarizers. The logical state $|0\rangle$ and $|1\rangle$ are represented by the orthogonal horizontal and vertical polarization $|H\rangle$ and $|V\rangle$. The most general state which represents a qubit is:

$$|\psi\rangle = \cos\frac{\theta}{2}|H\rangle + \sin\frac{\theta}{2}e^{j\phi}|V\rangle \qquad (2.36)$$

where $|H\rangle$ and $|V\rangle$ are two orthogonal basis vector which span a two-dimensional Hilbert space.
The Poincaré sphere construction provides a convenient way of representing polarized light; on this sphere a quantum state $|\psi\rangle$ is represented by a point (Figura 2.1).

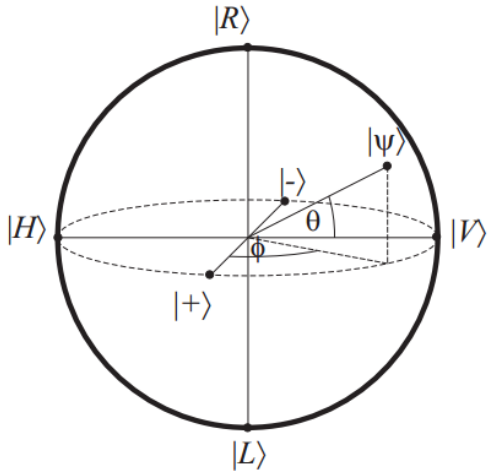

Figure 2.1: Rappresentation of the Hilber space of one qubit through the Poincaré phere.

u

In the sphere there are six special polarizations, in particular the linear horizontal $|H\rangle$ and vertical $V\rangle$ polarizations, the diagonal $|+\rangle$ and antidiagonal $|-\rangle$ polarizations and the left $|L\rangle$ and right $|R\rangle$ circular polarizations.

$$|R\rangle = \frac{1}{\sqrt{2}}|H\rangle + j|V\rangle \tag{2.37}$$

$$|R\rangle = \frac{1}{\sqrt{2}}|H\rangle - j|V\rangle \tag{2.38}$$

$$|+\rangle = \frac{1}{\sqrt{2}}|H\rangle + |V\rangle \tag{2.39}$$

$$|-\rangle = \frac{1}{\sqrt{2}}|H\rangle - |V\rangle \tag{2.40}$$

2.2 Entanglement

Entanglement plays a central role in the applications of quantum information. This phenomenon is important in *quantum criptography, quantum teleporation, quantum computation.* In postulate 4 we reported the formulation of quantum composite system; despite its simplicity it can reserve surprising aspects like entanglement. Considering a composite system C made up by two subsystems A and B, if a state vector of C cannot be written in the form of a tensor product of A and B is termed *entangled state.* In this quantum system every observable property (for example momentum and position) that

is measured in one of the two states influences directly the other one and its value will result invariably equal and opposite to the other. This result of perfect correlation between the two measurements led Einstein, Podolsky and Rosen (EPR) to write the article "Can quantum-mechanical description of physical reality be considered complete?" in 1935 [13]. This article was the answer to Heisenberg's principle of uncertainty. It says that it is not possible to determine with arbitrary precision two non commuting variables like momentum and position. But EPR considers the following: Two quantum particles interact in that way that they will have opposite momentum and will be separated. After some time one can measure the momentum of one of the particles and can make predictions about the other's momentum. By measuring the position of the second particle, one knows the position of its counterpart. So at least both the position and the momentum of a system are known. Considering every physical theory as local and real, they argued that quantum mechanics could not be complete as it cannot describe these values, and that "hidden variables" had to be introduced to provide a compleate theory. It was J. S. Bell, in 1964 [14], that finally proved EPR paradox to be wrong. He stated that for a quantum theory in which there are hidden variables and in which principles of reality and locality are true, inequality relations between measurements of related particles should sussist.

2.2.1 A system of two qubits

Now we show the notion of two tensors product by constructing the space of a two qubits systems. The spaces of states of the two qubits are the two-dimensional Hilbert space $\mathcal{H}_1$ and $\mathcal{H}_2$. The spaces of states of the composite system of two qubits $\mathcal{H} = \mathcal{H}_1 \otimes \mathcal{H}_2$ is a four-dimensional space.

$$dim(\mathcal{H}_1 \otimes \mathcal{H}_2) = dim(\mathcal{H}_1) \times dim(\mathcal{H}_2) \tag{2.41}$$

We choose the orthonormal bases of $\mathcal{H}_1$ and $\mathcal{H}_2$ that are $\{|0\rangle_1, |1\rangle_1\}$ and $\{|0\rangle_2, |1\rangle_2\}$ and consider $|\psi_1\rangle$ and $|\psi_2\rangle$ as two normalized vectors of the respective Hilbert spaces.

$$\begin{aligned} |\psi_1\rangle &= \lambda_1|0\rangle_1 + \mu_1|1\rangle_1, \quad |\lambda_1|^2 + |\mu_1|^2 = 1, \\ |\psi_2\rangle &= \lambda_2|0\rangle_2 + \mu_2|1\rangle_2, \quad |\lambda_2|^2 + |\mu_2|^2 = 1, \end{aligned} \tag{2.42}$$

According of the 2.26, the tensor product of the two states $|\psi_1\rangle$ and $|\psi_2\rangle$ is equal to:

$$|\psi\rangle = \lambda_1\lambda_2(|0\rangle_1 \otimes |0\rangle_2) + \lambda_1\mu_2(|0\rangle_1 \otimes |1\rangle_2) + \lambda_2\mu_1(|0\rangle_1 \otimes |1\rangle_2) + \mu_1\mu_2(|1\rangle_1 \otimes |1\rangle_2) \tag{2.43}$$

We indicate the orthonormal basis of the composite system in the following notation:

$$\{|00\rangle, |01\rangle, |10\rangle, |11\rangle\} \tag{2.44}$$

The generic vector $|\psi\rangle \in \mathcal{H}$ is:

$$|\psi\rangle = a|00\rangle + b|01\rangle + c|10\rangle + d|11\rangle \tag{2.45}$$

If we compare the expressions (2.43) and (2.45), we see that a tensor product vector satisfies:

$$ad = bc \tag{2.46}$$

Anyway, there is no reason for which this condition should be necessary and sufficient to be valid. The state vectors that satisfy (2.46) belong to a subset of the whole Hilbert space ($\mathcal{H}_1 \otimes \mathcal{H}_2$). Consider the following state:

$$|\phi\rangle = \frac{1}{\sqrt{2}}(|00\rangle + |11\rangle) \tag{2.47}$$

This state is called entangled and it is a quantum state of the Hilbert space $\mathcal{H}$ but it does not satisfy the relation (2.46) because:

$$a = d = \frac{1}{\sqrt{2}}, \quad b = c = 0, \quad ad = \frac{1}{2} \neq 0 = bc \tag{2.48}$$

2.2.2 Entangled states

In the previous section we have seen a particular case of state that cannot be described as a tensor product of two qubits systems.

$$|\psi\rangle \neq |\psi_1\rangle \otimes |\psi_2\rangle \tag{2.49}$$

The most common two-systems entangled states are the *Bell states*:

$$|\Phi^+\rangle = \frac{1}{\sqrt{2}}(|00\rangle + |11\rangle) \tag{2.50}$$

$$|\Phi^-\rangle = \frac{1}{\sqrt{2}}(|00\rangle - |11\rangle) \tag{2.51}$$

$$|\Psi^+\rangle = \frac{1}{\sqrt{2}}(|01\rangle + |10\rangle) \tag{2.52}$$

$$|\Psi^-\rangle = \frac{1}{\sqrt{2}}(|01\rangle - |10\rangle) \tag{2.53}$$

These states are maximally entangled that means that they all give a maximal violation of Bell's inequality or the following form of the CHSH inequality.

We see that when a system collapses into one of the two states $|0\rangle$ or $|1\rangle$, the other one is completely determined. It is also important to note that a measurement in another basis like $|+\rangle, |-\rangle$, does not affect the correlations between the systems; a measurement of one of the systems will again completely determine the state of the other system. This is a key property of entanglement; the correlations remain under local operations.
Entangled states can be realized in several physical systems. Here however, we will only discuss photonic entanglement created using spontaneous parametric downconversion in nonlinear crystals.

2.2.3 Realization of polarization entangled qubits

The most common choice in experimental realizations of entanglement is the use of polarization entanglement. When using SPDC to generate photon pairs, the entanglement can either be created directly or by post-selection. A typical setup creating entanglement by post-selection is when a type-I phase matching process is used. The two downconverted photons are then emitted on two opposite directions located on cone centered around the pump beam. If the polarization of one beam is rotated by 90° and the two beams are subsequently combined on a beam splitter, a polarization-entangled state is obtained for those events when the two photons exit in separate output ports of the beam splitter. In this way, the state generated is:

$$|\psi\rangle = \frac{1}{\sqrt{2}}(|HH\rangle) + |VV\rangle) \tag{2.54}$$

Alternatively, a type-II source can be used to create entangled states where the two photons are then sent to two input ports of a beam splitter. Selecting the events when the photons exit different output ports give a polarization-entangled state of the form:

$$|\psi\rangle = \frac{1}{\sqrt{2}}(|HV\rangle) + |VH\rangle) \tag{2.55}$$

Entanglement created directly can be achieved by using non-collinear emission in type-II phase matching. The signal and idler are then emitted on two intersection cones with opposite polarization. If the intersection points are selected, a polarization-entangled state is obtained and this state has the same form of 2.55 but by quarter and half-wave plates any of the four Bell states can be obtained.

Chapter 3

Nonlinear Optics

Nonlinear optics effects are not observed when the light travels in free space. The "non linearity" resides in the medium through which the ligth travels, rather than in the light itself. The iteraction of light with light is therefore mediated by the nonlinear medium and the presence of an optical field modifies the properties of the medium, which in turn causes another optical field, or even the original field itself, to be modified [15].
These interactions that generate the nonlinear effects take place when a material interacts with an intense ligth so that its response yields fundamentally different properties than the ones observed in the linear regime. As a consequence, until the development of laser in 1960, there was no way to observe nonlinear optics effects, although theoretical predictions were formulated in 1931. The first experiment of nonlinear phenomena was observed in 1961 by Franken et al [16], who detected the frequency doubling of a radiation passing through a nonlinear crystal. This process was interpreted as the generation of second harmonic.
Starting from 1961, research on nonlinear phenomena has discovered a large number of these nonlinear iterations, whose applications can be found in various fields such as physics, chemistry, biology and engineering.
In this dissertation we adopted two fundamental non-linear effects:

1. Second Harmonic Generation (SHG)

2. Spontaneous Parametric Down Conversion (SPDC)

and in this chapter we will focus on the theoretical study of these two phenomena.

3.1 Nonlinear Maxwell's wave equations

It is well known that in a linear dielectric medium the relation between the polarization density and the electric field is linear.

$$\mathbf{P} = \varepsilon_0 \chi^{(1)} \mathbf{E} \tag{3.1}$$

where $\chi^{(1)}$ is a tensor called linear susceptibility, which is related to the dielectric constant and the refractive index of the material by $n^2 = \epsilon \,/\, \epsilon_0 = 1 + \chi^{(1)}$. However, if we consider a nonlinear dielectric medium the relation is nonlinear, in particular when the electric field is small the relation between $\mathbf{P}$ and $\mathbf{E}$ is linear but, when the electric field is intense ($\sim 10^5 - 10^8$ V/m) the relation becomes nonlinear.

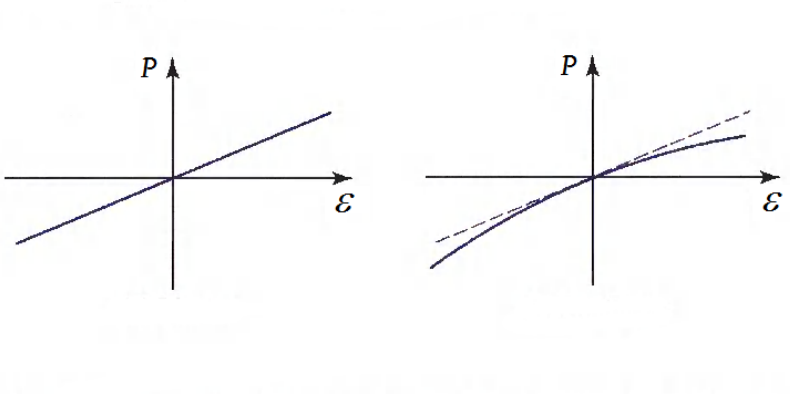

Figure 3.1: The **P**-**E** relation for a linear dielectric medium on the left and a nonlinear dielectric medium on the right .

Under the condition of strong fields in the medium, we can expand the relation beetween **P**-**E** in a Taylor series.

$$\mathbf{P} = \varepsilon_0 \chi^{(1)} \mathbf{E} + \varepsilon_0 \chi^{(2)} \mathbf{EE} + \varepsilon_0 \chi^{(3)} \mathbf{EEE} + ... \tag{3.2}$$

$$\mathbf{P} = \varepsilon_0 \chi^{(1)} \mathbf{E} + \mathbf{P}_{NL} \tag{3.3}$$

$$\mathbf{P}_{NL} = \varepsilon_0 \chi^{(2)} \mathbf{EE} + \varepsilon_0 \chi^{(3)} \mathbf{EEE} + ... \tag{3.4}$$

We consider the Maxwell's equation for electro-magnetic fields interacting

with matter.

$$\nabla \times \mathbf{E} = -\frac{\partial \mathbf{B}}{\partial t} \tag{3.5}$$

$$\nabla \times \mathbf{H} = \frac{\partial \mathbf{D}}{\partial t} \tag{3.6}$$

$$\nabla \cdot \mathbf{B} = 0 \tag{3.7}$$

$$\nabla \cdot \mathbf{D} = 0 \tag{3.8}$$

where $\mathbf{E} = \mathbf{E}(\mathbf{r}, \mathbf{t})$ is the electric field, $\mathbf{H}$ is the magnetic flux density, $\mathbf{B} = \mathbf{B}(\mathbf{r}, \mathbf{t})$ is the magnetic field and $\mathbf{D} = \varepsilon_0 \mathbf{E} + \mathbf{P}$ is the electric displacement vector with $\mathbf{P}$ polarization vector.
Taking into account the definition of vector Laplace operator $\nabla^2 \mathbf{A}$ of a generic vector field $\mathbf{A}$, $\nabla^2 \mathbf{A} = \nabla(\nabla \cdot \mathbf{A}) - \nabla \times \nabla \times \mathbf{A}$, and combining equation (3.4) with (3.5) we obtain the wave equation for an arbitrary homogeneous, isotropic dielectric medium.

$$\nabla^2 \mathbf{E} - \frac{1}{c^2} \frac{\partial^2 \mathbf{E}}{\partial t^2} = \mu_0 \frac{\partial^2 \mathbf{P}}{\partial t^2} \tag{3.9}$$

where $c = c_0/n$ is the speed of light in the dielectric medium.
Now, if we consider an arbitrary homogeneous and isotropic dielectric medium passing through a strong optical field, the wave equation (3.8) has to be rewritten as [15]:

$$\nabla^2 \mathbf{E} - \frac{1}{c^2} \frac{\partial^2 \mathbf{E}}{\partial t^2} = -\mathbf{S} \tag{3.10}$$

$$\mathbf{S} = -\mu_0 \frac{\partial^2 \mathbf{P}_{NL}}{\partial t^2} \tag{3.11}$$

This is the fundamental equation that underlies the theory of nonlinear optics, where the term $\mathbf{S}$ can be considered as a source that radiates in a linear medium of refractive index n.
The equation (3.9) is recursive because an incident electric field $\mathbf{E}_0$ in a nonlinear medium generates a radiation source $\mathbf{S}_0$ that radiates a new field $\mathbf{E}_1$. In turn, this new field generates a radiation source $\mathbf{S}_1$ that radiates a new field $\mathbf{E}_2$ and so on.
There are two approximate approaches to solve this nonlinear wave equation: **Scattering theory of nonlinear optics** or Born approximation and **Coupled-wave theory**.
We are interested in the theoretical analysis of second-order nonlinear phenomena, in particular **Second Harmonic Generation (SHG)** and **Spontaneous Parametric Down Conversion (SPDC)**.

For this reason we consider the relationship between $\mathbf{P}$ and $\mathbf{E}$ expanded in a Taylor series up to the second order.

$$\mathbf{P} = \varepsilon_0 \chi^{(1)} \mathbf{E} + \mathbf{P}_{NL} \tag{3.12}$$

$$\mathbf{P}_{NL} = \varepsilon_0 \chi^{(2)} \mathbf{E}\mathbf{E} \tag{3.13}$$

3.2 Properties of nonlinear susceptibility

The susceptibilities are proportional factors that convert the electric field vector in the polarization vector. In general, materials used in nonlinear optics have anisotropic structure. The anisotropic media are formed by molecules organized in space according to a regular pattern and oriented in the same direction. For this reason, the macroscopic optical properties in anisotropic media depend on direction and an important property is that polarization vector is never parallel with electric field vector. Accordingly, the susceptibility is a tensor which correlates the polarization direction with the three components of the electric field. A generic susceptibily $\chi^{(n)}$ is a tensor with rank $n+1$ and 3^{n+1} elements.
We consider the second order nonlinear susceptibily only and the mutual interaction of three waves of frequency $\omega_1,\ \omega_2,\ \omega_3 = \omega_1 + \omega_2$. The interaction of these waves requires that we know the expression of nonlinear polarization $\mathbf{P}(\omega_i)$ as follows [17]:

$$\mathbf{P}_i(\omega_n + \omega_m) = \varepsilon_0 \sum_{jk} \sum_{(nm)} \chi^{(2)}_{ijk}(\omega_n + \omega_m,\ \omega_n,\ \omega_m) \mathbf{E}_j(\omega_n) \mathbf{E}_k(\omega_m) \tag{3.14}$$

From this equation we determin six susceptibility tensor vectors:

$$\chi^{(2)}_{ijk}(\omega_1, \omega_3, -\omega_2), \qquad \chi^{(2)}_{ijk}(\omega_1, -\omega_2, \omega_3),$$
$$\chi^{(2)}_{ijk}(\omega_2, \omega_3, -\omega_1), \qquad \chi^{(2)}_{ijk}(\omega_2, -\omega_1, \omega_3),$$
$$\chi^{(2)}_{ijk}(\omega_3, \omega_1, \omega_2), \qquad \chi^{(2)}_{ijk}(\omega_3, \omega_2, \omega_1).$$

and six additional tensors in which each frequency is replaced by it is negative. Since each of these 12 tensors thus consists of 27 Cartesian components, as many as 324 different (complex) number need to be specified in order to describe the interaction.
Fortunately there are some semplifications and properties resulting from symmetries, which reduce the number of variables needed to describe the susceptibility tensor.

3.2.1 Intrinsic permutation symmetry

Intrinsic permutation symmetry is a fundamental property of the nonlinear susceptibily which derives from the principles of causality and time invariance.
We consider a generic term of the nonlinear susceptibily, for example:

$$P_i(\omega_n + \omega_m) = \varepsilon_0 \chi^{(2)}_{ijk}(\omega_n + \omega_m,\ \omega_n,\ \omega_m)\mathbf{E}_j(\omega_n)\mathbf{E}_k(\omega_m)$$

Now, we can write this contribution interchanging n with m and j with k.

$$P_i(\omega_n + \omega_m) = \varepsilon_0 \chi^{(2)}_{ikj}(\omega_n + \omega_m,\ \omega_m,\ \omega_n)\mathbf{E}_k(\omega_m)\mathbf{E}_j(\omega_n)$$

These two expressions are numerically equal if we require the nonlinear susceptibily to be unchanged by the simultaneous interchange of its last two frequency arguments and its last two Cartesian indices:

$$\chi^{(2)}_{ijk}(\omega_n + \omega_m,\ \omega_n,\ \omega_m) = \chi^{(2)}_{ikj}(\omega_n + \omega_m,\ \omega_m,\ \omega_n) \tag{3.15}$$

This property is know as intrinsic permutation symmetry and in general, if we have a generic nth-order susceptibily $\chi^{(n)}_{\alpha_1,\alpha_2,...,\alpha_n}(\sum_{i=1,...,n}\omega_i, \omega_1, \omega_2, ..., \omega_n)$, this quantity is invariant under all $n!$ permutation of $\omega_1, \omega_2, ..., \omega_n$.
When all of the optical frequencies are detuned from the resonance frequencies of the optical medium, the permutation can be extended to the first Cartesian index i, refering to induced frequency $\omega_n + \omega_m$.. This new symmetry is called **full permutation symmetry**, that implies, for instance, the following equality:

$$\chi^{(2)}_{ijk}(\omega_3 = \omega_1 + \omega_2) = \chi^{(2)}_{jki}(-\omega_1 = \omega_2 - \omega_3) \tag{3.16}$$

3.2.2 Reality of the fields

The nonlinear polarization describing the sum-frequency responce to input field at frequencies ω_n and ω_m has been represented as:

$$\widetilde{\mathbf{P}}_i(\boldsymbol{r}, t) = P_i(\omega_n + \omega_m)e^{-j(\omega_n+\omega_m)t} + P_i(-\omega_n - \omega_m)e^{j(\omega_n+\omega_m)t} \tag{3.17}$$

and the monocromatic electric fields have been represented as:

$$\begin{aligned} \widetilde{\mathbf{E}}_j(\boldsymbol{r}, t) &= E_j(\omega_n)e^{-j\omega_n t} + \ c.c \\ \widetilde{\mathbf{E}}_k((\boldsymbol{r}, t) &= E_k(\omega_m)e^{-j\omega_m t} + \ c.c \end{aligned} \tag{3.18}$$

The electric fields $\widetilde{\mathbf{E}}_j(\boldsymbol{r},t)$, $\widetilde{\mathbf{E}}_k((\boldsymbol{r},t)$ and the nonlinear polarization $\widetilde{\mathbf{P}}_i(\boldsymbol{r},t)$ are physically measurable quantities and they must be purely real.Consequently the relations between positive and negative frequency components have hermitian symmetry.

$$E_j(-\omega_n) = E_j(\omega_n)^*, \qquad E_k(-\omega_m) = E_j(\omega_m)^* \tag{3.19}$$

$$P_i(-\omega_n - \omega_m) = P_i(\omega_n + \omega_m)^* \tag{3.20}$$

From equation 3.14 we conclude that the positive and negative frequency components of the susceptibility must be related according to:

$$\chi^{(2)}_{ijk}(-\omega_n - \omega_m,\ -\omega_n,\ -\omega_m) = \chi^{(2)}_{ijk}(\omega_n + \omega_m,\ \omega_n,\ \omega_m)^* \tag{3.21}$$

3.2.3 Kleinman's Symmetry

Quite often nonlinear optical interactions involve optical waves whose frequencies ω_i are much smaller then the lowest resonance frequency of the material system. Under these conditions, the nonlinear susceptibility is essentially frequency indepent. Moreover, under the condition of low-frequency exitation the system responds istantaneously to the applied field, and the nonlinear polarization can be described in the time domain by the relation [17]:

$$\widetilde{P}(t) = \varepsilon_0 \chi^{(2)} \widetilde{E}^2(t) \tag{3.22}$$

where $\chi^{(2)}$ can be taken to be a costant.
Consider the interaction of three waves of frequencies ω_1, ω_2, and $\omega_3 = \omega_1 + \omega_2$. If the medium is characterized by lossless and the applied field frequencies ω_i, with $i = 1, 2, 3$, are much smaller than the resonance frequency ω_0, then the condition of full permutation symmetry must be valid. However if it is valid also the condition that the nonlinear susceptibility is frequencies indipendent, we can permute the indices without permuting the frequencies:

$$\begin{aligned}\chi^{(2)}_{ijk}(\omega_3 = \omega_1 + \omega_2) = \chi^{(2)}_{jki}(\omega_3 = \omega_1 + \omega_2) = \chi^{(2)}_{kij}(\omega_3 = \omega_1 + \omega_2) = \\ = \chi^{(2)}_{ikj}(\omega_3 = \omega_1 + \omega_2) = \chi^{(2)}_{jik}(\omega_3 = \omega_1 + \omega_2) = \chi^{(2)}_{kji}(\omega_3 = \omega_1 + \omega_2)\end{aligned} \tag{3.23}$$

This result is know as the Kleinman symmetry condition.

3.3 The d-coefficient

Now, we introduce a new nonlinear coefficient, the tensor d that is defined as follows:

$$d_{ijk} = \frac{1}{2}\chi^{(2)}_{ijk} \tag{3.24}$$

where the factor 1/2 is a consequence of historical conventions.
The nonlinear coefficient d, is more frequently used than $\chi^{(2)}$. In general the tensor d_{ijk} is a matrix of $3x3x3 = 27$ elements, but under the condition of intrinsic permutation symmetry the j and k indices of $\chi^{(2)}_{ijk}$ are interchangeable. We define a contracted notation where indices j and k together are replaced by the index l and the tensor d can take on following expression:

$$d_{il} = \frac{1}{2}\chi^{(2)}_{ijk} \tag{3.25}$$

where:

$jk:$	11	22	33	23, 32	13, 31	12, 21
$i:$	1	2	3	4	5	6

The number of indipendent elements are thereby reduced from 27 to 18 and the nonlinear coefficient d, can be rapresented with the following matrix:

$$d_{il} = \begin{bmatrix} d_{11} & d_{12} & d_{13} & d_{14} & d_{15} & d_{16} \\ d_{21} & d_{22} & d_{23} & d_{24} & d_{25} & d_{26} \\ d_{31} & d_{32} & d_{33} & d_{34} & d_{35} & d_{36} \end{bmatrix} \tag{3.26}$$

The number of indipendent components of nonlinear d-matrix, decrease from 18 to 10 when the Kleinman symmetry condition are valid. Therefore, when all frequencies involved in the interaction are far away from any resonance frequencies of the nonlinear material, the d-matrix is simplified within the following form:

$$d_{il} = \begin{bmatrix} d_{11} & d_{12} & d_{13} & d_{14} & d_{15} & d_{16} \\ d_{16} & d_{22} & d_{23} & d_{24} & d_{14} & d_{12} \\ d_{15} & d_{24} & d_{33} & d_{23} & d_{13} & d_{14} \end{bmatrix} \tag{3.27}$$

For example if we consider the element d_{32}, we see that:

$$d_{32} \equiv d_{322} = d_{232} = d_{223} \equiv d_{24}$$

If we apply the same argument of the elements in (3.26), the d-matrix is simplified within (3.27).
The complete expression of the second-order polarization vector, in the case of second harmonic generation using d-matrix notation is:

$$\begin{bmatrix} P_x(2\omega) \\ P_y(2\omega) \\ P_z(2\omega) \end{bmatrix} = 2\varepsilon_0 \begin{bmatrix} d_{11} & d_{12} & d_{13} & d_{14} & d_{15} & d_{16} \\ d_{16} & d_{22} & d_{23} & d_{24} & d_{14} & d_{12} \\ d_{15} & d_{24} & d_{33} & d_{23} & d_{13} & d_{14} \end{bmatrix} \begin{bmatrix} P^2_x(\omega) \\ P^2_y(\omega) \\ P^2_z(\omega) \\ 2P^2_y(\omega)P^2_z(\omega) \\ 2P^2_x(\omega)P^2_z(\omega) \\ 2P^2_x(\omega)P^2_y(\omega) \end{bmatrix} \tag{3.28}$$

In the following chapter we will resume this expression of polarization vector and it will be semplified in the application of SHG in KTP and PPKTP crystal. Furthermore, we will show that if the beam propagation direction and polarization are fixed, it is possible to express the nonlinear polarization by scalar relationship.

$$P(2\omega) = 2\varepsilon_0 d_{eff} E^2(\omega) \tag{3.29}$$

where the parameter d_{eff} is the effective value of d obtained from d-matrix. The value of d_{eff} depends on the polarization directions of the incident fields and on the phasematching conditions.

3.4 Second-order nonlinear optics

In this section we will explain the optical property of a nonlinear medium characterized by second-order nonlinearities only; the nonlinearities of higher order than the second are negligible. We can consider the nonlinear polarization vector composed by second-order term only and the expression of $\mathbf{P}_{NL}$ in function of d coefficient is:

$$\mathbf{P}_{NL} = 2d\mathcal{E}^2 \tag{3.30}$$

In this theoretical analysis of second-order nonlinear phenomena, we used the scattering theory of non-linear optics, in particular the first Born approximation.

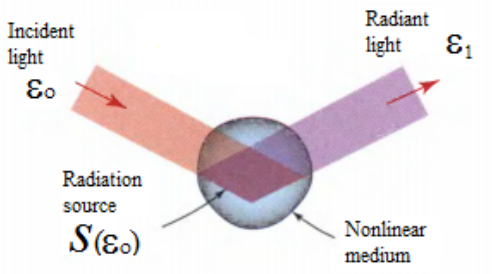

Figure 3.2: The first Born approximation

Consider a monocromatic field of angular frequency ω and complex amplitude $E(\omega)$ through a second-order nonlinear medium.

$$\mathcal{E}(t) = \boldsymbol{Re}\{E(\omega)exp(j\omega t)\} = \frac{1}{2}E(\omega)exp(j\omega t) + \frac{1}{2}E(\omega)^* exp(-j\omega t) \tag{3.31}$$

Now, we calculate the expression of nonlinear polarization density $\mathbf{P}_{NL}$ in the presence of a monocromatic field.

$$\mathbf{P}_{NL} = 2d\left[\frac{1}{2}E(\omega)exp(j\omega t) + \frac{1}{2}E(\omega)^* exp(-j\omega t)\right]^2 =$$

$$= 2d\left[\frac{1}{4}E(\omega)^2 exp(j2\omega t) + \frac{1}{4}E(\omega)^{2*} exp(-j2\omega t) + \frac{1}{2}E(\omega)E(\omega)^*\right];$$

$$\mathbf{P}_{NL} = P_{NL}(0) + \boldsymbol{Re}\{P_{NL}(2\omega)exp(j\omega t)\} \tag{3.32}$$

where

$$P_{NL}(0) = dE(\omega)E(\omega)^* \quad \textbf{Optical Rectification} \tag{3.33}$$

$$P_{NL}(2\omega) = dE(\omega)^2 \quad \textbf{Second Harmonic Generation} \tag{3.34}$$

This optical process is a degenerate special case (when $\omega = \omega_1 = \omega_2$) of a much wider class of nonlinear optical processes that we know as three wave mixing.
Now consider the general case of a electric field $\mathcal{E}(t)$ composed by two monocromatic components at optical frequencies ω_1 and ω_2.

$$\mathcal{E}(t) = \boldsymbol{Re}\{E(\omega_1)exp(j\omega_1 t) + E(\omega_2)exp(j\omega_2 t)\} =$$

$$= \frac{1}{2}\left[E(\omega_1)exp(j\omega_1 t) + E(\omega_1)^* exp(-j\omega_1 t)\right] + \frac{1}{2}\left[E(\omega_2)exp(j\omega_2 t) + E(\omega_2)^* exp(-j\omega_2 t)\right] \tag{3.35}$$

The relative nonlinear polarization density $\mathbf{P}_{NL}$ is obtained by substituting the electric field expression in (3.30). From this calculation we obtain five optical components at different frequencies, with amplitudes:

$$P_{NL}(0) = d\left[|E(\omega_1)|^2 + |E(\omega_2)|^2\right] \tag{3.36}$$

$$P_{NL}(2\omega_1) = dE(\omega_1)^2 \tag{3.37}$$

$$P_{NL}(2\omega_2) = dE(\omega_2)^2 \tag{3.38}$$

$$P_{NL}(\omega_1 + \omega_2) = 2dE(\omega_1)E(\omega_2) \tag{3.39}$$

$$P_{NL}(\omega_1 - \omega_2) = 2dE(\omega_1)E(\omega_2)^* \tag{3.40}$$

The interation of two optical waves at different frequencies generate a third wave at sum frequency or different frequency. This process is called **OFC**(Optical Frequency Conversion).
The optical process that we can obtain from the three wave mixing are much more and they are known as a **parametric iteration processes**. They take a variety of forms, depending on which of the three waves interacts in the input with the medium and which are extracted as outputs.

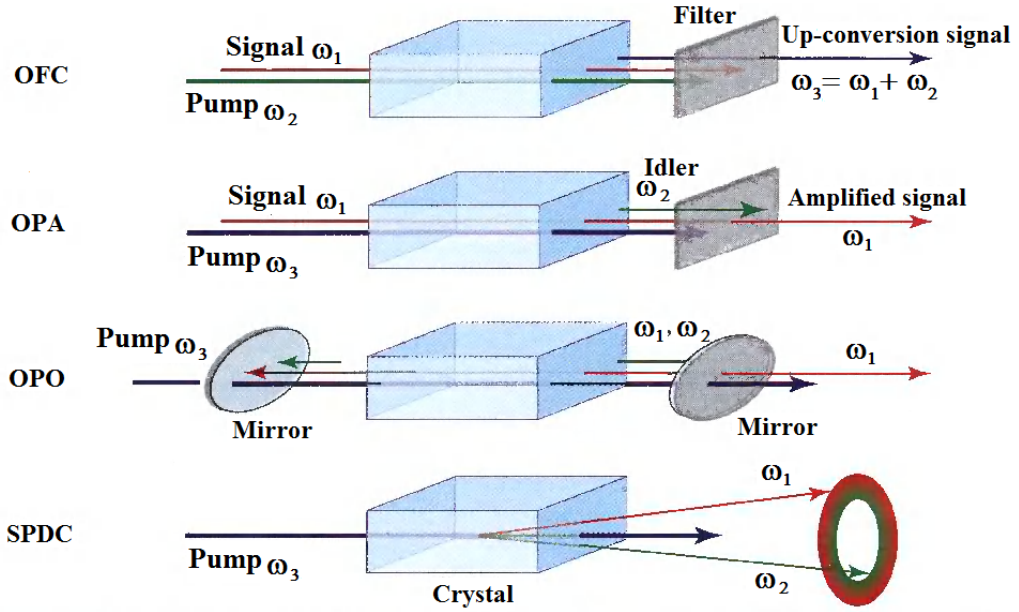

Figure 3.3: optical frequency conversion (OFC); optical parametric amplifier (OPA); optical parametric oscillator (OPO), spontaneous parametric down conversion (SPDC).

3.5 Second harmonic generation in bulk material

3.5.1 The coupled wave theory

Secon harmonic generation can be seen as a special case of three waves mixing where the two input interactive waves have the same frequency ω_F and the third wave generated from this iteraction has frequency $\omega_{SH} = \omega_F + \omega_F$.
One method to solve the nonlinear wave equation is the coupled wave theory. To simplify the solution we have to make several assumptions. We consider the SHG in a lossless nonlinear medium and the electromagnetic waves are quasi-monochromatic plane waves and propagate along z-axis. Then, electric field can be written as:

$$\mathcal{E}(z,t) = \frac{1}{2}[E(z,\omega)e^{-j(k_F z-\omega t)} + c.c] \tag{3.41}$$

In according to equation (3.29) we can write $\mathbf{P}_{NL} = P(2\omega) = 2d_{eff}E(z,\omega)^2$ and if now substitute equation (3.41) in nonlinear wave equation (3.9) we

obtain:

$$\frac{\partial^2 E_{SH}(z,\omega)}{\partial z^2} e^{-j(k_{SH}z-\omega t)} - \frac{n^2}{c_o^2}\frac{\partial^2 E_{SH}(z,\omega)}{\partial t^2} e^{-j(k_{SH}z-\omega t)} = \frac{\partial^2 E_F(z,\omega)}{\partial t^2} e^{-j(2k_F z-\omega t)} \tag{3.42}$$

where we have to replace ∇^2 with $\partial^2/\partial z^2$ because we have considered the electric field depending only from the cordinate z and independent from x and y cordinates during the propagation.

$$\left[\frac{\partial^2 E_{SH}(z,\omega)}{\partial z^2} - jk\frac{\partial E_{SH}(z,\omega)}{\partial z} + k^2 E_{SH}(z,\omega) - \frac{n^2\omega_F^2}{c_0^2} E_{SH}(z,\omega)\right] e^{-j(k_{SH}z-\omega t)} =$$

$$= -\frac{2d_{eff}\omega^2}{c_0^2} E_F(z,\omega)^2 e^{-j(2k_F z-\omega t)}.$$

Since $k^2 = n^2\omega^2/c_0^2$ we can rewrite the equation as:

$$\frac{\partial^2 E_{SH}(z,\omega)}{\partial z^2} - jk\frac{\partial E_{SH}(z,\omega)}{\partial z} = -\frac{2d_{eff}\omega^2}{c_0^2} E_F(z,\omega)^2 e^{j(\Delta k z)} \tag{3.43}$$

where $\Delta k = k_{SH} - 2k_F$.

We also assume that the envelop of the plane waves changes slowly with rispect to the distance. Then, the second order derivation with respect to the distance can be neglected respect to the first order of derivation. This approximation is called SVEA (Slowly Varing Envelop Approximation).

$$\left|\frac{\partial^2 E_{SH}(z,\omega)}{\partial z^2}\right| \ll \left|k\frac{\partial E_{SH}(z,\omega)}{\partial z}\right| \tag{3.44}$$

Under this last consideration we can write the following approximation equation:

$$\frac{\partial E_{SH}(z,\omega)}{\partial z} = \frac{2d_{eff}\omega^2}{k_{SH}c_0^2} E_F(z,\omega) E_F(z,\omega) e^{j(\Delta k z)} \tag{3.45}$$

During propagation in the medium, the amplitude of each interacting wave is influenced by the effect of other waves on itself. Then, each of the complex amplitude of the interacting waves satisfies the Helmholtz equation, as (3.10), with a source depending on the electric fields of the other waves.

Therefore the waves are coupled and in the case of SHG the coupled equation of the process are:

$$\begin{aligned}\frac{\partial E_{SH}(z,\omega)}{\partial z} &= \frac{j\omega d_{eff}}{n_{SH}c_0} E_F(z,\omega) E_F(z,\omega) e^{j(\Delta k z)} \\ \frac{\partial E_F(z,\omega)}{\partial z} &= \frac{j\omega d_{eff}}{n_F c_0} E_{SH}(z,\omega) E_F(z,\omega)^* e^{j(\Delta k z)}\end{aligned} \tag{3.46}$$

If we assume the system in non depletion pump condition, in that case $\partial E_F/\partial z = 0$ and the complex amplitude of second harmonic wave depens only from the first equation of (3.46).

3.5.2 Intensity of SHG

Now, we consider L the lenght of crystal along the z-axis and the assumption of non depletion pump condition. The amplitude of the SH field at the output interface $z = L$ is equal to:

$$E_{SH}(L) = \frac{\omega d_{eff}}{n_{SH} c_0^2} E_F^2 \int_0^L j e^{\Delta k z} dz = \frac{\omega d_{eff} E_F^2}{n_{SH} c_0^2} \left(\frac{e^{j\Delta k L} - 1}{j\Delta k} \right). \tag{3.47}$$

The intensity of the interacting waves is given by:

$$Ii = \frac{1}{2} \epsilon_0 n_i c_0 |E_i|^2, \quad i = SH; F \tag{3.48}$$

we thus obtain:

$$I_{SH} = \frac{2\omega^2 d_{eff}^2 I_F^2}{n_{SH} c_0^3 n_F^2 \epsilon_0} \left| \frac{e^{j\Delta k L} - 1}{j\Delta k} \right|^2 \tag{3.49}$$

where the squared modulus in the last equation can be developed as follows:

$$\left| \frac{e^{j\Delta k L} - 1}{j\Delta k} \right|^2 = L^2 \left(\frac{e^{j\Delta k L} - 1}{\Delta k L} \right) \left(\frac{e^{-j\Delta k L} - 1}{\Delta k L} \right) = L^2 \left(\frac{2 - e^{j\Delta k L} - e^{-j\Delta k L}}{(\Delta k L)^2} \right) =$$

$$= 2L^2 \frac{(1 - cos\Delta k L)}{(\Delta k L)^2} = L^2 \frac{sin^2(\Delta k L/2)}{(\Delta k L)^2} \equiv L^2 sinc^2 \left(\frac{\Delta k L}{2} \right). \tag{3.50}$$

The final expression of SH intensity, generated from the interaction of the fundamental wave with intensity I_F with a nonlinear medium of lenght L is:

$$I_{SH} = \frac{2 d_{eff}^2 \omega^2 L^2 I_F^2}{\epsilon_0 c_0^3 n_{SH} n_F^2} sinc^2 \left(\frac{\Delta k L}{2} \right). \tag{3.51}$$

This relationship tells us that, the SHG output intensity has a quadratic dependence on the fundamental intensity I_F, as well as on the length of the nonlinear crystal in the case of plane waves and finaly it depends on a $sinc^2$-curve in function of the mismatch $|\Delta|k$. If $\Delta k = 0$ the $sinc^2 = 1$ and the SH outpu intensity reaches the maximum.
We can rewrite the function in the following expression:

$$I_{SH} = I_{SH}^{max} sinc^2 \left(\frac{\Delta k L}{2} \right). \tag{3.52}$$

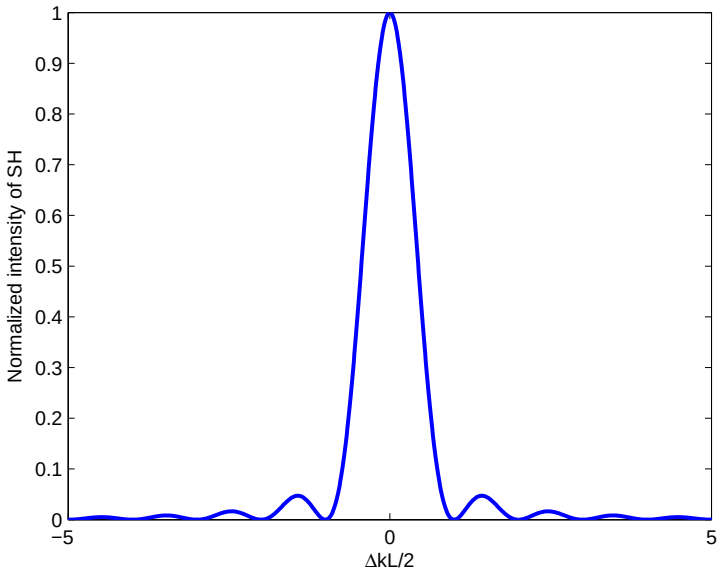

Figure 3.4: Normalized intensity of SHG as a function of $\Delta kL/2$

where $I_{SH}^{max} = \frac{2d_{eff}^2\omega^2L^2I_F^2}{\epsilon_0 c_0^3 n_{SH} n_F^2}$.
It should be noted that the efficiency of SH generation decreases as $|\Delta k|L$ increases. The condition on Δk generates a reduction of SH intensity and efficiency by a factor that is inversely proportional to length L. Futhermore with increasing length, the phase-mismatch Δk becomes more and more stringent. We define a **coherence length** L_c as:

$$L_c = \frac{2\pi}{\Delta k} \tag{3.53}$$

It idicates the maximum length within which the parametric interaction process is efficient. When the phase-matching fails it means that there will be destructive interference between wavelenghts generated at different points in the crystal. For instance, in the case of SHG, we have defined the phase-matching as $\Delta k = k_{SH} - 2k_F$ and the coherence length is equal to:

$$L_c = \frac{\lambda}{2(n_{SH} - 2n_F)} \tag{3.54}$$

3.6 Phase matching condition

We have already seen that the incident of two waves at frequencies ω_1 and ω_2 may generate a new waves at frequecies $0, 2\omega_1, 2\omega_2, \omega_1 + \omega_2, \omega_1 - \omega_2$, but all

of these waves are not necessarly generated. If we want generate a specific new wave some additional conditions must be satisfied.

$$\omega_1 + \omega_2 = \omega_3 \tag{3.55}$$

$$k_1 + k_2 = k_3 \tag{3.56}$$

These conditions are called **frequency and phase matching conditions**. They indicate that in optical processes the energy and momentum must be conserved.
In the last section we have seen that the phase-matching condition is very important to achieve the maximum intensity of conversion. The condition $\Delta k = 0$ is often difficult to achieve because the bulk materials are affected by normal dispersion. This effect causes a variation of refractive index in function of frequency. Unfortunely, due to material dispersion $n_{SH} \neq n_F$, and this condition often causes the non perfect phase-matching $\Delta k \neq 0$. It is usually compensate the dispersion using property of birefringence which is present in nonlinear crystal and in general in anisotropic medium. For an anisotropic medium, the refractive indeces n_{SH} and n_F are generally dependent on the polarization waves and on their directions relatively to the principal axes. In some cases it is possible to modify the refractive indeces controlling of the temperature. These possibilities offer other degrees of freedom to satisfy the phase matching condition.

3.6.1 Phase-matching with birefringence

In a birefringence medium the electric field $\mathbf{E}$ of an electromagnetic wave is in relation with the electric flux density $\mathbf{D}$ with the following relation:

$$\mathbf{D} = \varepsilon \mathbf{E} \tag{3.57}$$

with ε that is a 3×3 matrix ($\varepsilon_{ij} \in \mathbb{R}$).
In this material each component of the electric flux density is a linear combination of the three componenets of the electric field.

$$D_i = \sum_j \varepsilon_{ij} E_j \tag{3.58}$$

where the indexes $i, j = 1, 2, 3$ refer to the x, y and z components,respectively. The element of the permittivity tensor depends on how the coordinate system is chosen in relation to the crystal structure. However, a special case exist where the coordinate system generates a diagonal matrix of the permittivity

tensor.

$$\begin{bmatrix} D_x \\ D_y \\ D_z \end{bmatrix} = \begin{bmatrix} \varepsilon_x & 0 & 0 \\ 0 & \varepsilon_y & 0 \\ 0 & 0 & \varepsilon_z \end{bmatrix} \begin{bmatrix} E_x \\ E_y \\ E_z \end{bmatrix} \tag{3.59}$$

This coordinate system defines the **principal axes** and the principal plane of the crystal. Each component of the field propagates along this particular direction with three different refractive indeces.

$$n_x = \sqrt{\frac{\varepsilon_x}{\varepsilon_0}}, \quad n_y = \sqrt{\frac{\varepsilon_y}{\varepsilon_0}}, \quad n_z = \sqrt{\frac{\varepsilon_z}{\varepsilon_0}} \tag{3.60}$$

where n_x, n_y, n_z are **principal refractive indeces**. The relation 3.58 can be inverted and written in the form $\varepsilon_0 \mathbf{E} = \eta \mathbf{D}$ where $\eta = \varepsilon_0 \varepsilon^{-1}$ is the **electric impermeability tensor**. With this new tensor we can introduce the quadratic representation of the electric impermeability tensor, the so called **index ellipsoid**.

$$\sum_{ij} = \eta_{ij} ij = 1, \quad i, j = x, y, z \tag{3.61}$$

Both tensors ε and η share the same principal axes. In the principal coordinate system, η is diagonal with principal values $1/n_x^2, 1/n_y^2, 1/n_z^2$ and from the equation 3.61 we can write:

$$\frac{x^2}{n_x^2} + \frac{y^2}{n_y^2} + \frac{z^2}{n_z^2} = 1 \tag{3.62}$$

The optical properties of the crystals are therefore completely described by the index ellipsoid. If the crystal is biaxial the three principal refractive indexes are different; if the crystal is uniaxial two principal refractive indexes are equal and the ellipsoid reduces to an ellipsoid of revolution and finally, for an isotropic medium the index ellipsoid becomes a sphere.
In uniaxial crystals electromagnetic wave propagating in any direction can travel with either the ordinary and extraordinary polarization. Light polarized perpendicular to the plane containing the propagation vector **k** and the optic axis is called the ordinary polarization. Such light experiences the ordinary refactive index n_0. Light polarized in the plane containing **k** and the optic axis is called the extraordinary polarization and experiences a refractive index $n_e(\theta)$ that depends on the angle θ between the optical axes and **k** according to the relation:

$$\frac{1}{n_e(\theta)^2} = \frac{\cos^2\theta}{n_o^2} + \frac{\sin^2\theta}{n_e^2} \tag{3.63}$$

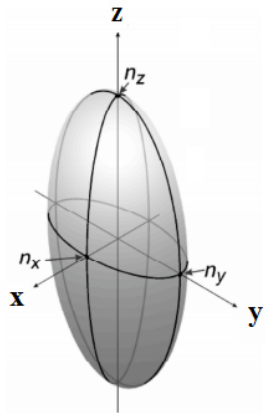

Figure 3.5: The index ellipsoid where coordinates (x, y, z) indicate the principal axes and (n_x, n_y, n_z) the principal refractive indeces

Note that $n_e(\theta)$ is equal to the principal value of the extraordinary refractive index n_e for $\theta = 90°$ degrees and is equal to the ordinary index n_0 for $\theta = 0$. Phase matching is achieved by adjusting the angle θ to obtain the value $n_e(\theta)$ for which the condition $\Delta k = 0$ is satisfied. There are two main types of phasematching, depending on the two possible orientations of the linear polarization vectors of the incident beams. Midwinter and Warner in 1965 define type-I phasematching to be the case in which the two lower incident frequencies have the same polarization, that is the polarization vectors are parallel, whereas the type-II phasematching to be the case where the two polarizations are orthogonal. The possibilities are summerized in the following Table. Consider the case of type I second harmonic generation in a negative

	Positive uniaxial $(n_e < n_0)$	Negative uniaxial $(n_e > n_0)$
Type-I	$n_3^o\omega_3 = n_1^e\omega_1 + n_2^e\omega_2$	$n_3^e\omega_3 = n_1^o\omega_1 + n_2^o\omega_2$
Type-II	$n_3^o\omega_3 = n_1^e\omega_1 + n_2^e\omega_2$	$n_3^e\omega_3 = n_1^o\omega_1 + n_2^o\omega_2$

Table 3.1: Phasematching methods for uniaxial cryastals

uniaxial crystal; since n_e is less than n_o, one chooses the fundamental frequency to propagate as an ordinary wave and the second harmonic frequency to propagate as an extraordinary wave, in order that the birefringence of the material can compensate for the dispersion. The phasematching condition

in this case is:

$$n_e(\omega_{SH}, \theta) = n_o(\omega_F), \tag{3.64}$$

$$\frac{\sin^2\theta}{n_e(\omega_{SH}^2} + \frac{\cos^2\theta}{n_o(\omega_{SH}^2} = \frac{1}{n_o(\omega_F)^2} \tag{3.65}$$

We can solve this equation for $\cos^2\theta$ and replace $\sin^2\theta = 1 - cos^2\theta$ to obtain:

$$\cos^2\theta = \frac{(1/n_0(\omega_F)^2) - (1/n_e(\omega_{SH})^2)}{(1/n_0(\omega_{SH})^2) - (1/n_e(\omega_{SH})^2)} \tag{3.66}$$

This equation shows how the crystal should be oriented in order to achieve the phasematching condition but, the solution does not exist necessarily for a physically realizzable orientation angle. For example, if for some materials the dispersion in the linear refractive index is too large or the birefringence is too small, the right-hand side of the last equation can have a magnitude larger than unity and consequently the equation will have no solution.

3.7 Quasi Phase Matching (QPM)

In the previous section we described birefringence of a nonlinear optical material as a method to achive the phase-matching condition of nonlinear optics. However there are situations in which these techniques are not suitable. For example, a particular material may possess no birefringence or insufficient birefringence to compensate the dispersion of the linear refractive index over the wavelength range of interest. Another situation under which birefringence phase matching cannot be used is when a particular application requires the use of d_{33} nonlinear coefficient that is much larger than the other nonlinear coefficients. When the interacting waves are polarized in the same direction the coefficient d_{33} can be used but birefringence cannot be used to compensate dispersion.
In QPM technique , the accumulation of phase mismatch is prevented through a spatial modulation of the sign of the nonlinear susceptibity. This condition is created by a periodically poled material which is a structure physically realized altering the orientation of one of the crystalline axis. In a ferroelectric crystal is usually inverted the c axis. This alteration has the consequence of inverting the sign of the nonlinear coefficient d_{eff}, thereby introducting an extra grating vector $\mathbf{K_Q}$ that is an artificial wave vector compensating the wave-vectior mismatch for SHG.
This technique was first proposed by Armstrong et al [18] in 1962. Matematically, we can consider the change of sign as being equivalent to a π phase shift ($e^{j\pi} = -1$). From an engineering point of view, in a SHG process, each

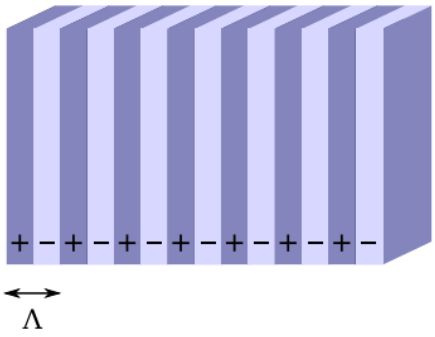

Figure 3.6: A schematic of periodically poled material with period Λ

layer length is chosen, in the way that the $-\pi$ phase shift obtained by the domain reversal is matching the phase shift obtained between the driving fundamental wave and the generated SH wave. The overall phase mismatch for each period is thus returned to zero, ensuring efficient second harmonic generation. Although the QPM interaction reduces the effective nonlinear coefficient by a factor $2/\pi$, the overall conversion efficiency can still be several times larger than with BPM (Best Phase Matching). The highest secon harmonic conversion efficiency is obtained for first-order QPM when the sign of the nonlinear coefficient is reversed every time the coherence length L_C occurs. When the sign of the nonlinear coefficient is reversed at a rate of m coherence lengths, the poling is named m-order QPM.
In a QPM structure, an artificially engineered spatial modulation of the nonlinear coefficient d is used to compensate for the phase-velocity mismatch between the interactive waves. A mathematical description of quasi phase matching can be formulated as follows. We let $d(z)$ denote the spatial dependance of the nonlinear coupling coefficient. It is useful to describe the spatial variation in term of a Fourier expansion:

$$d(z) = d_{il} \sum_{m=-\infty}^{\infty} G_m exp(jk_{mQ}z) \tag{3.67}$$

where d_{il} is the material nonlinear coefficent, G_m is the Fourier coefficient of the mth harmonic, and k_{mQ} is the magnitude of the grating vector associated with the mth Fourier component of $d(z)$ that is defined as:

$$k_{mQ} = \frac{2\pi m}{\Lambda}, \qquad m = 1, 2, 3, ... \tag{3.68}$$

where Λ is the period of modulated structure. When the sign of the nonlinear coefficient is periodically modulated, the mth Fourier coefficient is equal to:

$$G_m = \frac{2}{m\pi}\sin(m\pi D) \tag{3.69}$$

where $D = l/\Lambda$ is the duty cicle, which is the ratio of the reversed domain length l and the structure period Λ.
The effective nonlinear coefficient depends on the mth Fourier coefficient from the following relation:

$$d_{eff} = d_{il}G_m, \qquad d_{eff} = \frac{2d_{il}}{m\pi}\sin(m\pi D) \tag{3.70}$$

In Figure 3.7, we show the dependence of the effective nonlinear cefficient on the duty cicle for $m = 1, 2, 3$ and considering $d_{ij} = 1$. For the first-order QPM, the highest SH coversion is obtained at a duty cicle of $D = 0.5$ whereas for second-order QPM, it is found at $D = 0.25$ and for the third-order QPM at $D = 0.167$.

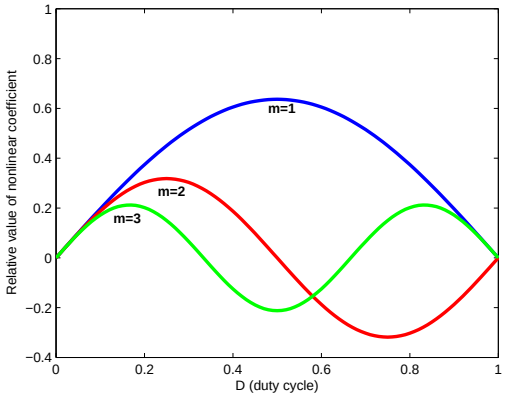

Figure 3.7: The variation of the d_{eff} coefficient as a function of the duty cicle for $1^{st}, 2^{nd}, 3^{rd}$ order

This relation between the effective nonlinear coefficient and order of QPM has an effect on conversion efficiecy of second harmonic. In Figure 3.8, we show how the 2^{nd} and 3^{rd} has, respectively, only 1/4 and 1/9 of efficiency compared to the 1^{st} order structure. We show the relation in the ideal case without duty error. In a real case, the maximum value of conversion efficency drops down if the duty cicle value is not optimum.

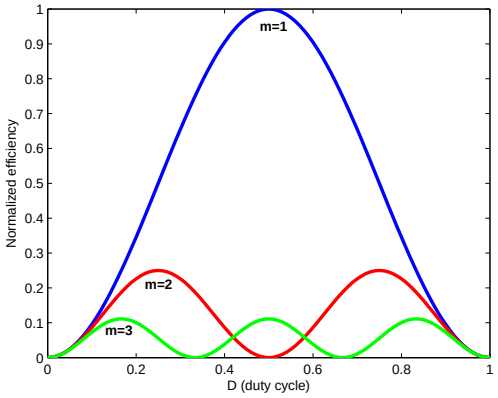

Figure 3.8: The relation between duty cicle and normalized efficiency at $1^{st}, 2^{nd}, 3^{rd}$ order.

3.7.1 SHG in presence of QPM

Now, consider a second harmonic generation in a non linear crystal with quasi phase matching. In this thesis we used a PPKTP to realize QPM and in this case the efficient non linear coefficient is.

$$d_{eff} = \frac{2d_{il}}{\pi m}\sin(\pi m D) \tag{3.71}$$

If we consider the case in which all wave vectors are collinear with the grating vector along the z-axis, the vector mismatch for QPM-SHG is:

$$\Delta k_Q = k_{SH} - 2k_F - k_{mQ} \tag{3.72}$$

Applying the same approximation that we used in equation 3.46, we can write the variation of SH in QPM as follows:

$$\frac{\partial E_{SH}(z,\omega)}{\partial z} = \frac{j\omega d_{eff}}{n_{SH}c_0}E_F(z,\omega)E_F(z,\omega)e^{j(\Delta k_Q z)} \tag{3.73}$$

The amplitude of SH outcome of the nonlinear crystal with length L is:

$$E_{SH}^{QPM}(L) = \frac{\omega d_{il}E_F^2}{n_{SH}c_0}\frac{2}{\pi m}\sin(\pi m D)\int_0^L je^{j\Delta k_Q z}dz \tag{3.74}$$

The intensity of SH in presence of QPM is equal to:

$$I_{SH}^{QPM} = \frac{2L^2\omega^2 d_{il}^2 I_F^2}{\epsilon_0 c_o^3 n_{SH}n_F^2}\frac{4}{m^2\pi^2}\sin(\pi m D)sinc^2\left(\frac{\Delta k_Q L}{2}\right) \tag{3.75}$$

we can rewrite it in the following way:

$$I_{SH}^{QPM} = I_{max}\frac{4}{m^2\pi^2}\sin(\pi m D)sinc^2\left(\frac{\Delta k_Q L}{2}\right) \tag{3.76}$$

When the SH and fundamental waves are quasi phasematched, than $\Delta k_Q = 0$ and the corresponding grating period which satisfies the QPM condition is:

$$\Lambda = \frac{2m\pi}{k_{SH} - 2k_F} = \frac{m\lambda_F}{2(n_{SH} - n_F)}, \qquad with \quad m = 1, 2, 3, ... \tag{3.77}$$

If we realize a first-order QPM, with $m = 1$, in the best condition of duty cicle ($D = 50\%$) and under the condition of quasi-phasematching, the intensity of SH is:

$$I_{SH}^{QPM} = \frac{4}{\pi^2} I_{max} \tag{3.78}$$

3.8 Spontaneous Parametric Down Conversion (SPDC)

Spontaneous parametric down conversion is a quantum mechanical phenomenon where the input field, usually called *the pump*, with frequency ω_p interacts with a nonlinear crystal creating two output fields, usually called *signal* and *idler* with frequencies ω_s and ω_i respectively. The SPDC optical process must occur under the condition of energy conservation $\omega_P = \omega_s + \omega_i$ and moment conservation $k_p = k_s + k_i$. We can view the process from a photon-optics perspective as a process of three-photons interaction in which one photon with frequency ω_p entering in the nonlinear crystal is converted into two photons with frequencies ω_s and ω_i.

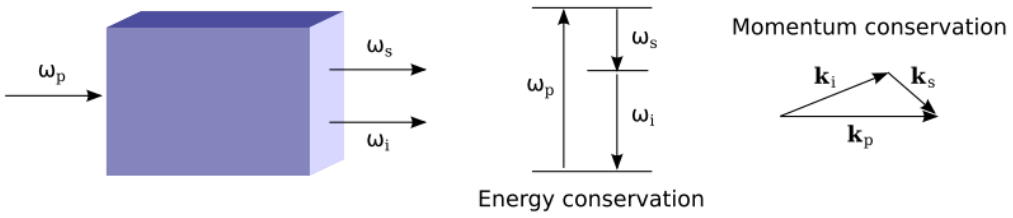

Figure 3.9: Schematic rapresentation of SPDC optical process with requirements of energy and momentum conservation

We can distinguish two types of SPDC, type-I and type-II according to the polarizations of the pump, idler and signal.

- **Type-I**

In SPDC type-I the pump photon has an orthogonal polarization (either ordinary or extraordinary) with respect to idler and signal photons which are equally polarized. Due to the fact that the two photons have the same polarization they will have the same refractive index and thus lie on the same cone. The degenerate case is illustate in Figure 3.10a, where the wavelength of both idler and signal are double respect to the pump wavelength. If the input angle of the pump changes with respect to the crystal, the emission cone changes its size. One can also think of a setting where signal and idler photons are emitted in the pump direction, this case is called *collinear down conversion*. Otherwise, if the signal and idler are emitted in different directions with rispect to the pump, this case is called *non collinear down conversion*.

- **Type-II**

In SPDC type-II the idler and signal have orthogonal polarizations (either ordinary or extraordinary). Due to the fact that the refractive indices of the two created photons are different, the cones are not coaxial. Again the size of the cones depends on the angle between the pump beam and the optical axis of the crystal. Here the collinear case is when the two emission cones are tangential. Thus idler and signal can be emitted in pump beam direction.

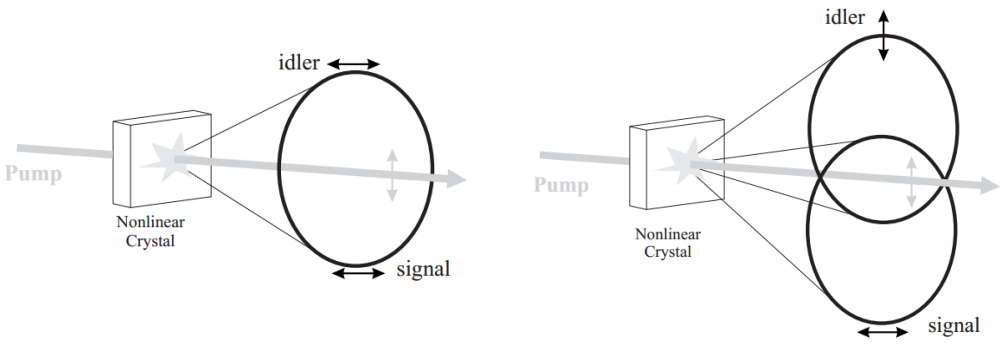

(a) SPDC Type-I (b) SPDC Type-II

Figure 3.10

Chapter 4

KTP and PPKTP crystals

In this chapter we present the characteristics of nonlinear optical material (KTP) and periodically poled KTP material.
Potassium Titanyl Phosphate (KTP) has been shown to have superior properties for several nonlinear-optical applications. It is characterized by high nonlinear-optical d coefficients, high optical damage threshold, wide acceptance angles and thermally stable phase-matching properties which make it useful for this purpose. Periodically poled crystals, in particular ferroelectrics materials, are suitable for the practical production of QPM devices for frequency conversion. Especially, this has been important to generate of compact and efficient blue-green sources as well as for UV light generation.
However,it is a very challenging task to fabricate high-quality PP structures with fine-pitch domain gratings ($3 - 10 \ \mu m$ periods) in large aperture samples ($> 0.5 \ mm$) needed for medium and for high-power applications.
In the following sections deal with the structure and crystal growth, optical properties, main fabrication techniques and possible damages in KTP induced by laser beam.

4.1 Structure and crystal growth

The **Potassium Titanyl Phosphate** material ($KTiOPO_4$ *or* KTP) belongs to the family of compounds with the formula unit $\boldsymbol{M}TiO\boldsymbol{X}O_4$, where M can be K, Rb, Tl, NH_4, and X can be P *or* As.
The KTP structure was determined for the first time in 1974 by Tordjman *et. al* [19]. It is an orthorhombic crystal and belongs to the acentric point group mm (space grup $Pna2$).
When we describe a crystal structure, the main parameter is the lattice constant, that is a costant distance between crystal cells in a crystal lattice. In

general the lattices have three constants referred to as a, b and c.For KTP the lattice costants are $a = 12.814\ \mathring{A},\ b = 6.404\ \mathring{A},\ and\ c = 10.616\ \mathring{A}$ and each unit cell contains eight formula units [20].
Figure 1 shows two unit crystal cells along the projection plane (a-c) and (a-b). The structure is characterized by chains of TiO_6 octahedra, which are linked at two corners, and the chains are separated by PO_4 tetrahedra.

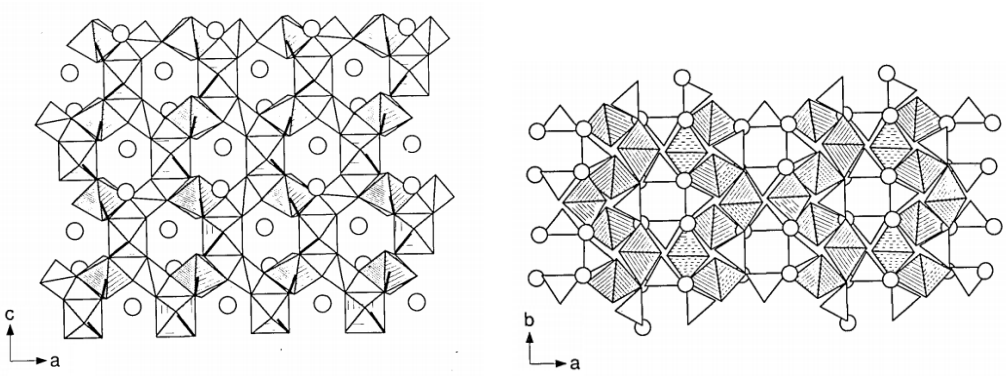

(a) a-c projection (b) a-b projection

Figure 4.1: KTP crystal structure

There are two chains per unit cell, and the chain direction alternates between [011] and [011], alternating long and short $Ti-O$ bonds occur along these chains (in figure the short $Ti-O$ bonds are shown as bold lines). This anisotropic structure in which there are long and short $Ti-O$ bonds is the major contributor to KTP large nonlinear optical coefficients.
KTP melts at $T \simeq 1150\ ^oC$ and the normal melt-growth techniques cannot be used to grow this material. Two common methods are used to grow KPT crystal: **Hydrothermal method** and **Flux-grown method**.

1. **Hydrothermal method:** The hydrothermal process consists in sealing nutrient and seed crystal in a gold or platinum tube inserted into a high-pressure and high-temperature autoclave. The crystal growth occurs at constant pressure ($\simeq 1.724 \times 10^8$) and temperature ($\simeq 350 - 600\ ^oC$) with a fixed gradient for approximately 6 weeks [20]. High quality, in terms of uniformity and low conductivity, can be obtained with this technique. However, it is difficult to grow a large crystal, which is limited to approximately $20mm \times 20mm \times 60mm$.

2. **Flux grown method:** The flux technique is essentially a high-temperature solution growth process in which the KTP crystallized out of a molten KTP/flux composition when cooled. Depending on the specific flux

used, crystal growth can occur from approximately 700 ^oC to approximately 1000 ^oC, and common fluxses vary according to different concentration of potassium phosphates. A significant advantage of using the flux process is that it operates at atmospheric pressures and hence does not require sophisticated pressure equipment. However, uniform temperatures and high levels of temperature control are required.

Nonlinear and electro-optical properties of KTP crystals grown by the flux and hydrothermal techniques are similar. Nevertheless differences have been observed in some of the dielectric properties and in the high-power optical damage characteristics. In particular KTP crystals grown with the hydrothermal technique have higher power optical damage than crystals grown with flux-grown technique.

4.2 Periodic poling technique for SHG

The idea of phase matching for SHG was first mentioned in [18]. The authors considered the possibility of periodic polarization reversal for quasi-phase matching via a 180° shift of the relative phase to enhance the conversion efficiency. The most common method to achieve domain reversal in ferroelectrics is by electric-field poling. Materials suitable for SHG must be non-centrosymmetric, and consequently there is the possibility of reversing their spontaneous polarization with external help, either during growth or subsequently. KTP is of current interest because it has good electro-optic and nonlinear properties as well as a high optical damage threshold.

4.2.1 Electric poling

Electring poling consists in applying at the material an electrostatic field, which can induce molecules to orientate along the field direction. This procedure involves several stages (Figure 4.2).
At the beginning, molecules have a random orientation inside the matrix. The polymer is heated through the Curie point and after an electric field is applied for a short period: in this way molecules can orientate their dipoles along the field direction. After, the polymer is cooled down in order to give a permament orientation to the crystal. One unfortunate problem is the limited lifetime of the poled structure. It has been noticed that organic molecules tend to lose their arrangement and thus their non-centrosymmetry. This limits the number of applications and so different techniques for poling polymers have been attempted.
The most used technique is corona poling [21],in which the crystal as a thin

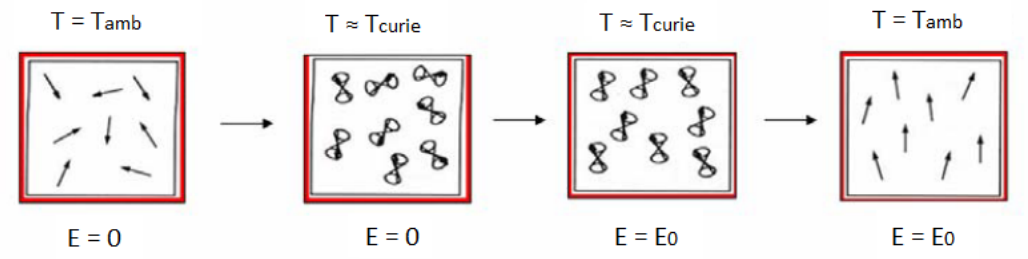

Figure 4.2: Schematic representation of the electric poling process

film is deposited on a substrate in contact with an electrode connected to the ground. On the other electrode (usually a thin golden or platinum wire) a high tension is applied ($5 - 10$ KV). Gas molecules and atoms surrounding the electrode (N, Ar, He) are ionized and along the filed's lines they are deposited on the film (Figure 4.4). Depending in the polarity of the electrode, both positive and negative ions can be emitted in the ionization region.

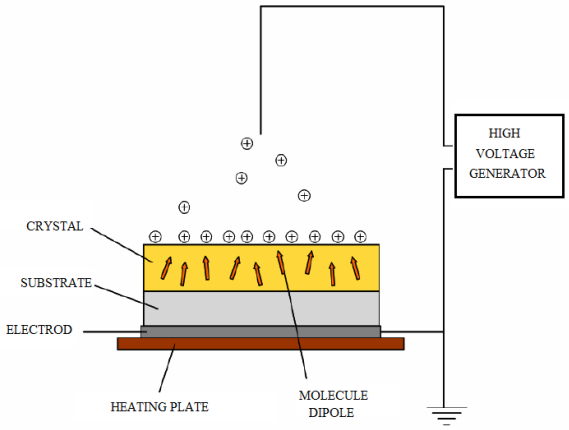

Figure 4.3: Schematic representation of Corona poling process.

The insulating nature of the crystal prevents the closing of the circuit and promotes the accumulation of high charges density on the surface. This expedient allows to reach very high local field values, to the order of several MV/cm. As the poling proceeds the dipoles orient in the crystal, so that the permanent dipole moment aligns with the field direction.

4.2.2 Heat treatments in KTP poling

Heating towards the Curie temperature can mimic the simple classic conditions for poling but if the region is to be localized, as in periodic poling, than

bulk heating may be undesiderable. A recent variation was to apply a steady DC electric field to crystals of KTP and pulse the local temperature by using a laser beam of 5 ns duration and some $80 - 100$ mJ cm^{-2} [22]. The concept is to move from the stable regime defined below the boundary line (of Figure 4.4a) to a point above it. While a high-voltage pulse moves between conditions in the ordinate direction, the heat pulse moves along the abscissa in. in this first example domain inversion was demonstrated when the sample temperature was 400 $°C$ and the steady field was just 750 V cm^{-1} (Figure 4.4b).

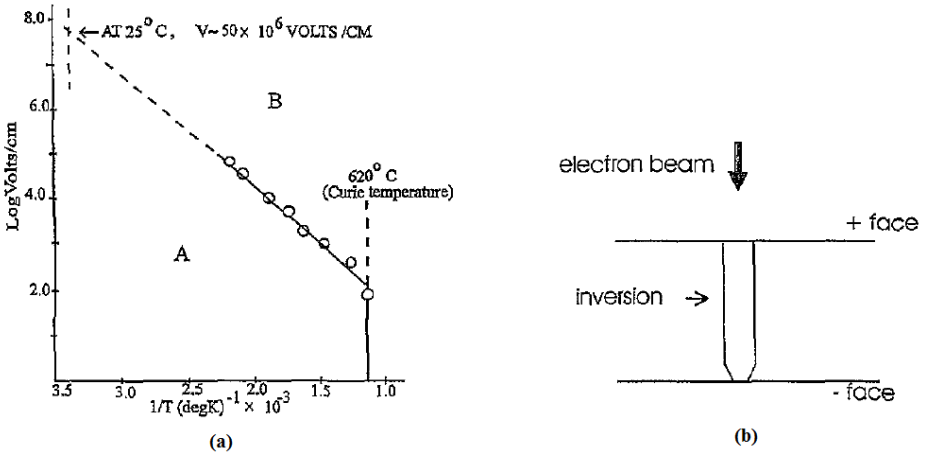

Figure 4.4: (a) Data for effective polarization reversal in KTP as a function of temperature and DC field. Note that region A is stable against inversion whereas excursion into region B allow re-poling. (b) An example of the shape of the inversion region in KTP which resulted from electron beam bombardment on the + surface.

4.3 Crystal properties

4.3.1 Ionic conductivity

The ionic conductivity originates from the ion transport in the crystal lattice. The open nature of the framework, built up by the TiO_6 octahedra and the PO_4 tetrahedra, allows for cations to diffuse easily along the polar axis. Thereby, KTP gets a relative large and highly anisotropic ionic conductivity. The ionic conductivity of KTP varies depending on the crystal growth process. Typically, the room-temperature ionic conductivity of flux-grown

KTP is $10-6$ S/cm. The high conductivity of flux grown KTP is primarily attributed to the non stoichiometry of the crystals, where the K^+-vacancies are built into the structure, which are than available for ionic transport with an applied electric field. Hydrothermally grown KTP, on the other hand, has a higher degree of stoichiometry and is, hence, much less conductive than the flux-grown material. However, as mentioned earlier, this material is much more difficult to grow. To obtain a flux-grown material with low conductivity, the doping technique was introduced. It has been reported that the ionic conductivity of KTP can be reduced by 1.5 to 3 orders of magnitude by introduction of dopants in the growth melt. However, some of the dopants make it difficult to do the periodic poling as they occupy crystal lattice positions that inhibits or hampers the domain reversal. KTP doped with Rb is an interesting candidate for periodic poling as we know that KTP can be poled with good results and the Rb^+-ion reduces the conductivity.

4.3.2 Ferroelectricity

Ferroelectric crystals are materials with a spontaneous polarization, as an inherent electric dipole moment per unit volume, that can be switched between two or more equilibrium states by an applied electric field. The electric field required to switch the direction of the spontaneous polarization is called coercive field. A ferroelectric domain is defined as a region of the ferroelectric crystal, with a uniform spontaneous polarization. In KTP, the domains have two states, the so called 180 degree domains oriented either in the c^+ or the c^- direction. The interface between two domains is called the domain wall. In ferroelectrics, the domains are stable below the Curie point, Tc.

4.3.3 Piezoelectricity

Piezoelectricity is a phenomenon where positive and negative charges are generated on a crystals surface when mechanical stress is imposed. The piezoelectric effect is a reversible electromechanical interaction. The inverse piezoelectricity is the generation of a mechanical stress by an applied electric field. The responses are linear with the applied electric field. All ferroelectric crystals are also piezoelectric.

4.3.4 Optical properties

KTP crystals have been widely used for SH generation of the near-IR laser beam and also for near-IR optical parametric oscillators (OPO). In the previous section we have shown the development of periodically poled KTP that

provides a wider use of the material thanks to its fully trasparency region from the UV, over the visible region to the near-IR spectrum. In general, $MTiOPO_4$ is trasparent over a broad wavelength range from 400 nm to 4000 nm [23]. An important feature, is the presence of a strong absorption line at about 2.8 μm. It is caused by OH^- groups trapped in the crystal during growth.
The d-matrix of the crystal has only 5 non-zero nonlinear coefficients:

$$d = \begin{bmatrix} 0 & 0 & 0 & 0 & 0 & d_{15} \\ 0 & 0 & 0 & d_{24} & 0 & 0 \\ d_{31} & d_{32} & d_{33} & 0 & 0 & 0 \end{bmatrix} \tag{4.1}$$

The values of second-order nonlinear optical coefficients play a key role in determination of the performance of optical processes but, significant discrepancies have been noted among them because of the different methods used by various investigators. In paper [24] is reported a more accurate and consistent absolute scale of second-order nonlinear-optical coefficients. In Table 4.1, we reported second-order nonlinear-optical coefficients for KTP crystal.

wavelength	$d_{15}(pm/V)$	$d_{24}(pm/V)$	$d_{31}(pm/V)$	$d_{32}(pm/V)$	$d_{33}(pm/V)$
$\lambda = 1313$ nm	2.6	1.4	no det.	no det.	11.1
$\lambda = 1064$ nm	3.7	1.9	3.7	2.2	14.6
$\lambda = 852$ nm	3.9	1.9	no det.	no det.	16.6

Table 4.1: Absolute magnitudes of second order nonlinear optical coefficient [24]

The absolute magnitude of the nonlinear optical coefficients was obtained by measuring of the second-harmonic power P_SH, the fundamental power P_F, and the fundamental beam radii ω_x and ω_y. The values of d_{31} and d_{32} at 1313 nm and 852 nm were not determined because the SH power was too low to give reproducible data [24].
To be able to generate a specific wavelength by the QPM devices, accurate knowledge of the refractive indices is needed. They are normally described by the **Sellmeier equation** and hence used for calculating the grating period. The Sellmeier equation is an empirical relation between the refractive index n and the light wavelength λ in the form of a series of single-dipole oscillator. In a medium with multiple resonances, the susceptibility is approximately given by a sum of terms, each in the following form:

$$\chi(\nu) \approx \chi_o \frac{\nu_0^2}{\nu_o^2 - \nu^2} \tag{4.2}$$

for frequencies far from any resonance.
Using the relation between the refractive index and the real susceptibility $n^2 = 1 + \chi$, the dependence of n on frequency and wavelength assumes a form known as the Sellmeier equation:

$$n^2 \approx 1 + \sum_i \chi o_i \frac{\nu_i^2}{\nu_i^2 - \nu^2} = 1 + \sum_i \chi o_i \frac{\nu_i^2}{\lambda_i^2 - \lambda^2} \tag{4.3}$$

The coefficients of the Sellmeier equation are obtained through experimental data, using a least-squares fitting algorithm. At wavelengths for which $\lambda \ll \lambda_i$ the ith term becomes approximately proportional to λ^2, and for $\lambda \gg \lambda_i$, it becomes approximately costant. It is possible to find the Sellmeier equation in the following general form given as:

$$n(\lambda) = 1 + \sum_i \frac{B_i \lambda^2}{\lambda^2 - C_i} \tag{4.4}$$

In several studies about optical properties of PPKTP crystal, the Sellmeier equation is the following:

$$n_e^2 = A + \frac{B}{1 - C/\lambda^2} + \frac{D}{1 - E/\lambda^2} - F\lambda^2 \tag{4.5}$$

where the corresponding costants are [25]:

A	B	C (μm^2)	D	E (μm^2)	F (μm^{-2})
2.12725	1.18431	5.14852×10^{-2}	0.6603	100.00507	9.68956×10^{-3}

Table 4.2: Sellmeier constants for PPKTP

The refractive index is a parameter that depends also on the temperature. The temperature tuning characteristics of the nonlinear interaction is very important. First of all, the phase matching wavelenght can be adjusted by changing the crystal temperature in order to match it to a light source with a fixed wavelength. Moreover, the temperature tuning characteristics for SHG can also provide information about the uniformity of the QPM structure, as a quality measured for the poling process. In the presence of three-wave mixing with waves signal, idler and pump; we can write the quasi phase matching condition as [25]:

$$\frac{n_e(\lambda_p, T)}{\lambda_p} - \frac{n_e(\lambda_s, T)}{\lambda_s} - \frac{n_e(\lambda_i, T)}{\lambda_i} - \frac{1}{\Lambda(T)} = 0 \tag{4.6}$$

and

$$\Lambda(T) = \Lambda_0 \left[1 + \alpha(T - 25°C) + \beta(T - 25°C)^2\right] \tag{4.7}$$

where $\Lambda(T)$ is the actual grating period of the crystal taking into account the thermal expansion of the material. The temperature coefficients α and β for PPKTP crystal are equal to:

$\alpha \ \ coefficient(°K^{-1})$	$\beta \ \ coefficient(°K^{-1})$
6.7×10^{-6}	11×10^{-9}

Table 4.3: Temperature coefficient for PPKTP [25]

4.4 Laser-induced damage in PPKTP

Laser-induced damage in crystals is a detrimental effect for nonlinear frequency converters. Particularly, photorefractive effect and photochromic effect like green-induced infrared absorption (GRIIRA), will limit the performance of high-power operating SHG devices in the UV and the visible spectrum. Different materials have different damage thresholds, which are complex functions of wavelength, peak intensity, average power, temperature, exposure duration and processing history of the crystal. Some of these negative effects can be mitigated at elevate temperatures but the lifetime of these materials may still be limited.
Green-induced infrared absorption is an increase of the infrared absorption in the presence of green light which causes a damage of the mechanism. In our research work a red light has been used, so we will not focalize on this particular damage source.

4.4.1 Photorefractive effect

The photorefractive effect is an optically induced change in refractive index. It is an unwelcome effect as preserving good beam quality is vital, and the photorefractive effect can cause beam distortion and scattering, leading to deterioration in optical performance. To minimize this effect both experimental and theoretical solutions have been proposed, such as:

1. operating the sample at elevated temperature;

2. doping the crystal with magnesium oxide;

3. make the crystal more stechiometric.

Furthermore, several studies have shown that the periodic poling can reduce the photorefractive effect in the crystal. This might be due to a cancellation effect in the adjacent domains with opposite direction of the spontaneous polarizations. On the other hand, KTP and its isomorphs, have a low susceptibility to photorefractive damage benefiting mainly from the high ionic conductivity, which will screen any generated bulk field.
The photorefractive effect is quite different from most of the other nonlinear-optical effects because it cannot be described by a nonlinear susceptibility χ^n for any value of n. The reason for this behavior is that, under a wide range of conditions, the change in refractive index in steady state is independent of the intensity of the light that induces the change.
The origin of photorefractive effect is illustrated schematically in Figure 4.5. We imagine that a photorefractive crystal is illuminated by two intersecting beams of light of the same frequency. These beams interfere to produce the spatially modulated intensity distribution I(x) shown in the upper graph.

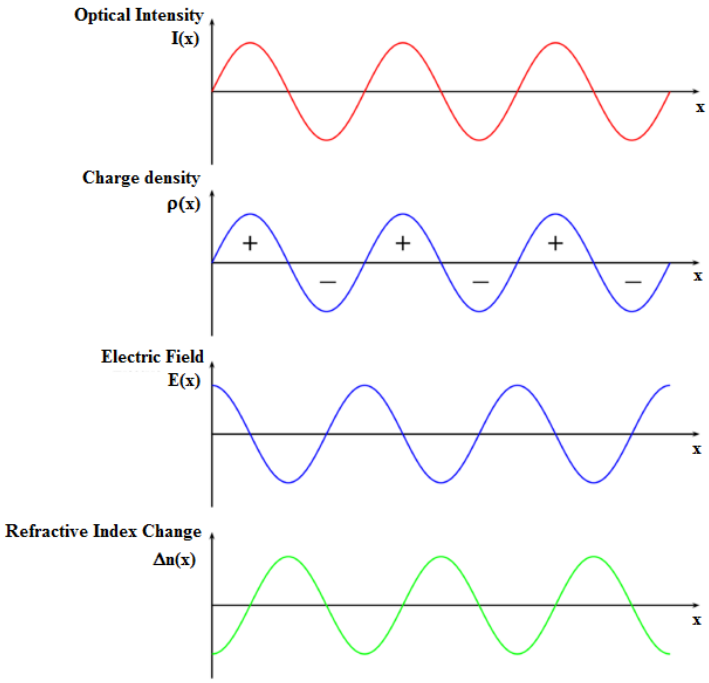

Figure 4.5: The resulting distributions of intensity $I(x)$, charge density $\rho(x)$, induced static field amplitude $E(x)$ and induced refractive index change $\Delta n(x)$

The incident light then induces a migration of charge along the optical axis,

in which Fe^{2+} and Fe^{3+} ion impurities can be photoexcited to produce electrons and holes respectively.

$$\begin{aligned} Fe^{2+} + h\nu &\Rightarrow Fe^{3+} + e^{-} \\ Fe^{3+} + h\nu &\Rightarrow Fe^{2+} + h^{+} \end{aligned} \tag{4.8}$$

Free charge carriers, which we assume to be electrons, are generated at a rate that is proportional to the local value of the optical intensity. These carriers can diffuse through the crystal or can drift in response to a static electric field. Both processes are observed experimentally. In drawing the figure we have assumed that diffusion is the dominant process, in which case the electron density is smallest in the region of maximum optical intensity, because electrons have preferentially diffuse away from these regions. The spatially varying charge distribution $\rho(x)$ gives rise to a spatially varying electric field distribution, whose form is shown in the third graph. Note that the maxima of the field $E(x)$ are shifted by 90 degrees with respect to those of the charge density distribution $\rho(x)$. the reason for this behavior is that the Maxwell equation $\nabla \cdot D = \rho$ when applied to the present situation implies that $dE/dx = \rho/\epsilon$, and the spatial derivative that appears in this equation leads to a 90-degree phase shift between $E(x)$ and $\rho(x)$. The last graph in the figure shows the refractive index variation $\Delta n(x)$ that is produced through the linear electrooptic effect (Pockels effect) by the field $E(x)$.

4.4.2 Photorefractive equations of Kukhtarev

In this section we see how to describe the photorefractive effect by means of a model Figure 4.6 due to Kukhtarev and co-workers. This model presupposes that the photorefractive effect is due solely to one type of charge carrier, which for definiteness we assume to be the electron. As illustrated in Figure 4.6.a, we assume that the crystal contains N_A acceptors and N_D^0 donors per unite volume, with $N_A \ll N_D^0$.

We assume that the acceptor levels are completely filled with electrons that have fallen from the donor levels and that these filled acceptor levels cannot be ionized by thermal or optical effect. Thus, at temperature $T = 0$ and in the absence of an optical field, each unit volume of the crystal contains N_A ionized donors, N_A electrons bound to acceptor impurities, and $N_D^0 - N_A$ neutral donor levels that can participate to the photorefractive effect. We further assume that electrons can be excited thermally or optically from the donor levels into the conduction band, as illustrated in part (b) of the

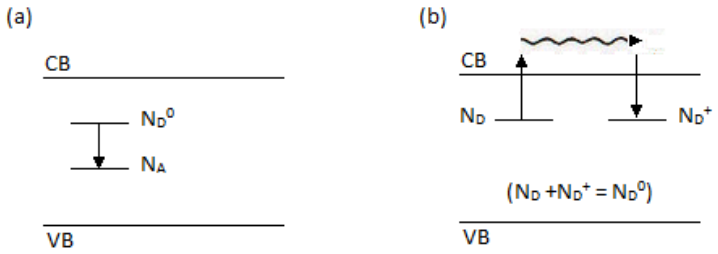

Figure 4.6: Energy level and populations of the model of the photorefractive effect due to Kukhtarev

figure. We let ne, N_D^+, and N_D denote the number densities of conduction band electrons, ionized donors, and unionized donors, respectively. Note that $N_D + N_D^+$ must equal N_D^0, but that N_D^+ is not necessarily equal to n_e, because some donors lose their electrons to the acceptors and because electrons can migrate within the crystal, leading to regions that are not electrically neutral. We next assume that the variation in level populations can be described by the rate equations.

$$\frac{\partial N_D^+}{\partial t} = (sI + \beta)(N_D^0 - N_D^+) - \gamma n_e N_D^+ \tag{4.9}$$

$$\frac{\partial n_e}{\partial t} = \frac{\partial N_D^+}{\partial t} + \frac{1}{e}(\nabla \cdot \mathbf{j}) \tag{4.10}$$

where s is a constant proportional to the photoionizatin cross section of a donor, β is the thermal generation rate, γ is the recombination coefficient $-e$ is the charge of the electron, and j is the electrical current density. Equation 4.9 states thet the ionized donor concentration can increase by thermal ionization of photoionization of unionized donors and can decrease by recombination. Equation 4.10 states that the mobile electron concentration can increase in any small region either because of the ionization of donor atoms or because of the flow of electrons into the local region. The flow of current is described by the equation:

$$\mathbf{j} = n_e e\mu \mathbf{E} + eD\nabla n_e + \mathbf{j}_{ph} \tag{4.11}$$

where μ is the electron mobility, D is the diffusion constant and $\mathbf{j_p h}$ is the photovoltaic contribution to the current.
The field E appearing in the equation above is the static electric field appearing within the crystal due to an applied voltage or to any charge separation within the crystal. It must satisfy the Maxwell equation:

$$\epsilon_{dc} \nabla \cdot \mathbf{E} = -e(n_e + N_A - N_D^+) \tag{4.12}$$

where $\varepsilon - dc$ Is the static dielectric constant of the crystal. The modification of the optical properties is described by assuming that the optical-frequency dielectric constant is changed by an amount:

$$\Delta\epsilon = -\epsilon^2 r_{eff}|E| \tag{4.13}$$

For simplicity, here we are treating the dielectric properties in the scalar approximation. The optical field Eopt is assumed to obey the wave equation

$$\nabla^2 \widetilde{E}_{opt} + \frac{1}{c^2}\frac{\partial^2}{\partial t^2}(\epsilon + \Delta\epsilon)\widetilde{E}_{opt} = 0 \tag{4.14}$$

Equations 4.9 through 4.14 constitute the photorefractive equations of Kukhtarev *et. al.* [17] they have been solved in a variety of special cases and have been found to provide an adequate description of most photorefractive phenomena.

Chapter 5

Experimental Setup

In this chapter we will present our experimental setup and we will explain the principle of working of each optical components.
We tested the generation of second harmonic from the 1 GHz repetition rate TACCOR 8 laser and its use for the generation of polarized photon pairs. We divided the experiment in two parts. In the first part we tested the Second harmonic generation (SHG) at 405 nm only.
We tested three different non-linear materials for SHG:

1. Periodically Poled KTP - **PPKTP** crystal;

2. Bismuth Borate BiB_3O_6 - **BiBO** crystal;

3. Beta Barium Borate **BBO** crystal.

We mainly experimented the second harmonic generation by PPKTP crystal but we also tested BBO and BiBO crystal to obtain a comparison on SHG. In this part it was important to study the characteristic of the gaussian laser beam and its trasformation in a setup with a system of lens, in order to find the best focusing condition into the nonlinear crystal. Finally, we built a Michelson interferometer to characterize the coherence time of the SH beam. In the second part we tested the complete experimental setup of polarization Entangled photon-pairs generation at 810 nm wavelenghts by a 2 mm BBO with the second harmonic beam. Even for the second part of the experiment it is important to work in the best focussing condition, with the gaussian beam well collimated along the path and with the optical system well aligned. These aspects are of paramount important to carry out an experiment of photon-pairs generation.

5.1 The Taccor8 laser source

The Taccor is a unique turn-key femtosecond laser with a repetition rate as high as 1 GHz that delivers up to 1.6 W of average power with pulses that can be as short as 15 fs. The laser is a mode-locking and it uses as nonlinear medium a sapphire crystal doped with titanium (Ti:Sapphire) with a very short resonant cavity. The Ti:Sapphire oscillator is pumped by a field of replaceable laser pump diode.

5.1.1 Mode locking

A multi-mode laser is said to be mode-locked if its modes have a well-defined and fixed phase relationship. In a laser every mode can oscillate on many longitudinal modes, with frequencies that are equally separated at $\nu_F = c/2d$. Although these modes normally oscillate independently, external means can be used to couple them, and lock their phases together. If the phases are locked in such way that there is a constructive interference between the modes at an instant and a destructive interference at other times, the output will appear as a pulse. We consider a simple analysis of mode-locking in which all oscillating modes are approximated by a uniform wave propagating in the z direction that has equal amplitude. Under these assumptions, the total electric field that is formed by $2n+1$ equally spaced modes is given by:

$$E(z,t) = \sum_{q=-n}^{n} Eexp\left[j2\pi\nu_q\left(t-\frac{z}{c}\right)\right] \tag{5.1}$$

where $\nu_q = \nu_0 + q\nu_F$ is the frequency of mode q (with $q = 0, \pm1, \pm2, ...$) end E_q is the complex envelope. We can rewrite the previous expression as follows:

$$E(z,t) = exp\left[j2\pi\nu_0\left(t-\frac{z}{c}\right)\right]\underbrace{\sum_{q} Eexp\left[j2\pi q\nu_q\left(t-\frac{z}{c}\right)\right]}_{E\left(t-\frac{z}{c}\right)}$$

$$E(z,t) = E\left(t-\frac{z}{c}\right)exp\left[j2\pi\nu_0\left(t-\frac{z}{c}\right)\right] \tag{5.2}$$

where the complex envelop $E(t)$ is a periodic function of the period $T_F = 1/\nu_F = 2d/c$ and $E(t-z/c)$ is a periodic function of the period $cT_F = 2d$.

$$E(t) = E\sum_{q=-n}^{n} exp\left(\frac{jq2\pi t}{T_F}\right) \tag{5.3}$$

So we have got an amplitude-modulated wave oscillating at the central mode frequency ν_0 and we can see that the expression for $E(t)$ contains a geometrical progression. From this we can convert it to another form and get the optical intensity as follows:

$$I(t,z) = |I(t-c/z)|^2 = |E|^2 \frac{\sin^2\left[(2n+1)(t-z/c)/T_F\right]}{\sin^2\left[\pi(t-z/c)/T_F\right]} \tag{5.4}$$

This function is periodic one, with strong peaks, the pulses, equally spaced by very weak subsidiary peaks. We can show several other important properties of this function. The pulse duration decreases, and its amplitude increases, as the number of modes increases. The number of modes $(2n+1)$ is proportional to the atomic linewidth $\Delta\nu$ and if $2n+1 \approx \Delta\nu/\nu_F$, the pulse duration τ_{pulse} is therefore inversally proportional to the atomic linewidth $\Delta\nu$.
If we consider the repetition rate at 1 GHz we find that the lenght of the resonant cavity of The TACCOR source is:

$$d = \frac{T_F * c}{2} = 15 \ \ cm \tag{5.5}$$

The Taccor laser source implements a mechanism of **self mode locking** that relies on the optical Kerr effect inside of the active medium. The optical Kerr effect is a third-order, non-linear effect which results in a change induced in the refractive index of a material by appling high-intensity electric fields. The behaviour of the refractive index under the Kerr effect is intensity dependent and can be described by:

$$n(I) = n_0 - \frac{1}{2}\mathbf{s}n^3 I \tag{5.6}$$

where n_0 is the refractive index, $\mathbf{s}$ is the **Kerr coefficient**, and I is the instantaneous beam intensity. For solid-state materials, the typical values of $\mathbf{s}$ are 10^{-18} to 10^{-14} m^2/W [15]. So it becomes considerable only for the high-intensity light pulses. In a pulsed laser the refractive index n of an active medium is proportional to the time and space dependent intensity $I(t,z)$ of the pulsed radiation. Therefore, the expression 5.6 can be written as:

$$n(t,z) = n_0 - \frac{1}{2}\mathbf{s}n^3 I(t,z) \tag{5.7}$$

The radiation pulse, propagating through such kind of medium, experiences a greater refractive index for the central part, which is the most intense. So the first conclusion one may do is that the central part of the beam travels at a lower speed than the peripheral part. The index change causes a temporal

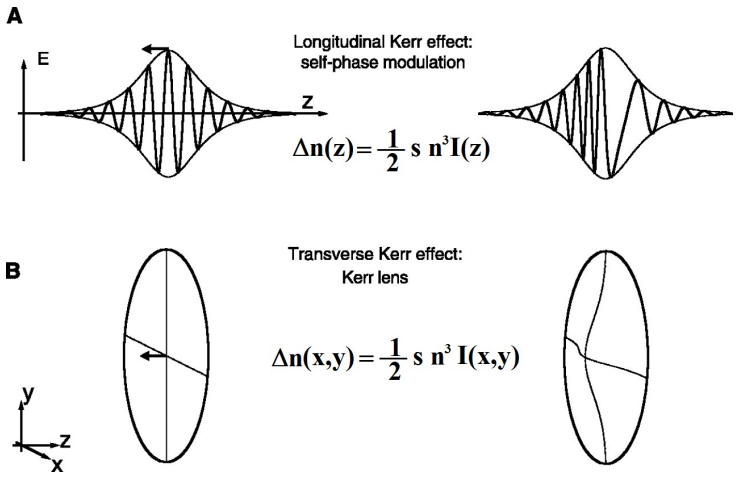

Figure 5.1: The Kerr effect gives rise to an increase of the refractive index with intensity, causing a retardation of the most intense parts of a pulse. In its longitudinal form (A), the Kerr effect causes self-phase modulation; in its transverse form (B), a nonlinear lens is formed in the central part of the beam profile.

delay or phase shift of the most intense parts of a beam. Assuming Gaussian spatial and temporal profiles of pulses, the effects caused by the longitudinal and transverse index change are shown on the Figure 5.1
Delay of the most intense part of a plane wave front transversely acts like a focusing lens, whereas along the axis of propagation, the Kerr effect retards the center of an optical pulse. The longitudinal effect produces a red shift of the leading part of the pulse, and a blue shift in the trailing part and has also been named self phase modulation (SPM). The formation of the Kerr-lens causes the beam to undergo 'self-focusing' when it passes through the medium. Since the degree of self-focusing is intensity dependent, there exists the possibility of introducing an intensity dependent loss mechanism in the cavity. Mode-locking can then occur. Since 'self-focusing' results in a spatial change of the beam, one method is to introduce an aperture or slit into the cavity. The size of the aperture is chosen so that a sufficiently self-focused beam can pass the aperture without attenuation, due to the smaller beam size, whilst a less focused beam will undergo attenuation due to diffraction losses. Use of a physical aperture, can thus create an intensity-dependent loss mechanism that favors higher intensity beams. This mechanism acts like a fast saturable absorber.

5.1.2 Technical specification

The are three variants of Taccor laser. In particolar the laser **Taccor** (T), is optimised for a specific output average power, the **Taccor s** (T-s) is optimised for shorter pulse duration and the last, **Taccor c** (T-c) in which we can select the wavelenght. In Figure 5.3 we show the typical output power of laser taccor [26].

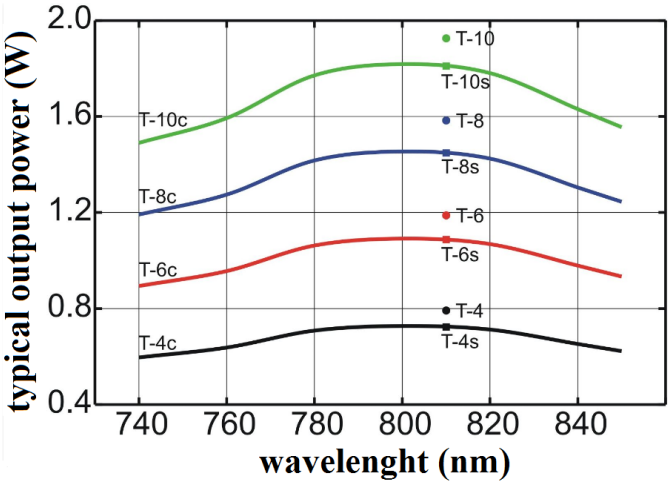

Figure 5.2: Typical output power for all Taccor laser sources.

In this work we used a TACCOR 8 laser source, the main features of which are shown in Table (5.1):

	TACCOR 8
Power	$> 1.6 \ \ W$
Wavelength	$810 \ \ nm$
Repetition rate	$1 \ \ GHz$
Beam waist	$2 \ \ mm$
Pulse duration	$\sim 70 \ \ fs$
Polarization	horizontal

Table 5.1: Specification of Taccor 8

It is very important to know the real size of the laser waist because it is the fundamental parameter that we will use to calculate the focusing condition in the experiment of SH generation. With this purpose, we detected with a

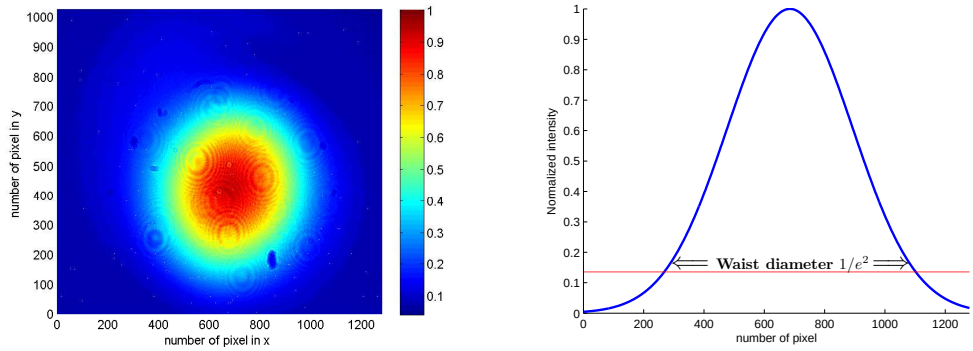

(a) Spot laser captured by CCD camera. (b) Normalized intensity in function of the radial distance

Figure 5.3

CCD camera (Thorlabs DCC1645C) the image of the laser spot.
In Figure 5.3(a) we show the spot of the laser captured by CCD camera in a trasversal plane of the propagation's direction z. In Figure 5.3(b) we show the normalized intensity referred to the x asis in fuction of the radial distance from the propagation axis. The Gaussian profile of the intensity was calculated with matlab auxilium through a Gaussian fit and with this we evaluated the beam waist. The value of the waist was calculated in correspondence with the size of the circle that contains the 86 % of the power ($1/e^2 \sim 0.135$).
It should be denoted that the following bidimensional function was used to fit the normalized intensity of the beam:

$$g(x,y) = exp\left(-\frac{(x-m_x)^2}{\sigma_x^2}\right) exp\left(-\frac{(y-m_y)^2}{\sigma_y^2}\right) \tag{5.8}$$

By knowing the pixel dimension of the camera $L_x = L_y = 3.6 \ \mu m$ and having calculated the parameters $(m_x, \sigma_x^2) = (679.7 \ \ px, 303.7 \ \ px)$ and $(m_y, \sigma_y^2) = (424.9 \ \ px, 277.6 \ \ px)$, we can calculate the beam waist as follows:

$$W_x = \sqrt{2}\sigma_x^2 L_x = 1.5 \ \ mm \tag{5.9}$$

$$W_y = \sqrt{2}\sigma_y^2 L_y = 1.4 \ \ mm \tag{5.10}$$

5.2 The beam focusing

5.2.1 The Gaussian beam

The study of the beam's propagation and its transformation along the optical path is crucial in our analysis. The laser beams have the characteristics to be spatially confined and the free space propagation occurs without large angular spread. In order to satisfy these aspects we begin to describe a beam from a paraxial solution of the Helmholtz equation. A paraxial wave is a plane wave traveling along the z direction e^{-jkz}, modulated by a complex envelope A($\mathbf{r}$) that is slowly varying function of position.

$$U(\mathbf{r}) = A(\mathbf{r})exp(-jkz) \tag{5.11}$$

There are many possible solutions of the paraxial Helmholtz equation and one of these is the Gaussian beam, which is describe by the following complex envelope A($\mathbf{r}$):

$$A(\mathbf{r}) = \frac{A_1}{q(z)}exp\left[-jk\frac{\rho^2}{2q(z)}\right], \quad q(z) = z + jz_0 \tag{5.12}$$

where the quantity $q(z)$ is called **q-parameter** of the beam and z_0 is called **Rayleigh range**. The quantity $q(z)$ can be rewrite by defining two new parameters:

$$\frac{1}{q(z)} = \frac{1}{R(z)} - j\frac{\lambda}{\pi W(z)^2} \tag{5.13}$$

where $R(z)$ is the wavefront radius of curvature and $W(z)$ is the beam width. With these new parameters we can write the complex envelope A($\mathbf{r}$) of the Gaussian beam as:

$$U(\mathbf{r}) = A_0\frac{W_0}{W(z)}exp\left[-\frac{\rho^2}{W(z)^2}\right]\left[-jkz - jk\frac{\rho^2}{2R(z)} + j\zeta(z)\right] \tag{5.14}$$

where the following beam parameters are introduced:

$$W(z) = W_0\sqrt{1 + \left(\frac{z}{z_0}\right)^2} \tag{5.15}$$

$$R(z) = z\left[1 + \left(\frac{z_0}{z}\right)^2\right] \tag{5.16}$$

$$\zeta(z) = \tan^-1\left(\frac{z}{z_0}\right) \tag{5.17}$$

$$W_0 = \sqrt{\frac{\lambda z_0}{\pi}} \tag{5.18}$$

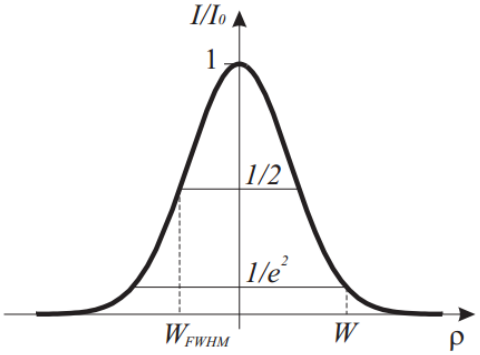

(a) Normalized intensity

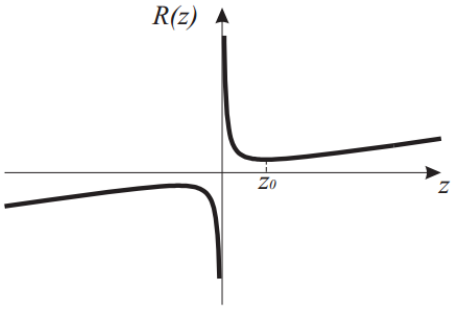

(b) Radius of beam curvature

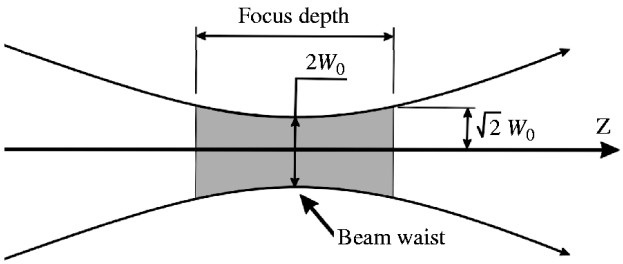

(c) Beam waist, beam radius and focus depth

Figure 5.4

In Figure 5.4 we present the main features of the Gaussian beam, in particular we show that the optical intensity is given by the square of the absolute value of complex field amplitude introduced in equation 5.14:

$$I(\rho, z) = I_0 \left(\frac{W_0}{W(z)}\right)^2 exp\left[-\frac{2\rho^2}{W(z)^2}\right] \tag{5.19}$$

where $I_0 = |A_0|^2$.
In Figure 5.4(a) we define also the $W_{FWHM}(z)$ which is the diameter of the beam when the intensity is half of the maximum intensity and $W(z)$ when the intensity is the 13.5 % of the maximum power. In Figure 5.4(b) we plot the wavefront curvature $R(z)$, that decreases to its minimum value at $z = z_0$ and we also see that $R(0)$ is infinite, that means that at $z = 0$ we have a plane wavefront. To investigate how the beam radius behaves in z

direction we can plot $W(z)$ and we can see that if the wavefront is far enough from the center of the beam, the beam radius grows linearly. However, we define two important parameters that are the **depth of focus** or **confocal parameter** $2z_0$ where is the axial distance within which the beam width is no greater than a factor $\sqrt{2}$ times its minimum value (Figure 5.4(c)), and the **divergence angle** $2\theta_0$ that is directly proportional to the wavelength and inversely proportional to the spot size.

$$2z_0 = \frac{2\pi W_0^2}{\lambda} \tag{5.20}$$

$$2\theta_0 = 2\frac{\lambda}{\pi W_0} \tag{5.21}$$

5.2.2 Gaussian trasformation through a thin lens

By passing an optical system like a lens the parameters of a gaussian beam, like the waist size and waist position, are generally changed. We will refer to this fact as *gaussian transformation*.
In this work, we needed to reshape the laser beam parameters and we made this through the use of lenses system. When a Gaussian beam is transmitted through a set of thin lenses aligned with the beam axis, this beam remains Gaussian and it is reshaped. However, its parameters like phase, waist and curvature are altered. In general the parameters of the emerging beam through a thin lens like the beam waist $W_0^{'}$, curvature $R^{'}$ and distance from the lens $-z^{'}$ are provided by the following equations:

$$W_0^{'} = \frac{W}{\sqrt{1 + (\pi W^2/\lambda R^{'})^2}} \tag{5.22}$$

$$-z^{'} = \frac{R^{'}}{1 + (\lambda R^{'}/\pi W^2)^2} \tag{5.23}$$

where

$$\frac{1}{R^{'}} = \frac{1}{R} - \frac{1}{f} \tag{5.24}$$

Consider the TACCOR laser beam at $\lambda = 810 \ \ nm$ with waist radius of $W_0 = 1.5 \ \ mm$, these parameters allow us to calculate the confocal parameter of the beam as:

$$2z_0 = \frac{2\pi W_0^2}{\lambda} = 17.45 \ \ m \tag{5.25}$$

Our optical path of the experiment is shorter than the confocal parameter of the beam and for this reason we will see that the lens, that focuses the beam

into the SH nonlinear cristal, is placed in the waist of the Gaussian beam. If a thin lens is placed at the waist of a Gaussian beam, the trasmitted beam is then focused in a waist radius $W_0^{'}$ at a distance $z^{'}$ given by:

$$W_0^{'} = \frac{W_0}{\sqrt{1 + (z_0/f)^2}} \tag{5.26}$$

$$z^{'} = \frac{f}{\sqrt{1 + (f/z_0)^2}} \tag{5.27}$$

Futhermore, in the special case in which the depth of focus of the incident beam $2z_0$ is much longer than the focal length f of the lens, this condition leads to the following semplifications:

$$W_0^{'} \approx \frac{\lambda}{\pi W_0} f = \theta_0 f \tag{5.28}$$

$$z^{'} \approx f \tag{5.29}$$

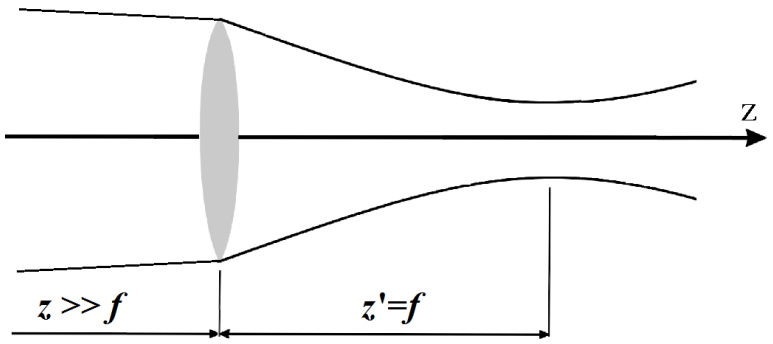

Figure 5.5: Focusing of a collimated beam.

5.2.3 SHG with focused Gaussian beam

The conversion efficiency of SHG may be greatly anhanced by focussing the pump beam into the nonlinear crystal. The longitudinal dimension of the focal region is defined by the focussing parameter ξ given by:

$$\xi = \frac{L}{b} \tag{5.30}$$

where L is the interaction length of the nonlinear crystal and $b = 2z_0$ is the confocal parameter.
If the crystal length L is smaller than the confocal parameter b, then tighter focusing increases the efficiency. If b is grater than L, however the plane-wave approximation breaks down and tighter focusing tends to reduced the conversion efficiency. Boyd and Kleinman [26] studied the focussing problem in detail. They introduced a factor $h(B, \xi)$ to include all the effects of focusing and any phase mismatch. For a focused fundamental Gaussian beam with beam cross-section $A = \pi W_0^2$ where W_0 is the beam waist radius, and with an interaction length L, we can get the SH generation power as follows:

$$P_{SH} = \left(\frac{2\omega_F^2 d_{eff}^2 k_F P_F^2}{\pi n_F^2 n_{SH} \varepsilon_0 c_0^2} \right) L h(B, \xi) \tag{5.31}$$

The factor B is the double refraction parameter that depends on the presence of the walk-off in nonlinear medium. If there is no walk-off, B=0 and $h(B, \xi) = h(\chi)$.

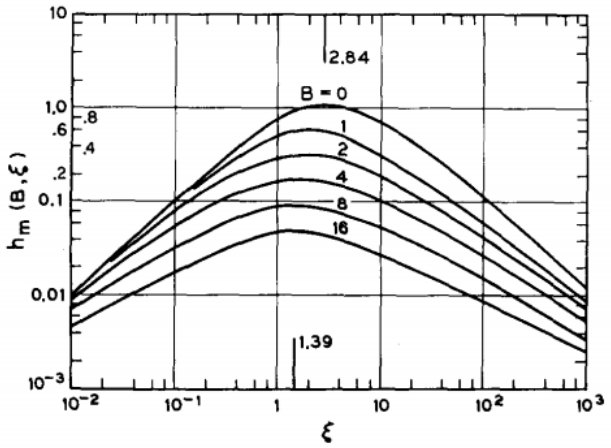

Figure 5.6: The trend of the focusing factor $h(B, \xi)$ due to focusing effects.

In Figure 5.6 we show the factor $h(B, \xi)$ against ξ for different values of B. As there is no walk-off in PPKTP, $B = 0$ and the highest value of $h(0, \xi) = 1.068$ when $\xi = 2.84$. Note that this theory assumes no pump depletion approximation.
In our experiment we used a PPKTP of length $L = 5 \ \ mm$, if we want to maximize the focusing condition, the confocal parameter of the fundamental beam should be:

$$b = 2z_0^{'} = \frac{L}{\xi} = \frac{5 \ \ mm}{2.84} \simeq 1.76 \ \ mm \tag{5.32}$$

where $b = 2\pi n_F W_0^2/\lambda$.
Consideing the refractive index of the PPKTP at fundamental wavelength $\lambda = 810\ \ nm$ equal to $n_F \simeq 1.84$ (using the Sellmeire equation (4.5)), we can calulate the beam waist $W_0^{'}$ that is equal to:

$$W_0^{'} = \sqrt{\frac{\lambda b}{2\pi n_F}} \simeq 11\ \ \mu m \tag{5.33}$$

It is necessary to stress that we cannot use the $W_0^{'}$ by itself. We have to compare this parameter with the crystal damage threshold; in other words, we have to compare the spot size with the maximum power density that the crystal can endure.

5.2.4 Evaluation of focusing parameter

In the SHG experiment we have tested different focusing conditions in order to obtain the maximum conversion efficiency. For this purpose we used a system composed of a single lens to focus the fundamental beam inside the crystal.
Now we will calculate for different values of the focal length f the parameters of the transmitted Gaussian beam as the waist radius and the confocal parameter; futhermore we will calculate the value of the focusing factor $h(0,\xi)$. Since our laser beam is characterized by having a confocal parameter much longer than the used focal length, we can use equation (5.28) to calculate the waist radius. In the following table we show the parameters for each focal lens used.

Focal length (mm)	**Beam waist** (μm)	**Confocal parameter** (mm)	**confocal factor**
L1	$W_0^{'} = \frac{\lambda}{\pi W_0} f$	$b = 2z_0^{'} = \frac{2\pi n_F W_0^{'2}}{\lambda}$	$h(0,\xi) = \frac{L}{b}$
75	12.89	2.37	2.11
100	17.19	4.22	1.18
120	20.63	6.07	0.82
150	25.78	9.49	0.53

Table 5.2: Focusing parameters.

where $n_F \simeq 1.84$, $W_0 = 1.5\ \ mm$,$L = 5\ \ mm$ and $\lambda = 810\ \ nm$.

5.3 Setup of SHG experiment

In Figure (5.7), we show a schematic diagram of our experimental setup to generate second harmonic. The fundamental laser beam comes from the laser source TACCOR8. In the first part of the path there are two mirror (BB1-E03) and one half wave plate that changes the polarization of fundamental beam from horizontal to vertical.

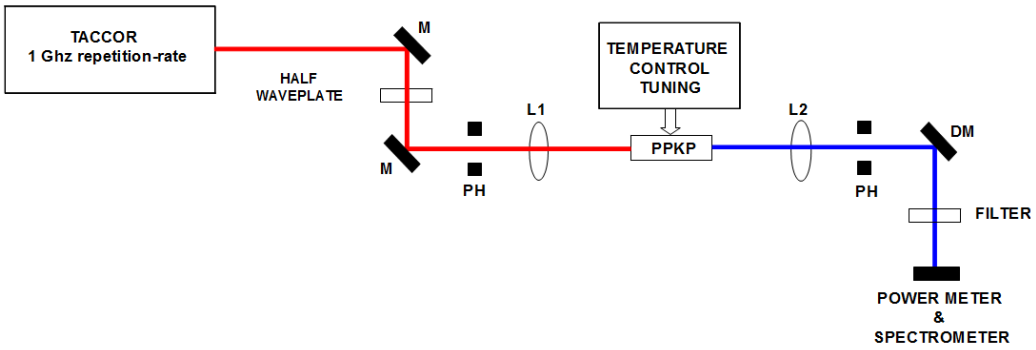

Figure 5.7: Experimental stup of SHG with PPKTP.

Then there is a pairs of pinholes to select the correct path, and a pair of lenses, L1 and L2. Lens L1 is used to manipulate the q-parameter of the fundamental beam in order to obtain the optimal focusing condition. Lens L2 is used to refocus the beam after the crystal, only if lens L1 is used with short focal length. The lenses are distinguished according to the reflectivity of the incident radiation. For this reason they are characterized by different anti-reflective coating. In particular, the coating A is used for $\lambda = 405 \ \ nm$, the coating B for $\lambda = 810 \ \ nm$. In our case we have to use the lens L1 with coating B and the lens L2 with coating A (Figure 5.8).

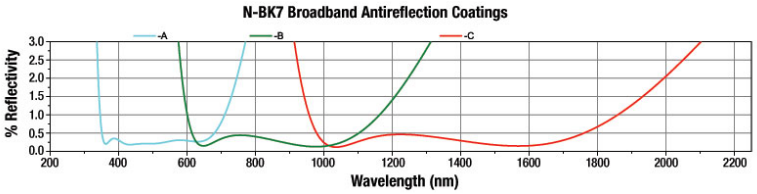

Figure 5.8: Trend of anti-refrected coated A,B and C.

After the lens L1 there is the crystal of second harmonic: BBO, BiBO and PPKTP with temperature control tuning. At the end of the path, after lens

L2, we used a dicrohic mirrors and a filter to eliminate the pump beam and to select only the wavelenght of second harmonic at $\lambda = 405 \ \ nm$.
The dicrohic mirror is used to reflect the SH along the optical path and trasmitting the fundamental beam blocking it immediately behind the mirror through a beam stop. The dicrohic mirror that we used is a Thorlabs DMLP567 and in figure (5.9) we show the trend of the transissivity and refrectivity at function of the wavelength.

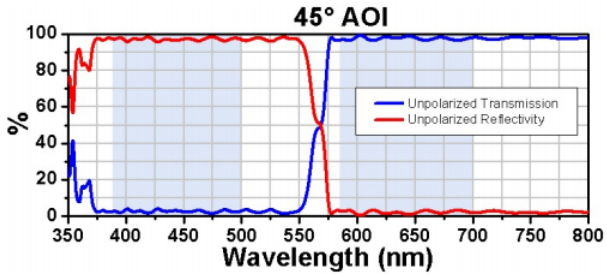

Figure 5.9: Trasissivity and refrectivity of the dichroic mirror DMLP567.

However, the dichroic mirror is not able to eliminate completely the pump beam, so we must use a filter to eliminate the residual pump beam. In this way we are sure that the measured power is due only to the second harmonic component, but above all it is important that in the experiment of photon-pairs generation, the pump beam is precisely at $\lambda = 405 \ \ nm$. The filter that we used is a Thorlab FB405 with bandwidth of 10 nm. In Figure 5.10, we show the percentage of the transmissivity in function of the wavelength.

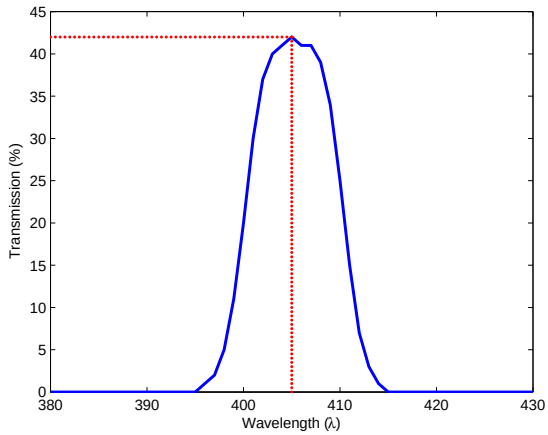

Figure 5.10: Filter Thorlabs at $\lambda = 405 \ \ nm$

After the filter we measure the power of SH with a power meter (Thorlabs

PM100) and we register the spectrum of SH with a spectrometer (Ocean Optics HR4000).
The value of the efficiency of transmission at $\lambda = 405\ \ nm$ is very important because allows us to calculate the real efficiency of SH generated. If P_{SH} is the value of SH power measured by power meter and P_F is the power of fundamental beam at the entrance of the crystal, the real conversion efficiency of SH is equal to:

$$\eta = \frac{P_{SH}}{P_F} \frac{1}{\eta_{FILTER}} \tag{5.34}$$

with $\eta_{FILTER} = 42\ \ \%$.
The spectrum of second harmonic generation with PPKTP crystal has a narrow spectral width (as we will see in Chapter 5) that is comparable with the spectrometer resolution $\Delta\lambda \approx 0.3\ \ nm$. For this reason we also performed a measurement of the SH coherence time by using a Michelson interferometer.

5.4 Nonlinear crystals

In this section we will report the main features of the nonlinear crystals that we used in the experiments.

5.4.1 PPKTP crystal

We used a PPKTP crystal that was fabricated by Raicol Crystals with electric poling technique. The dimension of the crystal are 1 mm thick, 2 mm wide and 5 mm length. It is a Type I ($e + e \rightarrow e$) uncoated crystal in which the d_{33} nonlinear coefficient was utilized.
To maximize the efficiency, the crystal implements a first-order quasi phase matching with grating period of $\Lambda = 3.425\ \ \mu m$ and duty cicle $D = 50\ \ \%$. The grating period had been designed for QPM at $T \sim 25° - 50°$. The relationship of the refractive index in function of the wavelength it was reported by Sellmeire equation (4.5) in Capter 4. Here we report the trend of the refractive index (Figure 5.11) and subsequentely we show the index at fundamental and SH wavelength.

$$\lambda_F = 810\ \ nm: \qquad n_F = 1.8424, \tag{5.35}$$

$$\lambda_{SH} = 405\ \ nm: \qquad n_{SH} = 1.8669, \tag{5.36}$$

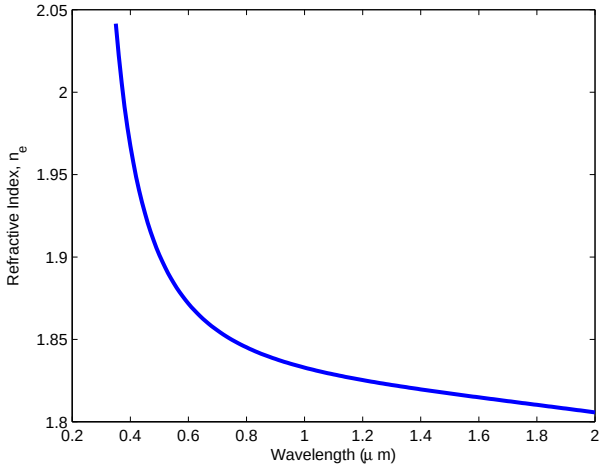

Figure 5.11: The trend of refractive index in PPKTP

5.4.2 BBO crystal

We used a Beta-Barium Borate crystal (BBO),Type I ($e + e \rightarrow o$) length $L = 1 \ \ mm$ with anti-refracting coating at 405 and 810 $\ nm$.
In Figure 5.12 we show that the crystal is negative uniaxial with $n_0 > n_e$ and the dipendence of refractive indices n_0 and n_e on the wavelength is given by Sellmeire equation:

$$n^2 = A + \frac{B}{\lambda^2 - C} - D\lambda^2 \tag{5.37}$$

where the coefficient of the Sellmeire equation for ordinary and extraordinary indices are in Table 5.3 [15]. For fundamental and SH beam the indices are:

$$\lambda = 405 \ \ nm: \qquad n_0 = 1.6919 \qquad n_e = 1.5671 \tag{5.38}$$

$$\lambda = 810 \ \ nm: \qquad n_0 = 1.6603 \qquad n_e = 1.5442 \tag{5.39}$$

In this crystal the phase matching condition is achieved by birefringence

	A	B	C (μm^2)	D (μm^{-2})
n_0	2.7359	0.01878	0.01822	0.01354
n_e	2.3753	0.01224	0.01667	0.01516

Table 5.3: Sellmeire parameters for BBO.

according to equation 2.65, and in order to obtain the perfect phase matching and the maximum of the efficiency, the crystal is mounted in a support with angle tuned. The effective nonlinear coefficient is $d_{eff} \sim 1 - 2 \ \ pm/V$.

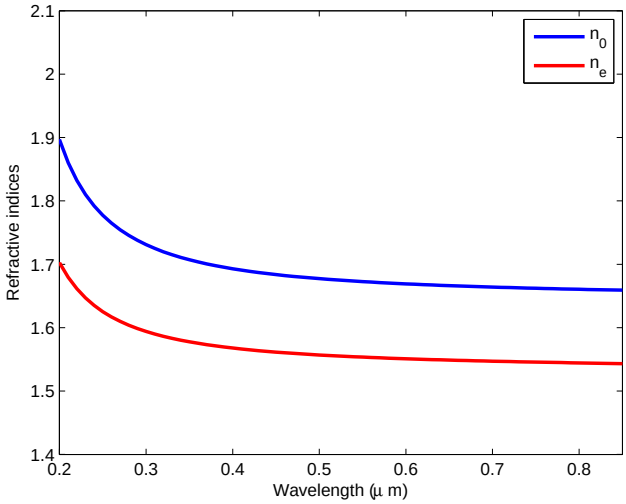

Figure 5.12: The trend of ordinary and extraordinary index in BBO crystal

5.4.3 BiBO

Finally, we have tested the SHG with a 1 mm length BiBO crystal, Type I ($e+e \rightarrow o$). It is a biaxial cristal and the refractive indices in the three axial directions are calculated by the following Sellmeire equations:

$$n_x^2 = 3.0740 + \frac{0.0323}{(\lambda^2 - 0.0316)} - 0.01337\lambda^2 \tag{5.40}$$

$$n_y^2 = 3.1685 + \frac{0.0373}{(\lambda^2 - 0.0346} - 0.01750\lambda^2 \tag{5.41}$$

$$n_z^2 = 3.6545 + \frac{0.0511}{\lambda^2 - 0.0371} - 0.0226\lambda^2 \tag{5.42}$$

where in our wavelengths the refractive indices are:

$$\lambda_{SH} = 405 \;\; nm: \qquad n_x = 1.8209 \qquad n_y = 1.8584 \qquad n_z = 2.0133 \tag{5.43}$$

$$\lambda_F = 810 \;\; nm: \qquad n_x = 1.7655 \qquad n_y = 1.7936 \qquad n_z = 1.9293 \tag{5.44}$$

In Figure 5.13, we show the trend of all refractive indices. It is usual, in each plane we designate the polarization direction normal to the plane by o and corrispondent refractive index (n_o) and the other allowed polarization parallel to the plane by e and correspondent refractive index (n_e). The most interesting plane for nonlinear optical interactions is yz, which offers the

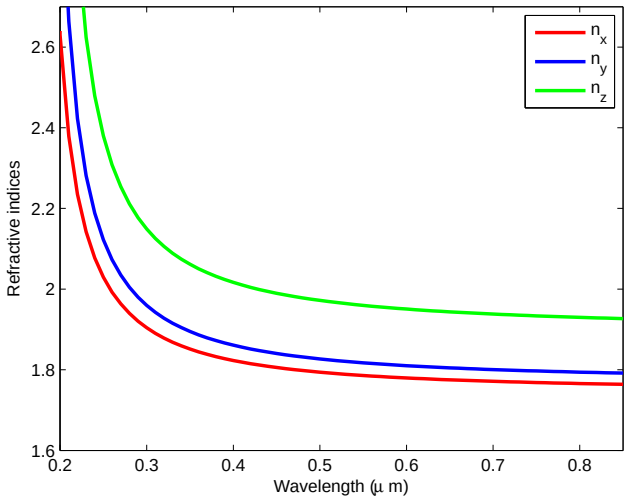

Figure 5.13: The tren of refractive indices n_x, n_y, n_z of BiBO crystal

highest effective nonlinearity, with a maximum value $d_{eff} \sim 3.4 \ \ pm/V$ [2]. This crystal is cut at $\phi = 90°$ and there are two possible phase matching angle at $\theta = 151.1°$ and $180° - \theta = 28.9°$.

5.5 Measurement of the coherence time

5.5.1 Coherence Time

Another interesting parameter that we measured in our experiments is the coherence time of a wave. The coherence time can be used to quantify the degree of temporal coherence of light. In other words, it is the time interval within which its phase is, on average, predictable.
The intensity of coherent light is related to the absolute square of the complex wavefunction $U(\mathbf{r}, t)$.

$$I(\mathbf{r}, \mathbf{t}) = |\mathbf{U}(\mathbf{r}, \mathbf{t})|^{\mathbf{2}} \tag{5.45}$$

For a pulsed light, the intensity is time varying and the quantity $U(t)$ (for brevity we need not explicitly indicate the $\mathbf{r}$ dipendence since r is fixed) is a fluctuation's function. This function is characterized by a time scale representing the "memory" of the function's fluctuation. After this time, the process "forget itself", so that fluctuations at point separated by a time interval longer than this time scale are indipendent. The measure of this temporal behavior is established by an autocorrelation function. The autocorrelation

function of $U(t)$ is defined as follows:

$$G(\tau) = \langle U^*(t)U(t+\tau)\rangle \tag{5.46}$$

This function is know as the temporal coherence function that carries information about both intensity $I = G(0)$ and the degree of coherence of light. A measure of the degrr of correlation between $U(t)$ and $U(t+\tau)$ is the function:

$$g(\tau) = \frac{G(\tau)}{G(0)} = \frac{\langle U^*(t)U(t+\tau)\rangle}{\langle U^*(t)U(t)\rangle} \tag{5.47}$$

which is called the complex degree of temporal coherence.
If $|g(\tau)|$ decreases with time delay, the value τ_c at which it drops to a prescribed value serves as a measure of the memory time of the fluctuations. The quantity τ_c is know as the coherence time. The distance that a wave travels in a coherence time τ_c is called coherence. length:

$$l_c = c\tau \tag{5.48}$$

If we want to know the coherence time of a wave, it is possible to derive this value through the measure of the coherence length. The measurement of the coherence length can be done directly through the use of a Michelson interferometer.

5.5.2 Michelson Interferometer

In this work we used the Michelson Interferometer to measure the coherence time of the SH wave. In our SHG setup we have built a Michelson interforemeter after the filter FB405 and this setup is illustated in Figure x.
The SH wave coming from the SH nonlinear crystal is split into two parts. One part of the light travels a different path length than the other. After traversing these different path lengths, the two parts of the light are brought together to interfere with each other and the interference pattern can be seen with a CCD camera (Thorlabs DCC1645C). The SH beam strikes the beam splitter that allows 50 % of the radiation to be transmitted to the moving mirror and the other 50 % of the radiation to be reflected to the fixed mirror. After one of the two partis of the light (50 %) is reflected toward the CCD camera. Likewise, the second part of the light (50 %) is transmitted to the CCD camera. The two beams are superposed and we can observe the interference between them on the camera.
In this way, on the image plane of the camera we can se the superposition of two waves; $U_1(t)$ reflected by the fixed mirror and $U_2(t)$ reflected by the

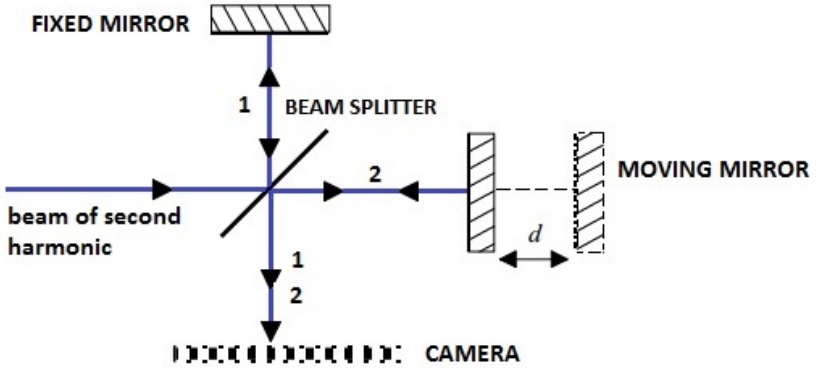

Figure 5.14

moving mirror. The wave $U_2(t)$ is superimposed to the first $U_1(t)$ with a certain temporal delay due to the greater path of $2d$.

$$U_2(t) = U_1(t+\tau) \tag{5.49}$$

where $\tau = \frac{2d}{c}$.
Then the resulting field on the image plane is characterized by the following intensity:

$$I = \langle |U_1(t) + |U_1(t+\tau)|^2 \rangle = \langle |U(t)|^2 \rangle + \langle |U(t+\tau)|^2 \langle + [\langle U(t+\tau)U(t)^* \rangle +$$

$$+ \langle U(t+\tau)^* U(t) \rangle]$$

and

$$I = I_1 + I_2 + 2Re[G(\tau)] \tag{5.50}$$

If a wave is coherence then it forms interference fringes and we can define a visibility of a fringe as:

$$V = \frac{I_{max} - I_{min}}{I_{max} + I_{min}} \tag{5.51}$$

where:

$$I_{max} = I_1 + I_2 + \sqrt{I_1 I_2}|G(\tau)|, \tag{5.52}$$

$$I_{min} = I_1 + I_2 - \sqrt{I_1 I_2}|G(\tau)| \tag{5.53}$$

So we can write the visibility as a function of the complex coherence degree as follows:

$$V = \frac{2\sqrt{I_1}\sqrt{I_2}}{I_1 + I2}|G(\tau)| \tag{5.54}$$

and if $I_1 = I_2$ the visibility is directly proporzional of the complex degree of coherence, then we can rewrite it in this way.

$$V = |G(\tau)| \tag{5.55}$$

So by measuring the visibility of the fringes we can derive the coherence time of the second harmonic beam.

5.6 Experimental setup of photon-pairs generations

After generating and characterizing the second harmonic, the experiment includes the generation and the measurement of the entangled photon pairs using the spontaneous parametric down conversion (Figura 5.15).

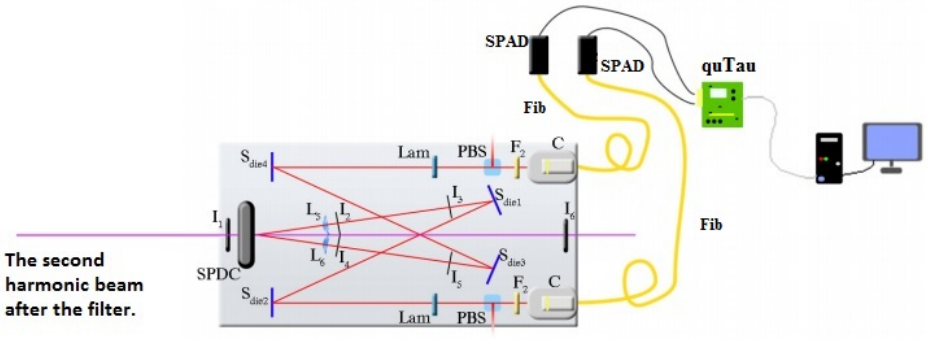

Figure 5.15: Setup of Entangled photon-pairs generation

The crystal used for SPDC is a BBO type II of 2 mm length, mounted on a tip tilt support with rotation, in order to obtain the right phase matching. The beam that impact on the crystal comes from the SH crystal that has to be well collimated using the lens L2 located after the crystal. We let the beam pass through two pin holes I_5 and I_6 so that the optical path is as much aligned as possible. These conditions are really important, because if the position is nof well focused even of few mm, the loss in efficiency is about 20 %. The produced parametric radiation follows the two paths as shown in Figure 5.15. It is important that the two paths have the same length, to allow photons to arrive at the same time and to pemit in this way the coincidence. Along the two paths we can notice the presence of two lenses $L5$ and $L6$ with

$f = 100 \ \ mm$ that allow a better collimation of the parametric radiation enhancing the system's efficiency.
Waveplates $\lambda/2$ and PBS (polarization beam splitter) project the photons states on the basis $|HV\rangle, |VH\rangle, |+-\rangle$ and $|-+\rangle$. The state $|HV\rangle$ is obtained imposing one wave plate at 0° and the other one at 45°, while for the state $|VH\rangle$ the first waveplate is at 45° and the second one at 0°. In the same way, if we want to obtain the projection on the state $|+-\rangle$ we have to impose a wave plate at 67.5° and the other at 22.5°, while for the state $|-+\rangle$ the first wave is at 22.5° and the second at 67.5°. Finally, the parametric beams are collimated with a single mode fiber connected to the SPAD.
The SPAD (Single Photon Avalanche Diode) is a solid-state photodetector based on a reverse polarization pn junction. It can generate an output current in response to the detection of signals at very low intensity (such as the detection of a photon) thanks to the phenomenon of ionization by impact, that allows high internal amplification. For each detected event, the SPAD outputs a TTL pulse.Than, SPAD are connected to the Qu-tau system and to the PC for the aquisition and the recording of coincidenses.

Chapter 6

Analysis of the results

Now, we will present the results of our experiments. In the first part of this chapter we will explain the conventions used for the calculation of parameters and results analysis. In the second part we will present the results of the SH experiment referring to the three nonlinear crystals used and we will show what we turned out from the Entangled photon-pairs generation. This last experiment was carried out using only the PPKTP crystal that is the most important crystal of this work.

6.1 Temporal and spectral representations

The characterization of the laser source is very important for the analysis of the results. A pulsed laser source is described by an optical field of finite time duration and we can use a complex wavefunction $U(\mathbf{r}, t)$ to describe the field components. In general an optical pulse of central frequency ν_0 is written as follows:

$$U(t) = A(t)exp(j\omega_0 t) \tag{6.1}$$

where $A(t)$ is the complex envelope.
The intensity profile $I(t) = |U(t)|^2$ of the TACCOR laser pulse is Gaussian and its function is:

$$I(t) \propto exp(-2t^2/\tau^2) \tag{6.2}$$

and in the spectral domain, the pulse is defined by the Fourier transform:

$$V(\nu) = \int_{-\infty}^{+\infty} U(t)exp(-j2\pi\nu t)dt \tag{6.3}$$

whith $V(\nu) = |V(\nu)|exp(j\phi(\nu))$.
The quantity $S(\nu) = |V(\nu)|^2$ is the spectral intensity of the laser pulse and

$\phi(\nu)$ is the spectral phase.
When we measure the spectral intensity with a spectrometer, it is plotted as a function of the wavelength $|S(\lambda)|$ and for this reason the spectral width $\Delta\nu$ may also be converted into wavelength units. In our case $\Delta\nu \ll \nu_0$ and:

$$\Delta\lambda \approx \frac{\lambda_0^2}{c}\Delta\nu \tag{6.4}$$

Now, we want to calculate the parameter of coherence time, temporal and spectral width at FWHM of the TACCOR laser pulse. We consider a transform limited Gaussian pulse and its expression of the spectral intensity at FWHM is:

$$S(\nu) = exp\left(-4ln2\frac{\nu^2}{\Delta\nu^2}\right) \tag{6.5}$$

and consequentely:

$$S(\nu) = |V(\nu)|^2 \quad \Rightarrow \quad V(\nu) = exp\left(-2ln2\frac{\nu^2}{\Delta\nu^2}\right) \tag{6.6}$$

To calculate the expression of $U(t)$ in the time domain, is enough to apply the anti Fourier transform to $V(\nu)$ as follows:

$$U(t) = \int_{-\infty}^{+\infty} exp\left(-\alpha^2\nu^2\right) exp(j2\pi\nu t)d\nu \tag{6.7}$$

with $\alpha^2 = \frac{2ln2}{\Delta\nu^2}$.

$$\Rightarrow \quad U(t) = exp\left(-\frac{\pi^2t^2}{\alpha^2}\right)\int_{-\infty}^{+\infty} exp\left(-\alpha\nu - j\frac{\pi t}{\alpha}\right)^2 d\nu =$$

$$= \frac{exp\left(-\frac{\pi^2t^2}{\alpha^2}\right)}{\alpha}\int_{-\infty}^{+\infty} exp(-k^2)dk = \sqrt{\pi}$$

Then, the temporal representation of the laser pulse is:

$$U(t) = \frac{\sqrt{\pi}exp\left(-\frac{\pi^2t^2}{\alpha^2}\right)}{\alpha} \tag{6.8}$$

However, the tranform limited gaussian pulse has the following expression of U(t):

$$U(t) = exp\left(-\frac{2ln(2)t^2}{\tau_{FWHM}}\right) \tag{6.9}$$

and then:

$$\frac{\pi^2 t^2}{2ln2}\Delta\nu^2 = \frac{2ln(2)t^2}{\tau_{FWHM}} \tag{6.10}$$

So the product of the FWHM temporal and spectral widths is:

$$\Delta\nu\tau_{FWHM} = \frac{2}{\pi}ln2 = 0.44 \tag{6.11}$$

Now, we calculate the expression of autocorrelation function to find the coherence time τ_c:

$$G(T) = \langle U^*(t)U(t+T)\rangle = \int_{-\infty}^{+\infty} exp\left(-\frac{2ln(2)}{\tau_{FWHM}^2}\left[t^2 + (t^2+T)^2\right]\right)dt \tag{6.12}$$

$$\Rightarrow \int_{-\infty}^{+\infty} exp\left(-\beta\left[2t^2 + 2Tt + T^2\right]\right)dt = exp\left(-\frac{\beta}{2}T^2\right)$$

where $\beta = \frac{2ln(2)}{\tau_{FWHM}^2}$ and we applied the following integral:

$$\int_{-\infty}^{\infty} exp(-[ax^2 + bx + c])dx = exp(-b^2/4a)$$

From this expression of $G(T)$ we can calculate the complex degree of temporal coherence as:

$$g(T) = \frac{G(T)}{G(0)} = exp\left(-\frac{\beta}{2}T^2\right) \tag{6.13}$$

Considering the expression for the complex degree of temporal coherence that is [15]:

$$g(T) = exp\left(-\frac{\pi T^2}{2\tau_c^2}\right) \tag{6.14}$$

we can write the following equality:

$$\frac{2ln(2)}{\tau_{FWHM}}T^2 = \frac{\pi}{2\tau_c^2}T^2 \tag{6.15}$$

So the product of the FWHM spectral widths and coherence time is:

$$\Delta\nu\tau_c = \sqrt{\frac{2}{\pi}ln2} = 0.66 \tag{6.16}$$

6.2 Results of the SHG experiment

In this sections we present the results of the SHG experiment with three different nonlinear materials (PPKTP-BBO-BiBO). For each different nonlinear crystal we show the spectrum of SH and an image of the spot, and we calculate the power and efficiency of SH, the spectral width, the pulse duration and the coherence time. In particular the spectral width is calculated using an estimation through a Gaussian fitting and for each spectrum we use the following function of fitting:

$$g(x) = exp\left(-4ln2\frac{(x-m_x)^2}{\sigma_x^2}\right) \tag{6.17}$$

Before each measurement's test the power and the spectrum of the pump beam were measured at the input of the crystal. The behaviour of the pump beam was stable in all experiments in which we measured a fundamental power $P_F = 1.4 \;\; W$. The spectrum of fundamental beam is shown in Figure 6.1.

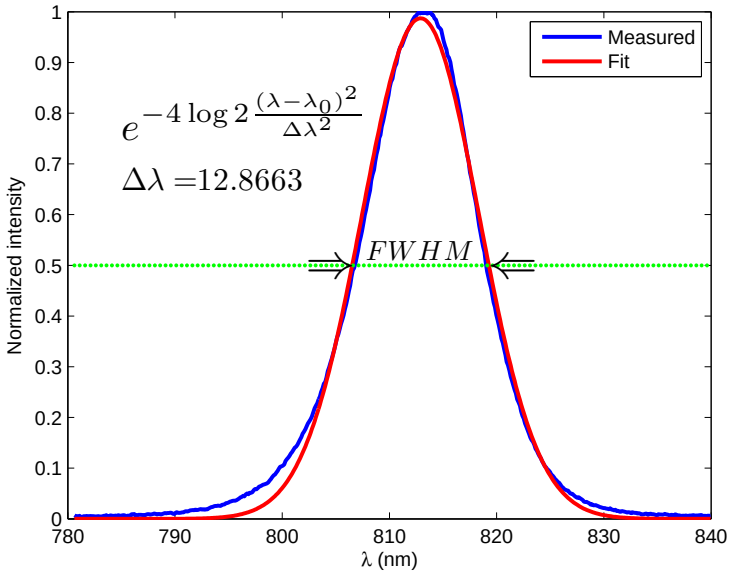

Figure 6.1: Spectrum of TACCOR laser source with Gaussian fitting.

Finally, we calculate the time duration of the pump beam using the conventions that we demostated in the previous section.

$$\tau_{FWHM} = 0.44\frac{\lambda_0^2}{c_0\Delta\lambda_0} \simeq= 75 \;\; fs \tag{6.18}$$

where $\lambda_0 = 810 \ \ nm$ and $\Delta\lambda_0 = 12.8663 \ \ nm$.

6.2.1 Results with PPKTP

In order to obtain the maximum effciency of SHG with PPKTP, we have tested different focusing conditions, and for each of these, we have performed a temperature scan from $T = 25°C$ to $T = 130°C$. When we run the temperature scan of the PPKTP, we must be careful not to increase the temperature of the crystal too fast. According to the specifications, the temperature should be increased with a speed of $< 10°C/min$.

6.2.2 The problem of the photorefractive effect

In this experiment we did not find a stable condition of SHG in all focusing conditions. For the L1 lens with focal lenght $f \leq 120 \ \ mm$ the measurement of the power was very unstable, in some cases impracticable, like in the cases of $f = 75 \ \ mm$ and $f = 100 \ \ mm$, because the spectrum of the second harmonic widens over time due to the photorefractive effect. This unwelcome effect preserving good beam quality and stable spectrum is of the utmost importance, and the photorefractive effect can cause beam distortion and scattering, leading to deterioration in the entangled pair generation process. The following figures (ordered temporally for the $40°C$ case) show the broadening of the second harmonic spectrum and the change of the SH power caused by the photorefractive effect. The data are obtained with a 100 mm focal length. It is possible to note that the spectrum and the SHG power change over time both in the $40°C$ and in the $50°C$ case.

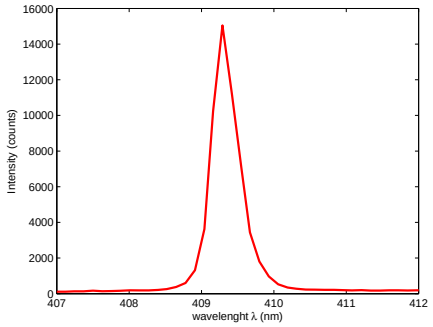

(a) $T = 40 \ °C$ and $P_{SH} = 39.7 \ mW$

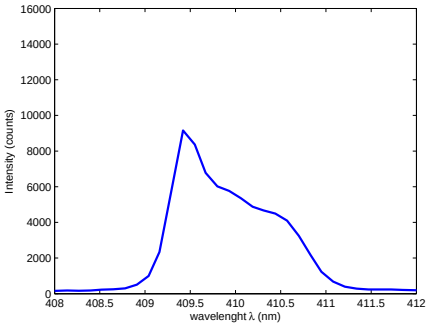

(b) $T = 40 \ °C$ and $P_{SH} = 44.2 \ mW$

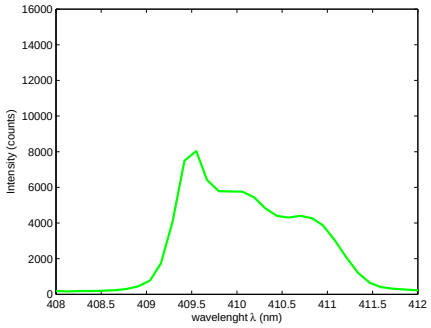

(c) $T = 40\ °C$ and $P_{SH} = 39.7\ mW$

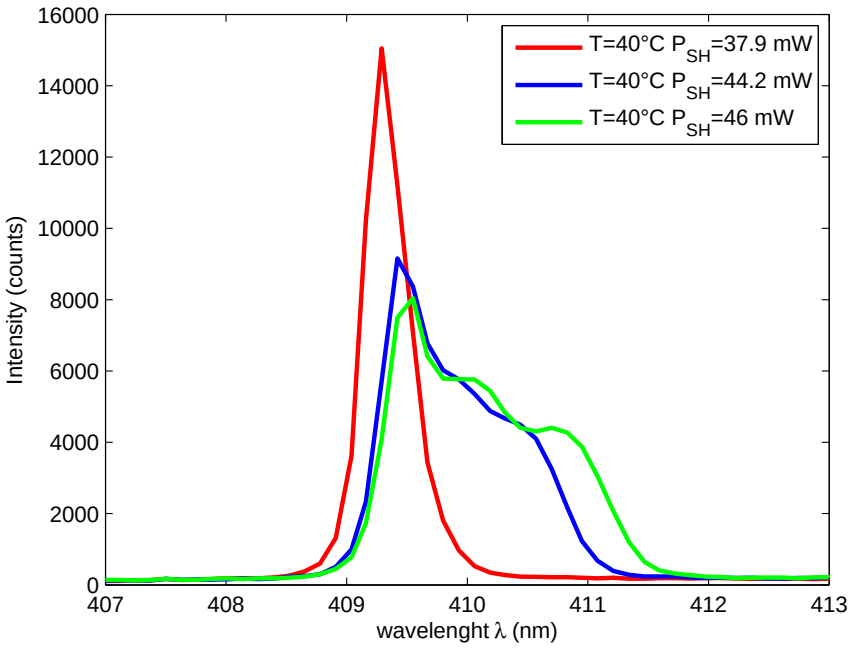

(d) Global view of the effect

Figure 6.2: Photorefractive effect at $T = 40°C$

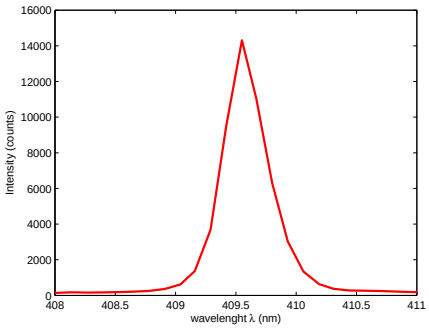

(a) $T = 50\ ^{\circ}C$ and $P_{SH} = 42.5\ mW$

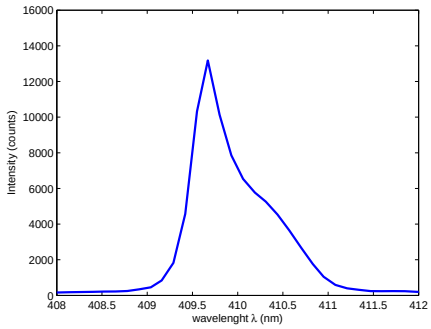

(b) $T = 50\ ^{\circ}C$ and $P_{SH} = 45.5\ mW$

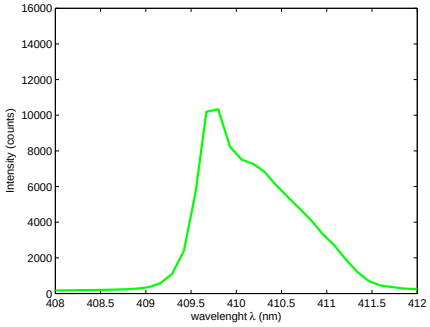

(c) $T = 50\ ^{\circ}C$ and $P_{SH} = 46.3\ mW$

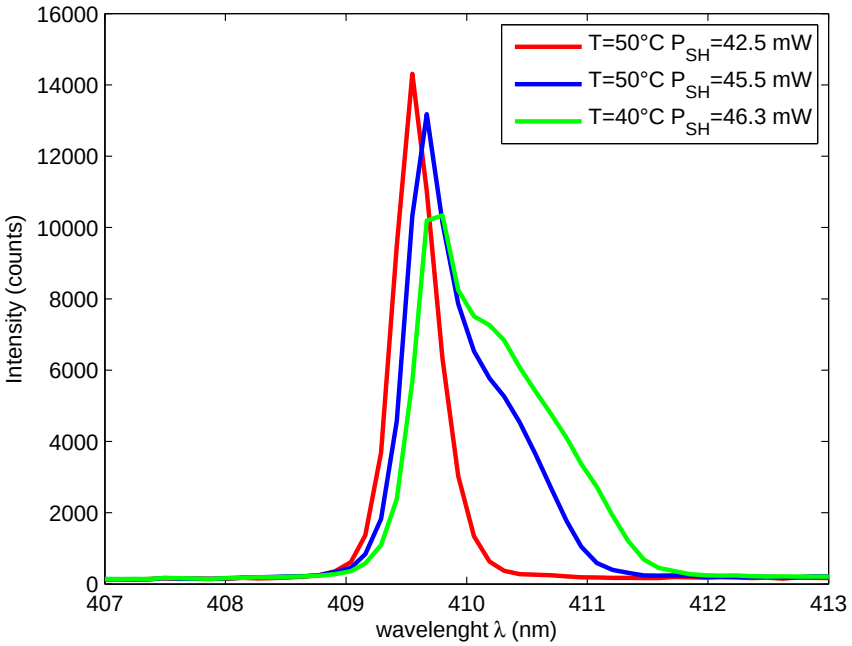

(d) Global view of the effect

Figure 6.3: Photorefractive effect at $T = 50°C$

In the case with focal lenght $f = 120 \ \ mm$ we have noted the instability only during the test of entanglement generation, because the effect of widening of the spectrum is very slow and we realized this in operations lasting some tens of minutes.
So the photorefractive effect is manifested in a time scale that decreases when the focal length L1 decreases.

6.2.3 The best performance of SHG

The choice of the minimum focal length L1 which results stable for second harmonic generation is then $f = 150mm$. Firstly, in this focusing condition we have run the temperature scan, measuring the SH power at intervals of $\Delta T = 2.5°C$. From this measurement we have found that the maximum value of SH power is $P_{SH} = 43 \ \ mW$ at $T = 95°C$ (Figure 6.4).

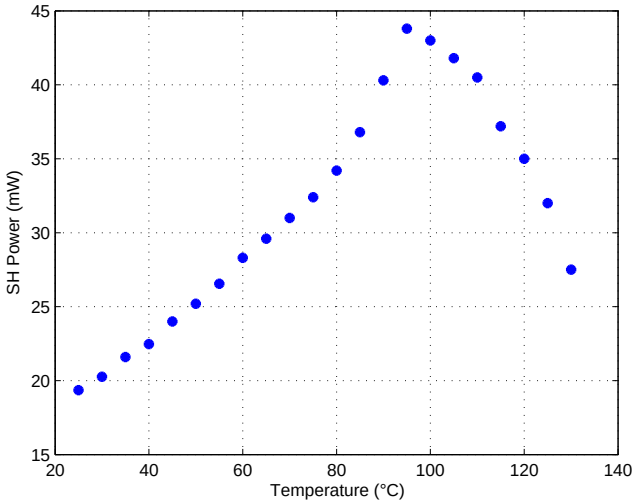

Figure 6.4: Temperature scan

In Fig 6.5, we show the spectrum of SH at the maximum value of the power. From the spectrum, we measured the spectral width $\Delta\lambda_{PPKTP} \simeq 0.38 \ \ nm$ (FWHM). However, this number disclose to the resolution of our spectrometer ($0.35 \ \ nm$) and by deconvolving the instrumental resolution with the measured width we obtain $\widetilde{\Delta\lambda}_{PPKTP} \simeq 0.15nm$ (FWHM). The results of the pulse duration and coherence time are the following:

$$\tau_{FWHM}^{PPKTP} = 0.44 \frac{\lambda_{SH}}{c\widetilde{\Delta\lambda}_{PPKTP}} = 1.6 \ \ ps \tag{6.19}$$

$$\tau_c^{PPKTP} = 0.66\frac{\lambda_{SH}}{c\widetilde{\Delta\lambda}_{PPKTP}} = 2.4 \;\; ps \tag{6.20}$$

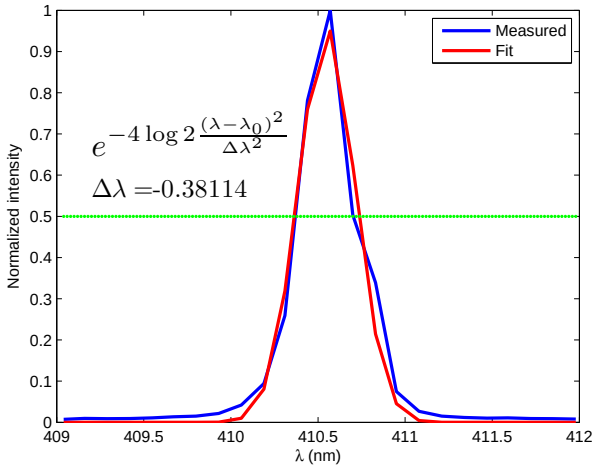

Figure 6.5: SH spectrum of PPKTP refering to the power $P_{SH} = 43 \;\; mW$

In Figure 6.6 we show the spot of SH and its bidimensional Gaussian fitting (b-c) obtained using the function of fitting (5.8). the image of the spot was detected by the CCD camera (Thorlabs DCC1645C) with pixel size of $(L_x = L_y = 3.6 \;\; \mu m)$. From the fitting parameters (m_x, σ_x^2)=$(905 \;\; px, 30 \;\; px)$ and (m_y, σ_y^2)=$(435 \;\; px, 35 \;\; px)$ we calculate the beam waist as follows:

$$W_x = \sqrt{2}\sigma_x^2 L_x \simeq 0.153 \;\; mm, \qquad W_y = \sqrt{2}\sigma_y^2 L_y \simeq 1.178 \;\; mm \tag{6.21}$$

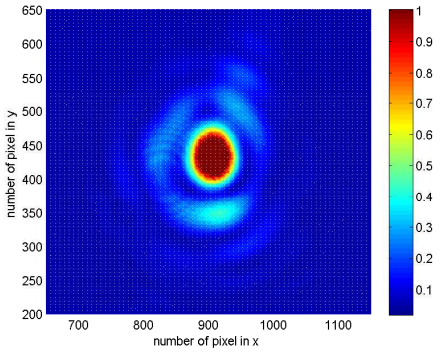

(a) SH spot with $f = 150 \;\; mm$

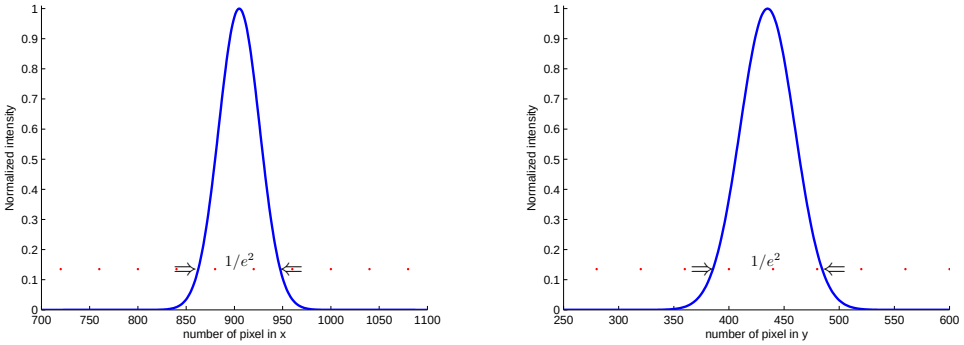

(b) Gaussian fitting of normalizad intensity in the x direction

(c) Gaussian fitting of normalizad intensity in the y direction

Figure 6.6: SH spot of PPKTP with bidimensional Gaussian fitting

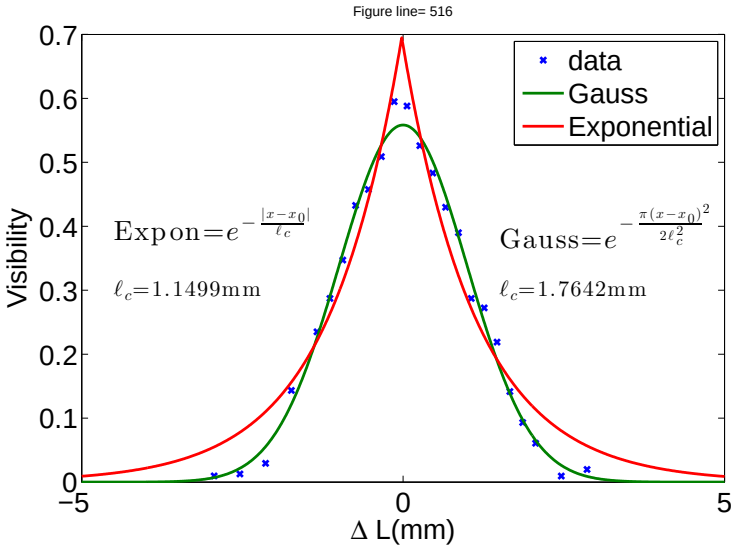

Figure 6.7: Fitting of the visibility

However, we also performed a measurement of the SH coherence time by using the Michelson interferometer. In Appendix A, we show interference pattern detected with the Michelson interferometer in function of the translation stage position. In Figure 6.7 we illustate the data of visibility obtained from the images shown in Appendix A. These data has been fitted by a Gaussian function and exponential function. The best fit has obtained with the Gaussian function with a caherence lenght of $l = 1.7642 \ \ mm$ from which we devived the coherence time:

$$\tau_c^{PPKTP} = \frac{l_c}{c} = 5.88 \ \ ps \tag{6.22}$$

Finally, the efficiency of SH conversion is:

$$\eta_{PPKTP} = \frac{P_{SH}}{\eta_{FILTER} P_F} = \frac{43 \ \ mW}{0.42 * 1.4W} = 7.31 \ \ \% \tag{6.23}$$

6.3 SHG with BBO and BiBO

To have a comparison with different crystals, we also implement the SHG with a BBO and a BiBO crystal. The BBO crystal is 1 mm long, 5 mm thick, Type I and coated. It was the crystal that we tested in the first experiment with a Taccor laser in September 2012. We have retested this crystal because the Taccor laser used in the present experiment has an output power that was nearly twice that the one used in September 2012. The BiBO crystal is 1 mm long, 5 mmthick, Type I and coated. This is the crystal used to generate the second harmonic with laser MIRA, that is a Ti:sapphire laser mode-locking, providing ultrashort pulses ($\sim 150 \ \ fs$) at 76 MHz repetition-rate with an average power of 3.3 W. For each crystal we performed the same measurements shown in the previous sections on PPKTP, in particular the SH spectrum and spot, the spectral width, the coherence time and the second harmonic effciency. In both cases, no temperature tuning is necessary, but we optimize the phase-matching by tilting the crystals.

6.3.1 Results with BBO crystal

In the case of BBO, we optimize the SHG by using a lens of 50mm focal length. The obtained SH power is $P_{SH} = 32.7 \ \ mW$. The second harmonic effciency obtained in this case is given by:

$$\eta_{BBO} = \frac{P_{SH}}{\eta_{FILTER} P_F} = \frac{32.7 \ \ mW}{0.42 * 1.4W} \simeq 5.56 \ \ \% \tag{6.24}$$

In Figure 6.8 we show the spectrum of the SH. From the same figure, the spectral width results to be $\Delta\lambda_{BBO} \simeq 3.28 \;\; nm$ (FWHM) and the coherence time is:

$$\tau_c^{BBO} = 0.66 \frac{\lambda_{SH}^2}{c\Delta\lambda_{BBO}} \simeq 111 \;\; fs \tag{6.25}$$

We again measured the coherence time by the Michelson interferometer.

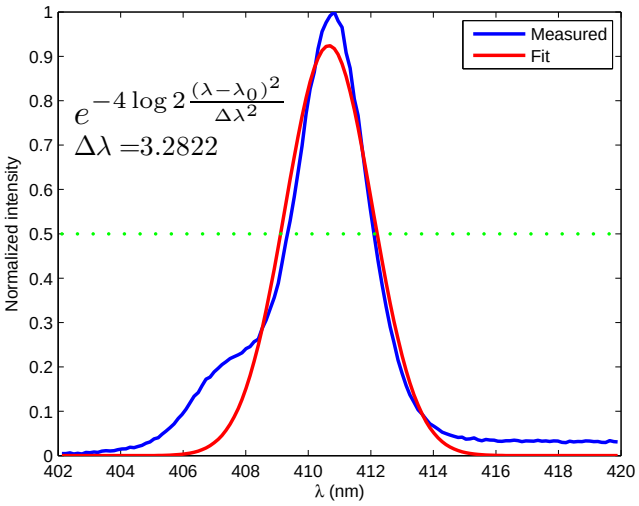

Figure 6.8: BBO SH spectrum

The positions l_i and l_f corresponding to the beginning and the end of the interference are separated by $2(l_f - l_i) = 140 \;\; \mu m$. By using the same ratio $2(lf - li)/l_c = 5.8mm/1.76mm = 3.29 \;\; mm$ obtained for the PPKTP we get a coherence length $l_c = 43 \;\; \mu m$ and a correspondent coherence time:

$$\widetilde{\tau}_c^{BBO} = \frac{l_c}{c} \simeq 141 \;\; fs \tag{6.26}$$

The uncertainties on the determination of l_i and l_f $(10 \;\; \mu m)$, make the two values of τ (one from the spectrum and the other from the interferometer) comparables, with the values (9) more reliable. In Figure 6.9 we show the second harmonic spot presenting a strong ellipticity due to the spatial walk-off effect present in birefringent crystals. In the same way of the PPKTP, we calculate the values of the spot from the fitting parameters as follows:

$$(m_x, \sigma_x^2)_{horizont} = (610 \;\; px, 210 \;\; px): \quad W_x^{horizont} \simeq 1.07 \;\; mm \tag{6.27}$$

$$(m_y, \sigma_y^2)_{horizont} = (490 \;\; px, 280 \;\; px): \quad W_y^{horizont} \simeq 1.43 \;\; mm \tag{6.28}$$

$$(m_x, \sigma_x^2)_{vertical} = (450 \;\; px, 190 \;\; px): \quad W_x^{vertical} \simeq 0.97 \;\; mm \tag{6.29}$$

$$(m_y, \sigma_x^2)_{vertical} = (257 \;\; px, 050 \;\; px): \quad W_y^{vertical} \simeq 0.25 \;\; mm \tag{6.30}$$

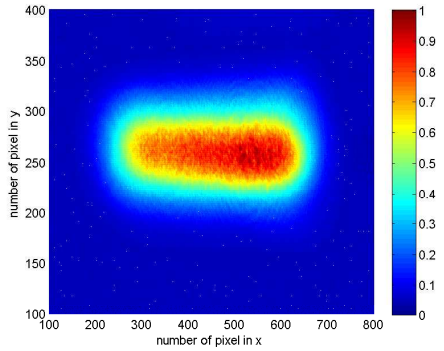

(a) BBO vertical waist

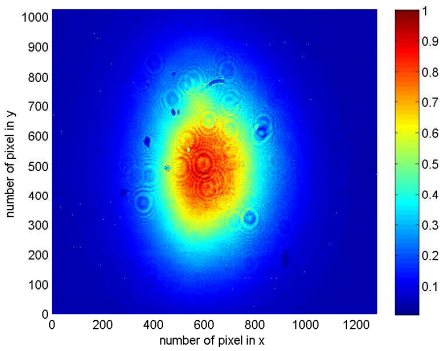

(b) BBO horizontal waist

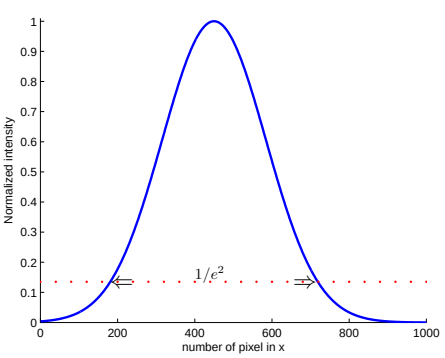

(c) Vertical Gaussian fitting of normalized intensity in x direction

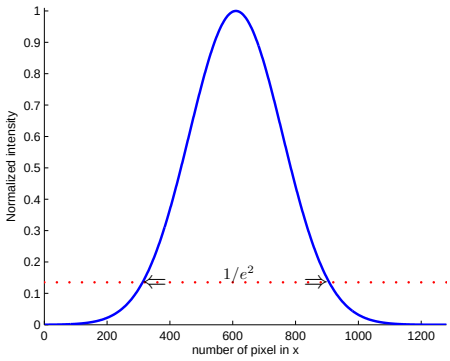

(d) Horizontal Gaussian fitting of normalized intensity in x direction

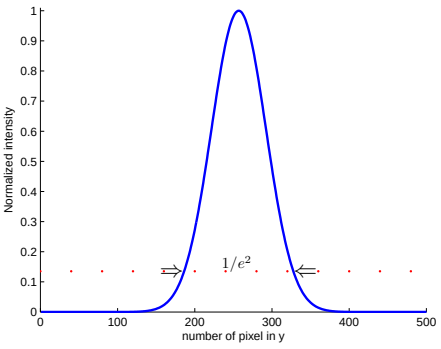

(e) Vertical Gaussian fitting of normalized intensity in y direction

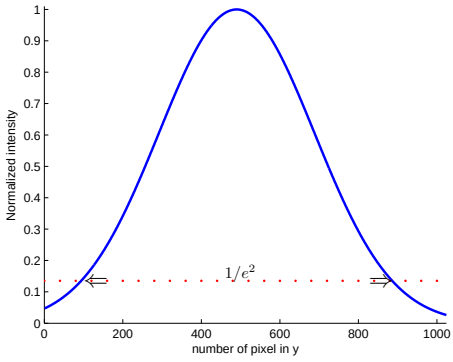

(f) Horizontal Gaussian fitting of normalized intensity in y direction

Figure 6.9: SH spots of BBO with bidimensional Gaussian fitting

6.3.2 Results with BiBO crystal

In the case of BiBO, we optimize the SHG by using a lens of $f = 50 \ \ mm$ focal length. The obtained SH power is $P_{SH} = 76.6 \ \ mW$. The second harmonic efficiency obtained in this case is given by:

$$\eta_{BiBO} = \frac{P_{SH}}{\eta_{FILTER} P_F} = \frac{76.6 \ \ mW}{0.42 * 1.4W} \simeq 13 \ \ \% \tag{6.31}$$

We would like to note that this is the highest observed coeffcient, though not corresponding to the best entangled pair generation conditions. In Figure 6.10 we show the spectrum of the SH. From the same figure, the spectral width results to be $\Delta\lambda_{BBO} \simeq 3.28 \ \ nm$ (FWHM) and the coherence time is:

$$\tau_c^{BiBO} = 0.66 \frac{\lambda_{SH}^2}{c \Delta\lambda_{BiBO}} \simeq 144 \ \ fs \tag{6.32}$$

We again measured the coherence time by the Michelson interferometer.

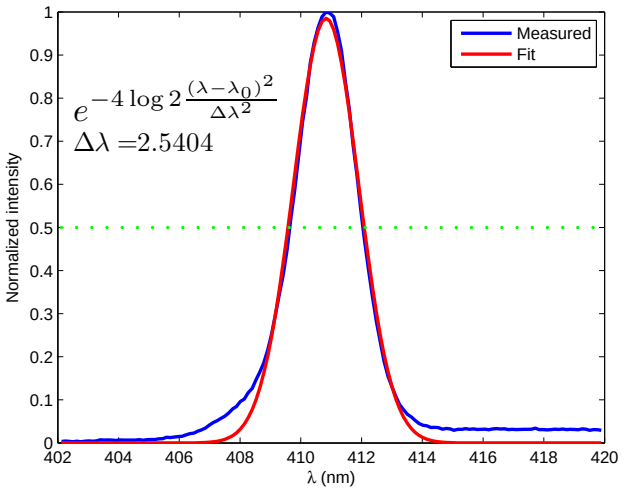

Figure 6.10: BiBO SH spectrum

The positions l_i and l_f corresponding to the beginning and the end of the interference are separated by $2(l_f - l_i) = 250 \ \ \mu m$. By using the same ratio $2(lf - li)/l_c = 5.8mm/1.76mm = 3.29 \ \ mm$ obtained for the PPKTP we get a coherence length $l_c = 76 \ \ \mu m$ and a correspondent coherence time:

$$\widetilde{\tau}_c^{BiBO} = \frac{l_c}{c} \simeq 253 \ \ fs \tag{6.33}$$

In this case the two values of τ, given in equation (6.32) and (6.33) are quite different and the origin of the discrepancy is not clear.

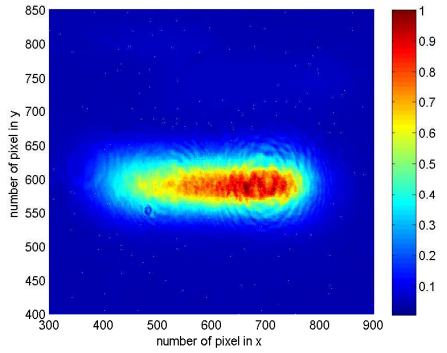

(a) BiBO vertical waist

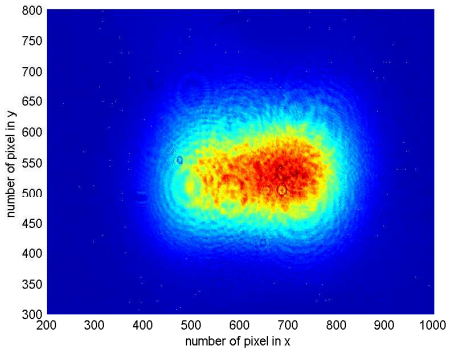

(b) BiBO horizontal waist

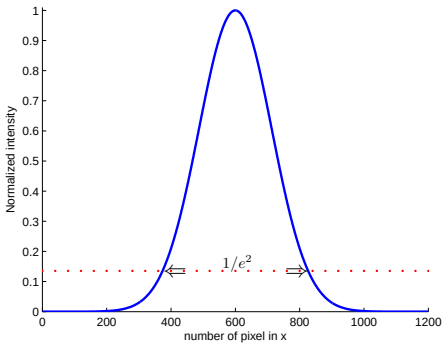

(c) Vertical Gaussian fitting of normalized intensity in x direction

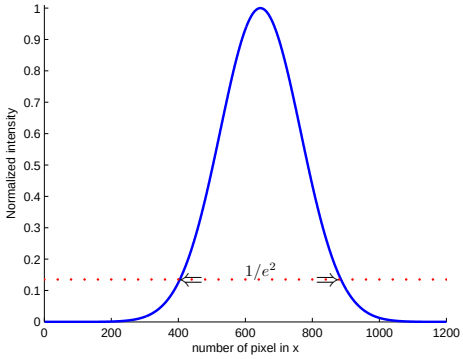

(d) Horizontal Gaussian fitting of normalized intensity in x direction

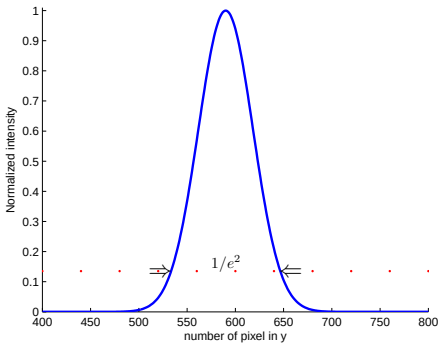

(e) Vertical Gaussian fitting of normalized intensity in y direction

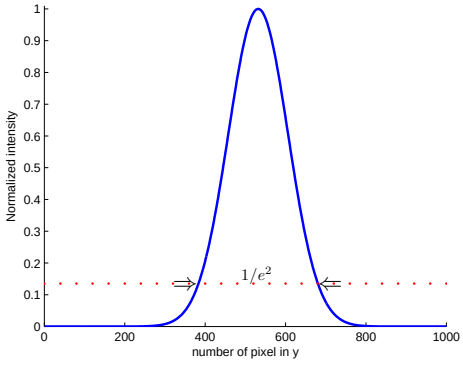

(f) Horizontal Gaussian fitting of normalized intensity in y direction

Figure 6.11: SH spots of BiBO with bidimensional Gaussian fitting

In Figure 6.11 we show the second harmonic spot of BiBO crystal and in the same way of the PPKTP, we calculate the values of the spot from the fitting parameters as follows:

$$(m_x, \sigma_x^2)_{horizont} = (645 \ \ px, 170 \ \ px): \quad W_x^{horizont} \simeq 0.87 \ \ mm \tag{6.34}$$

$$(m_y, \sigma_y^2)_{horizont} = (532 \ \ px, 105 \ \ px): \quad W_y^{horizont} \simeq 0.53 \ \ mm \tag{6.35}$$

$$(m_x, \sigma_x^2)_{vertical} = (600 \ \ px, 160 \ \ px): \quad W_x^{vertical} \simeq 0.81 \ \ mm \tag{6.36}$$

$$(m_y, \sigma_x^2)_{vertical} = (590 \ \ px, 040 \ \ px): \quad W_y^{vertical} \simeq 0.20 \ \ mm \tag{6.37}$$

6.4 Results of SPDC measurements

In this section we present the results abstained in the generation of polarization-entangled photon pairs. With the setup of SPDC experiment described in the chapter 5 we can be generated the following entangled states:

$$\frac{1}{\sqrt{2}}(|H\rangle_1|V\rangle_2 - |V\rangle_1|H\rangle_2) \tag{6.38}$$

We have tested the coincidences in the best case of second harmonic by PPKTP. The aligment and focusing condition are two important aspects in order to ensure the success of the experiment. For this reason the best focusing condition that allowed us to obtain a stable second harmonic without photorefractive effects is:

$$L1 \ f = 150 \ mm \ ; \ L2 \ f = 125 \ mm$$

Then, we checked that the optical setup was aligned. If the count of singles is equal to the different bases $|HV\rangle$ and $|VH\rangle$ the aligment is good.
Another parameter that should be controlled before starting the measurements, is the visibility. The visibility is an estimation of the interference quality and can be calculated as follows:

$$V = \frac{N_{MAX} - Nmin}{N_{MAX} + Nmin} \tag{6.39}$$

where N_{MAX} is the number of the photon pairs detected in the maximum position and N_{min} is the number of the photon pairs detected in the minimum position.

We measured the coincidence in two bases $\{H, V\}$ and $\{+, -\}$. In the first base $\{H, V\}$ we obtained a good value of the visibiliy ($V > 95$ %), in the another base we have never obtained a good value of the visibility ($V \sim 60$ %).

With $P_{SH} = 36 \ mW$ of PPKTP SHG we obtained the following results:

- By optimizing the directions giving the maximum generation rate of $|HV\rangle$ we get the following rates

  $$|HV\rangle_{opt} = 1300\ Hz\,, \quad |HH\rangle = 6\ Hz\,, \quad |VV\rangle = 10\ Hz$$

  with the single counts given by about 22000 Hz.

- By selecting the directions giving the same generation rate of $|HV\rangle$ and $|VH\rangle$ we get the following rates

  $$|HH\rangle = 10\,sec^{-1}\,, \quad |HV\rangle = 850\,sec^{-1}\,, \quad |VV\rangle = 10\,sec^{-1}\,, \quad |VH\rangle = 800\,sec^{-1}$$

  with a visibility of

  $$V = 97.6\ \%$$

6.4.1 Accidentals

One great advantage of using a GHz pump laser source is related to the amount of accidental coincidences. The total coincidences contain a percentage of "accidental" coincidences, related to the double pair emission. Since the SPDC process is probabilistic, there is a chance to produce more than one pair per single pump pulse. Due to detection inefficiencies, it is possible to detect one photon coming from the first pair and the second from the other pair, giving raise to a coincidence detection not arising from an entangled state. These coincidences are called "accidentals". The amount of accidentals can be calculated as follow.

If ν_p is the pump laser repetition rate and N_1 and N_2 the single photon rate measured at the SPADs, the probability of detection for each pump pulse is given by $p_j = N_j/\nu_p$. The probability of a double detection arising from uncorrelated photons is given by $p_1 \times p_2$. The accidental rate is thus given by

$$C_{acc} = p_1 p_2 \nu_p = \frac{N_1 N_2}{\nu} \tag{6.40}$$

In the present experiment the rate of accidental coincidences is given by:

$$C_{acc} = \frac{N_1 N_2}{\nu} = \frac{22000^2\ Hz^2}{10^9\ Hz} = 0.484\ Hz$$

It is worth to stress that, if we use a pump beam at 76MHz (such as the one the can be obtained with the MIRA) with the average power giving rise to the same rate of single count (22000 Hz), the obtained accidentals would be

$$C_{acc}^{MIRA} = \frac{22000^2\ Hz^2}{76 \cdot 10^6\ Hz} = 6.37\ Hz$$

This number is comparable with the rate obtained for the $|VV\rangle$ and $|HH\rangle$ pairs and thus will cause a decrease of the visibility.

6.4.2 TACCOR scalability

The experiment of Entangled photon-pairs generation, has not shown the increase of the generation coefficient that we expected. The problem is that the average power of the SH generated is still too low, so that the pump pulses generated are not all "active". Indeed, the relationship between the rate of coincidences and the average power is linear. If we generate a SH sufficiently high to enter in the condition of multi-pairs generation, the relationship could not be linear anymore. If we were able to generate a very efficient SH, we could take advantage of the TACCOR "scalability". This feature allows to distribute the energy per pulse in a different way and in multi-pairs conditions we should be able to enhance the generation of a single Entangled photon-pairs.

Chapter 7

Conclusion

This thesis work's objective was the investigation of the possibility to enhance the probability of generation of a single entangled photon pair. To gain this aim a gigahertz laser was used. Due to the low energy per pulse of the laser, we tried to generate a highly efficient SH using a QPM periodically poled KTP (PPKTP) crystal. This mean has a high non-linear coefficient (5-6 times more than BiBO and BBO) so the SH generated is theoretically more efficient. However, the efficiency of SHG achieved with PPKTP is lower than BiBO crystal and larger than BBO; this is due to the photorefractive effect that limits the efficiency and the beam quality. In order to obtain a stable second harmonic (without photorefractive effect) we used a focusing condition of lens L1 with focal length $f = 150\ mm$.. With short focal lens ($f < 150\ \ mm$) we measured a peak efficiency with PPKTP the 10% greater than with BiBO and BBO crystals. Unfortunately, these configurations cannot be considered reliable due to the instabilities caused by photorefractive effect. If this effect could be reduced, better efficiency will be obtained. The photorefractive effect is a big problem for PPKTP crystal and the method used to reduce the effect, the self-anneling for crystal temperatures above 180 $°C$, seems not to solve the problem. Other methods to solve the problem of photorefractive effects involve the use of a modified PPKTP crystal: one possibility is to drug the crystal with rubidium ions (Rb^+) during its growth process, that could limit the photorefractive effect reducing the ionic conductivity; anyway it has the side effect that the poling of the crystal results more difficult. Another method is to build the crystal with a periocally poling grating period, that can reach the phase matching condition at higher temperature. Thanks to the higher temperature, the photorefractive effect is reduced. Furthermore, we can use coated crystals that can increase a lot the efficiency of about 10 %.
The best feature of PPKTP is the spectral compression that allows to gener-

ate second harmonic pulses with picosecond coherence time. SH with PPKTP presents a better spatial mode (almost Gaussian) compared to the other crystals.
The main advantage of Taccor for entanglement generation is the lower accidental rate at fixed single photon detection rate compared with other sources. This is due to its repetition rate $\nu_p = 1\ GHz$, since the number of accidental coincidences scales as:

$$C_{acc} = \frac{N_1 N_2}{\nu_p}$$

Current commercial single photon detectors have jitter (i.e. the indetermination on the arrival time of the photons) of about 350 ps. Then, by using coincidence windows slightly lower than 1 ns it is possible to avoid accidentals coming from different pulses without loosing real coincidences. Repetition rate above 1-1.5 GHz will require detectors with better temporal resolution: the Taccor represents the optimal solution for the accidental problem.
The photon pair rate generation with TACCOR scales with the power similarly to the MIRA source. The MIRA source allows to generate a second harmonic power of 300 mW and the rate of photon pairs obtained is around 10.5 KHz; 36 mW of SH from the TACCOR produces 1.3 KHz coicidences. With our produced SH we could not take advantage of the TACCOR scalability respect to MIRA. To exploit this feature we should be able to generate a much higher SH in order to obtain the condition of multi-pairs generation. Compactness and simplicity of the TACCOR is a positive feature allowing easily relocation and operation in out of the lab environment. Syncronization with another oscillator with high precision allow to envisage the exploitation of TACCOR for entanglement swapping and teleportation experiment.

Appendix A

7.1 Visibility of interference fringes by the SH with PPKTP crystal

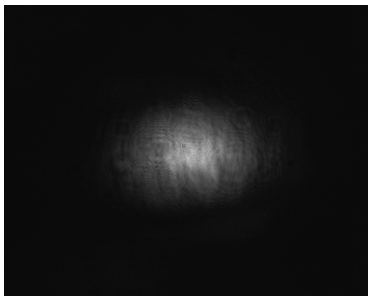

(a) $l_i = 9.50\ mm$

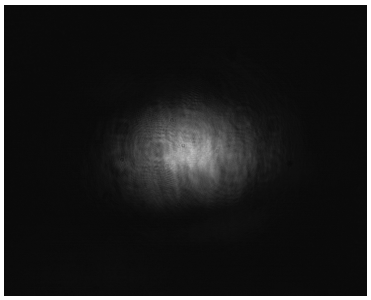

(b) $l = 9.70\ mm$

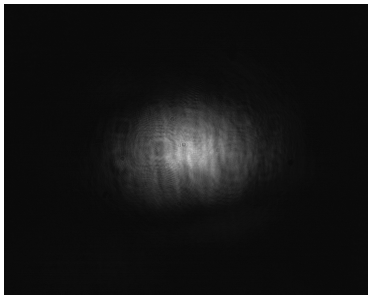

(c) $l = 9.90\ mm$

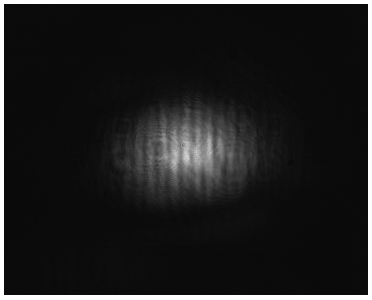

(d) $l = 10.10\ mm$

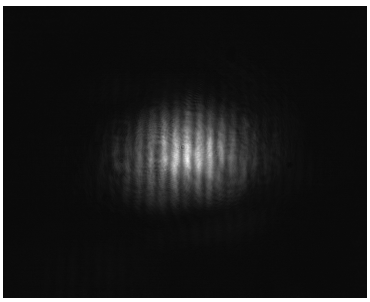

(e) $l = 10.30\ mm$

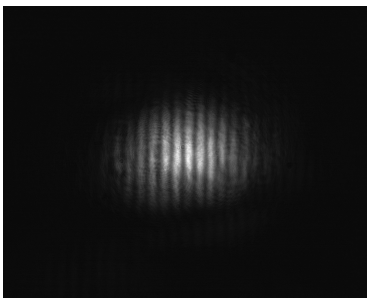

(f) $l = 10.40\ mm$

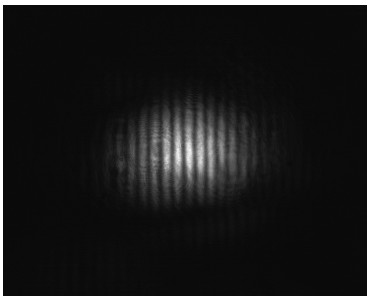

(g) $l = 10.50\ mm$

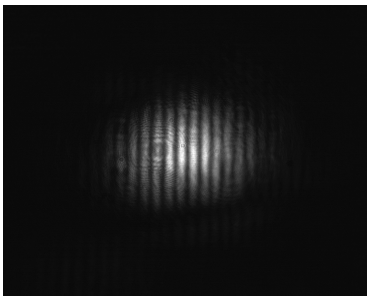

(h) $l = 10.60\ mm$

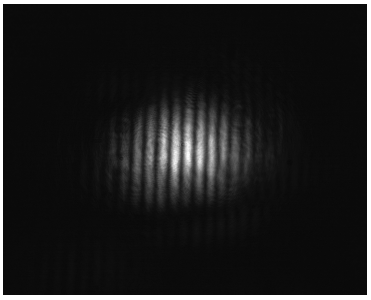

(i) $l = 10.70\ mm$

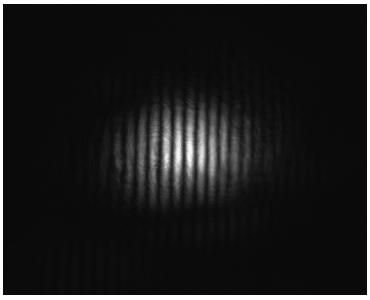

(j) $l = 10.80\ mm$

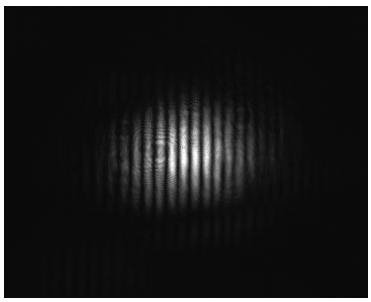

(k) $l = 10.90\ mm$

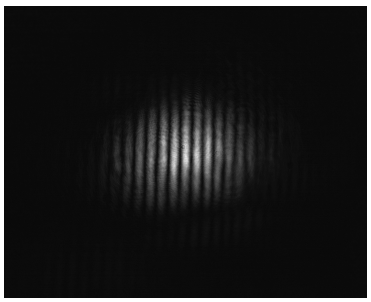

(l) $l = 11.00\ mm$

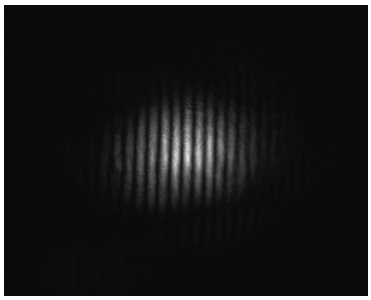

(m) $l = 11.10\ mm$

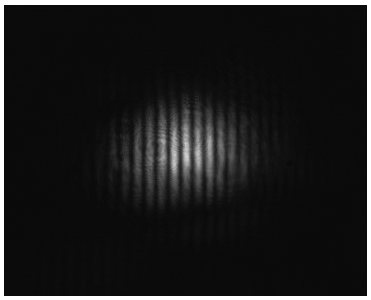

(n) $l = 11.20\ mm$

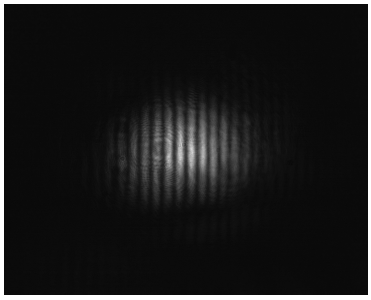

(o) $l = 11.30\ mm$

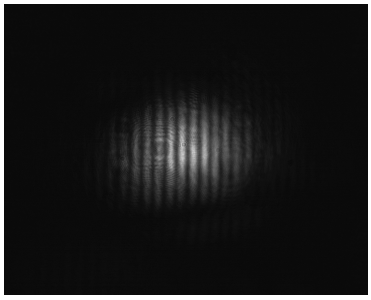

(p) $l = 11.40\ mm$

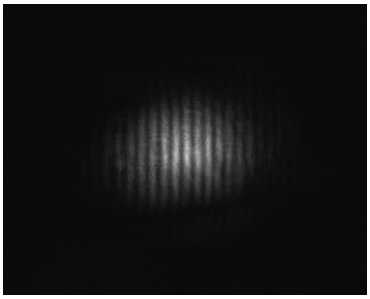

(q) $l = 11.50\ mm$

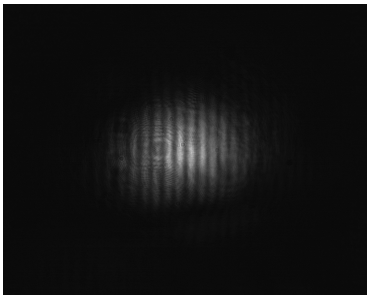

(r) $l = 11.60\ mm$

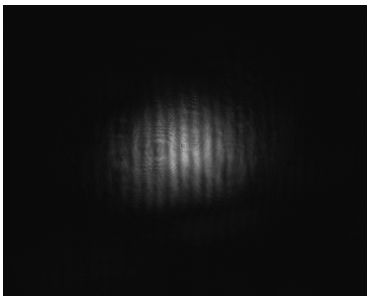

(s) $l = 11.70\ mm$

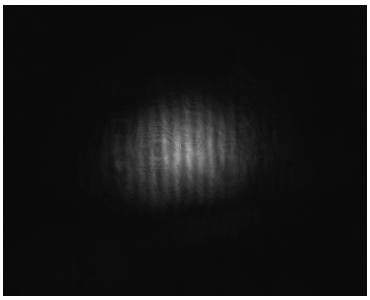

(t) $l = 11.80\ mm$

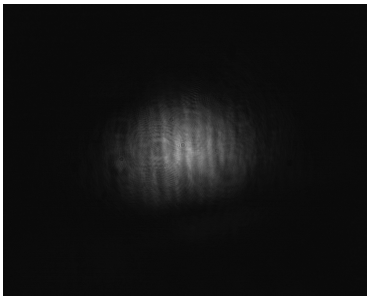

(u) $l = 11.90\ mm$

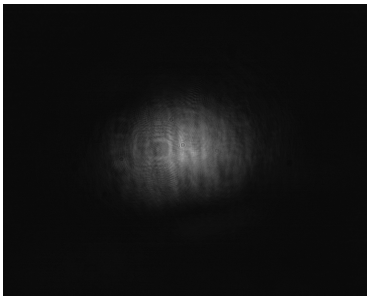

(v) $l = 12.00\ mm$

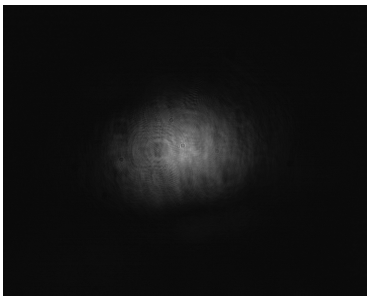

(w) $l = 12.20\ mm$

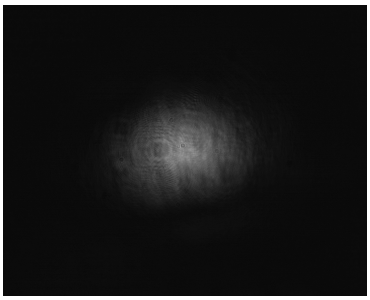

(x) $l_f = 12.40\ mm$

Figure 7.1

Bibliography

[1] A. Ehlers, I. Riemann, S. Martin, R. Le Harzic, A. Bartels, C. Janke, and K. König. «*High repetition rate compact femtosecond laser: A powerful multiphoton tool for nanomedicine and nanobiotechnology* », J. Appl. Phys. **102**, 014701 (2007).

[2] M.Ghotbi,M. Ebrahim-Zadeh,A.Majchrowski, E.Michalski, and I.V.Kityk. «*High-avarage-power femtosecond pulse generation in the blue using* BiB_3O_6 », Opt. Lett. **29**(21), 2530-2532 (2004).

[3] A.V. Smith, D.J. Armstrong, and W.J. Alford. «*Increased acceptance bandwidths in optical frequency conversion by use of multiple walk-off-compensating nonlinear crystals* », J. Opt. Soc. Am. B **15**(1), 122 (1998).

[4] R.J. Gehr, M.W. Kimmel, and A.V. Smith. «*Simultaneous spatial and temporal walk-off compensation in frequency-doubling femtosecond pulses in* $\beta - BaB_2O_4$ », Opt. Lett. **23**(16), 1298-1230 (2004).

[5] H. Wang and M.Andrew. «*Efficiency of short-pulse Type-I second-harmonic generation with simultaneous spatial Walk-Off,temporal walk-off, and pump depletion* », IEEE. J.Quantum Electron. vol **28**(12), 1600-1617 (2003).

[6] G.R. Fayaz, M. Ghotbi, and M. Ebrahim-Zadeh. «*Efficiency second-harmonic generation of tunable femtosecond pulses into the blue in periodically poled KTP* », Appl. Phys. Lett. **86**(12), 061110 (2005).

[7] M. Marangoni, D. Brida, M. Quintavalle, G. Cirmi, F.M. Pigozzo, C. Manzoni, F. Baronio, A.D. Capobianco, and G. Cerullo. «*Narrow-bandwidth picosecond pulses by spectral compression of femtosecond pulses in a second-order nonlinear crystal* », Opt. Express **15**(14), 8884-8891 (2007).

[8] A.K. Ekert. «*Quantum cryptography based on bell's theorem* », Phys. Rev. Lett. **67**(661), (1991).

[9] C.H. Bennet and S.J. Wiesner. «*Communication via one- and two-particle oper-ators on einstein-podolsky-rosen states* », Phys. Rev. Lett. **69**(661), (1992).

[10] C.H. Bennet, G. Brassard, C. Crepeau, R. Jozsa, A. Peres, and W.K. Wootters. «*Teleporting an unknown quantum state via dual classical and einstein-podolsky-rosen channels* », Phys. Rev. Lett. **70**(2881), (1993).

[11] M.Le Bellac. «*Quantum Physics* », Cambridge University Press, 2006.

[12] G. Cariolaro. «*Comunicazioni Quantistiche* », Aprile,2009.

[13] A. Einstein, B. Podolsky, and N. Rosen. «*Can quantum-mechanical desciption of physical reality be considered complete?* », Phys. Rev. **47**(777), (1935).

[14] J.S. Bell. «*On the einstein-podolsky-rosen paradox* », Physics, **1**, (1964).

[15] B.E.A. Saleh, and M.C. Teich. «*Fundamentals of photonics* », Wiley, Second Edition (2006).

[16] P.A. Franken, A.E. Hill, C.W. Peters and G. Weinreich «*Generation of optical harmonics of photonics* », Phys. Rev. Lett. **7**, 118, (1961).

[17] Robert W. Boyd «*Nonlinear Optics* », Academic Press, Third Edition (2008).

[18] J.A. Armstrong, N. Bloembergen, J. Ducuing and P.S. Perhsan «*Interactions between Light Waves in a Nonlinear Dielectric Optics* », Phys. Rev. **127**, 1918, (1962).

[19] I. Tordjman, R. Masse, J.C. Guitel, and Z. Kristallogr «*Crystalline structure of monophosphate* $KTiO_5$», Zeitschrift fur kristallographie **139**, 103-115 (1974).

[20] John D. Bierlein and H. Vanherzeele «*Potassium titanyl phosphate: properties and new applications* », J. Opt. Soc. Am. B **6**(4), 622-633 (1989).

[21] F. Borbone, A.Roviello, R.Lanzella,A.Vitagliano «*Materiali polimerici per applicazioni in ottica non lineare del secondo ordine: sintesi, struttura e proprietá* », Tesi di dottorato in scienze chimiche.

[22] M. Houe, and P.D. Townsend «*An introduction to methods of periodic poling for second-harmonic generation* », J. OPhys. D:Appl. Phys. **28**, 1747-1763 (1995).

[23] ≪*Raicol Crystals Ltd* ≫, URL: http://www.raicol.com

[24] I. Shoji, T. Kondo, A. Kitamoto, M. Shirane, and R. Ito ≪*Absolute scale of second-order nonlinear-optical coefficients* ≫, J. Opt. Soc. Am. B **14**(9), 2268-2294 (1997).

[25] S. Manjooran, H. Zhao, I.T. Lima Jr., and A.Major ≪*Phase-matching properties of PPKTP, MgO:PPSLT and MgO:PPcLN for ultrafast optical parametric oscillation in the visible and near-infrared with green pumpranges* ≫, Laser Physics, **22**(8), 1325-1330 (2012).

[26] G.D. Boyd, and D.A. Kleinman ≪*Parametric Interaction of Focused Gaussian Light Beams* ≫, J. Appl. Phys. **39**(8), 3597-3639 (1968).